

SPATIOTEMPORAL VARIABILITY OF MESOSCALE CONVECTIVE SYSTEMS
AND THEIR PROPERTIES IN THE TROPICS USING IMERG

by

Manikandan Rajagopal

A dissertation submitted to the faculty of
The University of Utah
in partial fulfillment of the requirements for the degree of

Doctor of Philosophy

Department of Atmospheric Sciences

The University of Utah

August 2022

Copyright © Manikandan Rajagopal 2022

All Rights Reserved

ABSTRACT

Moist convection sometimes organizes into Mesoscale Convective Systems (MCSs) that are at least 100 km wide. MCSs, in the Inter-Tropical Convergence Zone (ITCZ), affect global circulation through their upper tropospheric heating that elevates the Hadley cell circulation centers. They also directly affect us through severe weather such as hail, strong winds, and flooding. In the tropics, where the surface observations are sparse, the Infrared (IR) satellite data have been used to track MCSs and study their regional properties. Although useful, the IR data have biases in the inferred MCS properties such as rain rates, area, lifetime, and propagation velocity. Integrated-Multisatellite Retrievals for Global Precipitation Mission (IMERG) is NASA's global precipitation product available every 30 minutes and has a lower bias than IR. We use the Forward in Time (FiT) algorithm to track MCSs over the global tropics from 2011 to 2020 and store their properties in the Tracked Mesoscale Precipitation Systems (TIMPS) database. The ten years of TIMPS data is used to study the spatial and temporal variability of MCSs and their properties.

Our results show that MCSs contribute 70 – 90% of annual precipitation, though they are only ~7% of all tracked systems. When comparing broadly, the oceanic MCSs have a larger area and longer lifetime than land systems. MCSs occur more often over the Amazon basin and the Maritime Continent than in central Africa, which has higher thunderstorm frequency. The Amazon basin has many large, long-lived MCSs similar to

the ocean; therefore, aptly called the “Green Ocean”.

Another form of variability is the diurnal changes in convection and precipitation. The land and ocean have diurnal cycles that are out of phase, with maximum precipitation typically in the evening over land and early morning over the ocean. However, we found that some ocean areas have an afternoon maximum influenced by neighboring land. These regions have the time of maximum precipitation change gradually from early morning near offshore to an afternoon maximum over the open ocean. Therefore, it must be a diurnally forced propagating disturbance that produced the afternoon maximum over some open ocean areas.

To my grandmother, Ambujavalli

TABLE OF CONTENTS

ABSTRACT.....	iii
ACKNOWLEDGMENTS	viii
1. INTRODUCTION.....	10
1.1 Background.....	10
1.2 Convection Variability.....	11
1.3 Satellite Studies.....	13
1.4 Tracking MCSs	15
1.5 Motivation.....	15
1.6 Objectives	17
1.7 References.....	18
2. COMPARISONS OF IMERG VERSION 06 PRECIPITATION AT AND BETWEEN PASSIVE MICROWAVE OVERPASSES IN THE TROPICS.....	24
2.1 Abstract.....	25
2.2 Introduction.....	25
2.3 Data	26
2.3.1 CPEX aircraft data	26
2.3.2 IMERG version 06B	27
2.4 Methods.....	27
2.4.1 MCSs: Tracking and properties	27
2.4.2 Constructing precipitation rate distributions.....	28
2.4.3 Computing precipitation occurrence (%).....	29
2.5 Results.....	30
2.5.1 Case Study 1: 6 June 2017	30
2.5.2 Case Study 2: 10 June 2017	31
2.5.3 Precipitation rate distribution: PMW versus morphing	33
2.5.4 Precipitation occurrence: PMW versus morphing	34
2.6 Discussion	35
2.7 Conclusions.....	36
2.8 References.....	36
3. TRACKING MESOSCALE CONVECTIVE SYSTEMS AND SPATIAL VARIABILITY OF THEIR PROPERTIES IN THE TROPICS USING IMERG. .	39
3.1 Abstract.....	39
3.2 Introduction.....	40
3.3 Data and Methods	44

3.3.1 IMERG version 06B	44
3.3.2 Tracking algorithm.....	46
3.3.3 Recent improvements to the FiT	48
3.3.4 Tracking challenges	49
3.3.5 Tracking procedure	52
3.3.6 Optimal tracking parameters.....	54
3.3.7 TIMPS dataset.....	58
3.4 Results.....	60
3.4.1 Rain contribution	60
3.4.2 MCS frequency	62
3.4.3 Area.....	65
3.4.4 Precipitation intensity	67
3.4.5 Lifetime.....	69
3.4.6 Propagation velocity	71
3.4.7 Motion vector.....	74
3.4.8 Relationship between MCS properties.....	75
3.5 Summary	76
3.6 References.....	95

4. DIURNAL CYCLE TRANSITION FROM COAST TO OPEN OCEAN AND INLAND REGIONS. 105

4.1 Abstract	105
4.2 Introduction.....	106
4.3 Data and Methods	110
4.3.1 IMERG version 06B	111
4.3.2 TIMPS dataset.....	112
4.3.3 Study regions and seasons	112
4.3.4 Diurnal cycle.....	113
4.4 Results.....	114
4.4.1 IMERG vs. PR	114
4.4.2 Regional: Coast to open ocean.....	115
4.4.3 Spatial variability	118
4.4.4 Global: Coast to open ocean and inland	119
4.5 Discussion	121
4.6 Summary	124
4.7 References.....	135

5. CONCLUSIONS. 140

5.1 Summary	140
5.2 Caveats.....	143
5.3 Future work.....	144
5.4 References.....	145

ACKNOWLEDGMENTS

I want to thank my advisor Ed Zipser for the opportunity to work on this research and to participate in the field programs. I thoroughly enjoyed the fieldwork; although hectic, it was engaging and elevated my interest in meteorology. Ed always encouraged asking questions, and I enjoyed his lucid explanations. I also want to express my gratitude to my committee members - Steve Krueger, Adam Varble, Tim Garrett, and Joe Turk. They provided valuable feedback on each chapter as I worked through this dissertation. I enjoyed the hour-long science discussion with Adam Varble when he was at the University of Utah, and I still do when we meet once in a while. Running into Tim Garrett in the hallways and talking about science and food always makes my day. Joe Turk has supported me greatly since my first year by discussing my research progress and connecting me with people during conferences. Thank you all.

Special thanks to Steve Krueger, who has been my mentor. Thanks for introducing me to numerical modeling and the countless discussion on weather and research. Mary Anne Berzins, my other mentor, has greatly helped me with my communication, writing, and presentation skills. Holly Moreno, the academic advisor, requires a special mention. She helped me find resources to do my research and career growth. Special thanks to the University of Utah's graduate writing center members – Will, Blair and Jake, for reviewing my manuscripts and providing feedback.

I am grateful for the collaboration with George Huffman and Jackson Tan. I learned so

much about the IMERG algorithm, which immensely helped me with my research. I also want to thank James Russell, with whom I collaborated to create the TIMPS dataset. I appreciate the discussions and his colossal effort to create this dataset. Zipser group members and friends – Zhixiao Zhang, Peter Veals, Michell Tinoco-Morales, Mckenna Stanford, Trey Alvey, Sarah Bang, and Crystal Painter, helped and supported me at various times through these years. My classmates and friends – Xia Li, Husile Bai, and Kyle Fitch, with whom I enjoyed learning and sharing ideas.

My dearest friends and family here, who cheered and supported me - Alysha Braithwaite, Mary Anne Jenkins, Michael Barton, Tessa Galland, Jenny Campbell, Brian Busath, Gurupratap Bhatti, and Austin Watkins, thank you for being there. Other friends and family in India – Shankari, JayaBharath, Manimegalai, and Mayur, who looked out for me.

This research was supported by NASA Grant NNX17AG74G and NNX16AD76G, under the leadership of Ramesh Kakar and Gail Jackson, who is dearly missed.

CHAPTER 1

INTRODUCTION

In the tropics, moist convection occurs at various spatial scales, from small boundary layer clouds to large hurricanes. This dissertation focuses on the mesoscale convective systems (MCSs) that are 100 km wide in at least one direction (Houze, 2004). Though MCSs occur less frequently, they play a significant role in global weather and climate. The MCSs exhibit different characteristics depending on the region and time they occur. Here, we explore the spatiotemporal variability of MCS properties such as frequency, area, rain volume, precipitation intensity, and propagation velocity using the Integrated Multi-satellite Retrievals for Global Precipitation Mission (IMERG) precipitation data.

1.1 Background

MCSs affect global climate through their latent heating and radiative effects. Their typical structure has deep convective cells and broad stratiform clouds (Houze, 2004). The stratiform clouds create a top-heavy latent heating profile (Houze 1989; Schumacher and Houze, 2004), and the resulting upper tropospheric heating produces a deeper Hadley cell circulation and stronger upper-level winds (Hartmann et al., 1984; Schumacher et al., 2004). MCSs, with vast stratiform and anvil clouds, significantly affect the earth's radiation budget. These clouds reflect the incoming short wave radiation and absorb the

outgoing long wave radiation. Although MCSs have significant radiative impacts, their rain contribution is much more significant, with nearly 50 - 90% of the tropical annual precipitation (Nesbitt et al., 2000; Mathon and Laurent, 2001; Liu, 2011; Feng et al., 2021).

Like climate, the weather is also greatly influenced by MCSs. The top-heavy latent heating on a shorter timescale produces atmospheric waves that propagate to neighboring areas and initiate new convection (Murakami, 1972; Matthews & Kiladis, 2000; Rydbeck & Maloney, 2015). MCSs also impact us directly through severe weather such as hail, strong winds, flooding, and landslides (Maranan et al., 2019; Poveda et al., 2020). Despite their crucial role in both the weather and global climate, numerical models have issues simulating the MCSs and their top-heavy latent heating profile.

1.2 Convection Variability

The convection and its properties depend on the region they occur. The land and ocean contrast, particularly, has received much attention. The land convection tends to be intense, with stronger updrafts reaching higher altitudes than the oceanic convection (Liu and Zipser, 2005; Zipser et al., 2006). The updraft strength affects the lightning frequency; consequently, land has a higher flash rate than the ocean (Bang and Zipser, 2015). Oceanic convection has a higher probability of lightning when it becomes organized as MCSs (Bang and Zipser, 2016). When comparing the precipitation area, the oceanic MCSs have a larger area with wider stratiform precipitation than land (Schumacher and Houze, 2003; Houze et al., 2015). Besides these differences in convective system properties, the land and ocean have diurnal cycles that are out of

phase. Over the land, the maximum precipitation typically occurs in the evening, whereas over the ocean, it is early morning (Yang and Slingo, 2001; Nesbitt and Zipser, 2003; Liu and Zipser, 2008; Biasutti et al., 2012). The diurnal cycle of precipitation over land is closely associated with diurnally forced circulations and the convective system frequency (Nesbitt and Zipser, 2003). However, over the ocean, the processes behind the early morning maximum are complex and are attributed to the enhancement of existing convection, often through radiative feedback (Gray & Jacobson, 1977; Dudhia, 1989).

In addition to these broad land and ocean contrasts, the convection differs between various regions. Over west Africa, the convection often organizes into squall lines during the African monsoon. These squall lines have a leading edge of convective cells with trailing stratiform precipitation. Such structure effectively transports momentum from the mid or lower troposphere to the surface, making MCSs propagate at a speed of $10 - 15 \text{ m s}^{-1}$ (Zipser, 1977; Leary and Houze, 1979; Janiga & Thorncroft, 2016). Over west Africa and the Amazon basin, MCSs initiate during the daytime and continue to grow at night through nocturnal low-level jets (Houze and Betts, 1981; Anselmo et al., 2020). Over the Amazon basin, the MCS cloud depth is shallower with weaker updrafts than central Africa, similar to oceans. Hence, the Amazon basin is called the "Green Ocean" (Silva Dias et al., 2002; Anselmo et al., 2021). Over the Maritime Continent, the islands interspersed among the ocean have a strong diurnally forced convection, mainly from the land-sea breeze circulation (Houze et al., 1981; Hagos et al., 2016). Convection initiates over the islands during the day, growing into MCSs. At night the convection shifts offshore and back over the islands in the afternoon of the following day. Over most ocean basins, the MCSs are often non-squall lines and have a larger

stratiform area (Houze and Betts, 1981; Kingsmill and Houze, 1999). The convection over the ocean is often organized through tropical waves such as Madden Julian Oscillation (Chen and Houze, 1997b; Mapes and Houze, 1993) and Easterly waves (Janiga & Thorncroft, 2016). The regional differences in forcing play a significant role in determining convective system properties.

The seasonal and diurnal cycles are the two dominant modes of temporal variability and are associated with the solar cycle. Most precipitation and the associated convection in the tropics occur in the Inter-Tropical Convergence Zone (ITCZ). This ITCZ position shifts with seasons, more over land than the ocean, creating contrasting convective regimes. For instance, in West Africa, MCSs are common during the northern summer, whereas, in the northern winter, sub-mesoscale systems dominate the convection. The diurnal cycle is another mode of temporal variability. The precipitation and MCSs have a stronger, and more regular, diurnal cycle over the Maritime Continent than in other regions (Houze et al., 1981). Over the ocean, the diurnal cycle is weak, with the maximum precipitation typically in the early morning. However, the afternoon maximum has been reported over the eastern Atlantic (McGarry & Reed, 1978) and east South Pacific Convergence Zone (Albright et al., 1985).

1.3 Satellite Studies

MCSs, over the continental USA, have been studied extensively using dense observational networks, including surface radars. Over the global tropics, the surface observations are sparse; therefore, satellite data is vital to studying MCSs and their properties. Past studies used Infrared (IR) data from the geostationary satellite or space-

borne precipitation radar data to study MCS properties over the tropics (Williams and Houze, 1987; Mathon and Laurent, 2001; Cecil et al., 2005; Houze et al., 2015). Though IR data is helpful in characterizing MCSs, they have biases in the inferred surface precipitation, area, lifetime, and propagation velocity. The surface precipitation is poorly correlated with the IR Tb values. For instance, the anvil clouds with very cold IR Tb may have no surface precipitation. On the other hand, warmer clouds (shallower depth) over oceans and the Amazon basin produce heavy rain through the warm rain process (Woodley et al., 1980; Liu et al., 2007; Berg et al., 2002). The non-precipitating anvil clouds also spread over a large area and live longer due to LW radiative forcing, which causes bias in the MCS's area and lifetime (Houze, 1982).

The Global Precipitation Mission (GPM) and Tropical rainfall measuring mission (TRMM) precipitation radar (PR) have precipitation estimates in better agreement with the surface observations than other satellites. The precipitation feature (PF) database with PF defined as contiguous pixels in the reflectivity field provided a deeper understanding of convective regimes over different regions (Nesbitt and Zipser, 2000; Zipser et al., 2006; Houze et al., 2015). However, the spatial extent of observed MCSs is limited by swath edges. Nearly 9% of TRMM precipitation features are edge features, contributing 42% of total precipitation. These edge features could be a larger system that extends beyond swath boundaries. The PR data also has a poor temporal resolution and cannot be used to track MCSs to study the Lagrangian system properties such as lifetime and propagation velocity.

1.4 Tracking MCSs

The GPM and TRMM precipitation radars provide only snapshots of convective systems. Tracking these convective systems in time will help understand their evolution, such as preferred location and time of initiation, growth, and termination. Moreover, objective tracking is more beneficial for model validation than contingency table-based verification methods because the tracked systems provide context to the model errors in terms of MCS frequency, size, intensity, and lifetime (Davis et al., 2006).

There are different tracking methodologies, such as the areal overlap (Williams, M., Houze, 1987), the centroid distance (Hayden et al., 2021), centroid translation (Ocasio et al., 2020), spatial correlation (Dixon & Wiener, 1993), and graph theory (Whitehall et al., 2015). Though different methods produce different quantitative results, the qualitative conclusions tend to be the same. Of these methods, the areal overlap method has been widely used. Williams and Houze (1987) used the IR satellite data and areal overlap method to track MCSs over the Borneo. Similar studies have been conducted in other regions: South America (Burleyson et al., 2016; Anselmo et al., 2021), West Africa (Martin & Schreiner, 1981; Mathon and Laurent, 2001), and the western Pacific Ocean (Mapes and Houze, 1993; Chen and Houze, 1997b).

1.5 Motivation

Moist convection organized as MCSs has significant impacts on tropical weather and climate. Numerical weather and climate models have issues simulating MCSs with their top-heavy latent heating profiles. Studying the variability of MCSs and their properties in space and time will provide a reference for numerical model validation and

help develop a better parameterization scheme. Various regional studies used IR satellite data to track MCSs and study their lifecycle, but they have biases in the inferred MCS properties.

Integrated Multi-satellite Retrievals for GPM (IMERG) is NASA's recent global precipitation product available at high spatial (0.1°) and temporal resolution (every 30 minutes). IMERG uses passive microwave (PMW) observations from the constellation of low earth orbit (LEO) satellites. If PMW observations are unavailable at a location, IMERG combines the advected PMW precipitation from past and future observations with IR Tb gradient-based precipitation. IMERG precipitation is less affected by thin anvils because the PMW precipitation is based on total column ice water content, and the IR precipitation is based on Tb gradients instead of direct Tb values. In addition to having better precipitation data, IMERG's high time resolution makes tracking more reliable and accurate since a convective system's translation and evolution are smaller between consecutive time steps.

The availability of IMERG precipitation data for a long period and accessibility to fast computing has motivated us to track MCSs over the global tropics ($30^\circ\text{N} - 30^\circ\text{S}$) from 2011 to 2020. We use the Forward in Time (FiT; Skok et al., 2009, 2013) algorithm to track MCSs in the IMERG precipitation field. Our dataset will provide a more consistent regional comparison than past studies because of the long-term data and the same tracking algorithm used over various regions. Recent studies that tracked MCSs in the IMERG precipitation field used different algorithms (Feng et al., 2021; Hayden et al., 2021). This study is, therefore, complementary and provides a different perspective of MCS properties in the tropics.

In addition to spatial variability, we explore the diurnal cycle over land and ocean as a function of distance from the coastline. Though it is typical for the ocean to have maximum precipitation in the early morning, an afternoon maximum was observed over the eastern Atlantic during the Global Atmospheric Research Program Atlantic Tropical Experiment (GATE; McGarry & Reed, 1978). This afternoon maximum is intriguing and likely due to the influence of nearby land. Therefore, we explore the transition of the diurnal cycle from coast to open ocean and inland regions, with the possibility of finding afternoon maxima in the intervening ocean areas (~ 1000 km from the coastline).

1.6 Objectives

The main focus of this dissertation is to study the spatial and temporal variability of precipitation and MCSs properties. Since IMERG is a relatively recent satellite precipitation product, first, we examine its ability to represent MCSs and their lifecycle using the Convective Processes Experiment (CPEX) data for validation. Later, we use the FiT algorithm to track MCSs in the IMERG precipitation field. FiT is a generic algorithm that can track objects in any two or three-dimensional data field. Therefore, we find the optimal tracking parameters for works for IMERG and then track MCSs over the global tropics (30°N – 30°S) for ten years (2011 -2020).

The IMERG precipitation and tracked MCSs dataset are used to study the spatial variability of MCSs and their properties, such as MCS frequency, rain contribution, area, precipitation intensity (maximum rain rate), and propagation velocity. Later, we are motivated to explore the transition of peaks in the diurnal cycle from inland to the open ocean as a function of distance from the coastlines, something that has been rarely done

systematically. The tracked MCSs dataset alongside IMERG precipitation will help understand the role of MCSs and their lifecycle in the observed diurnal cycle.

1.7 References

- Albright, M. D., Recker, E. E., Reed, R. J., & Dang, R. (1985). The Diurnal Variation of Deep Convection and Inferred Precipitation in the Central Tropical Pacific During January–February 1979. *Monthly Weather Review*, *113*(10), 1663–1680. [https://doi.org/10.1175/1520-0493\(1985\)113<1663:TDVODC>2.0.CO;2](https://doi.org/10.1175/1520-0493(1985)113<1663:TDVODC>2.0.CO;2)
- Anselmo, E. M., Schumacher, C., & Machado, L. A. T. (2020). The amazonian low-level jet and its connection to convective cloud propagation and evolution. *Monthly Weather Review*, *148*(10), 4083–4099. <https://doi.org/10.1175/MWR-D-19-0414.1>
- Anselmo, E. M., Machado, L. A. T., Schumacher, C., & Kiladis, G. N. (2021). Amazonian mesoscale convective systems: Life cycle and propagation characteristics. *International Journal of Climatology*, *41*(7), 3968–3981. <https://doi.org/10.1002/joc.7053>
- Bang, S. D., & Zipser, E. J. (2015). Differences in size spectra of electrified storms over land and ocean. *Geophysical Research Letters*, *121*(15), 9048–9068. <https://doi.org/10.1002/2016JD025150>
- Bang, S. D., & Zipser, E. J. (2016). Seeking reasons for the differences in size spectra of electrified storms over land and ocean. *Journal of Geophysical Research*, *121*(15), 9048–9068. <https://doi.org/10.1002/2016JD025150>
- Berg, W., Kummerow, C., & Morales, C. A. (2002). Differences between East and West Pacific rainfall systems. *Journal of Climate*, *15*(24), 3659–3672. [https://doi.org/10.1175/1520-0442\(2002\)015<3659:DBEAWP>2.0.CO;2](https://doi.org/10.1175/1520-0442(2002)015<3659:DBEAWP>2.0.CO;2)
- Biasutti, M., Yuter, S. E., Burleyson, C. D., & Sobel, A. H. (2012). Very high resolution rainfall patterns measured by TRMM precipitation radar: Seasonal and diurnal cycles. *Climate Dynamics*, *39*(1–2), 239–258. <https://doi.org/10.1007/s00382-011-1146-6>
- Burleyson, C. D., Feng, Z., Hagos, S. M., Fast, J., Machado, L. A. T., & Martin, S. T. (2016). Spatial variability of the background diurnal cycle of deep convection around the GoAmazon2014/5 field campaign sites. *Journal of Applied Meteorology and Climatology*, *55*(7), 1579–1598. <https://doi.org/10.1175/JAMC-D-15-0229.1>
- Cecil, D. J., Goodman, S. J., Boccippio, D. J., Zipser, E. J., & Nesbitt, S. W. (2005).

- Three years of TRMM precipitation features. Part I: Radar, radiometric, and lightning characteristics. *Monthly Weather Review*, 133(3), 543–566.
<https://doi.org/10.1175/MWR-2876.1>
- Chen, S. S., & Houze, R. A. (1997a). Diurnal variation and life-cycle of deep convective systems over the tropical Pacific warm pool. *Quarterly Journal of the Royal Meteorological Society*, 123(538), 357–388. <https://doi.org/10.1256/smsqj.53805>
- Chen, S. S., & Houze, R. A. (1997b). Interannual variability of deep convection over the tropical warm pool. *Journal of Geophysical Research: Atmospheres*, 102(D22), 25783–25795. <https://doi.org/10.1029/97JD02238>
- Davis, C. A., Brown, B., & Bullock, R. (2006). Object-based verification of precipitation forecasts. Part I: Application to convective rain systems. *Monthly Weather Review*, 134(7), 1785–1795. <https://doi.org/10.1175/MWR3146.1>
- Dixon, M., & Wiener, G. (1993). TITAN: Thunderstorm Identification, Tracking, Analysis, and Nowcasting—A Radar-based Methodology. *Journal of Atmospheric and Oceanic Technology*, 10(6), 785–797.
[https://doi.org/10.1175/1520-0426\(1993\)010<0785:TTITAA>2.0.CO;2](https://doi.org/10.1175/1520-0426(1993)010<0785:TTITAA>2.0.CO;2)
- Dudhia, J. (1989). Numerical Study of Convection Observed during the Winter Monsoon Experiment Using a Mesoscale Two-Dimensional Model. *Journal of the Atmospheric Sciences*, 46(20), 3077–3107. [https://doi.org/10.1175/1520-0469\(1989\)046<3077:NSOCOD>2.0.CO;2](https://doi.org/10.1175/1520-0469(1989)046<3077:NSOCOD>2.0.CO;2)
- Feng, Z., Leung, L. R., Liu, N., Wang, J., Houze, R. A., Li, J., et al. (2021). A Global High-Resolution Mesoscale Convective System Database Using Satellite-Derived Cloud Tops, Surface Precipitation, and Tracking. *Journal of Geophysical Research: Atmospheres*, 126(8). <https://doi.org/10.1029/2020JD034202>
- Gray, W. M., & Jacobson, R. W. (1977). Diurnal Variation of Deep Cumulus Convection. *Monthly Weather Review*, 105(9), 1171–1188.
[https://doi.org/10.1175/1520-0493\(1977\)105<1171:DVODCC>2.0.CO;2](https://doi.org/10.1175/1520-0493(1977)105<1171:DVODCC>2.0.CO;2)
- Hagos, S. M., Zhang, C., Feng, Z., Burleyson, C. D., De Mott, C., Kerns, B., et al. (2016). The impact of the diurnal cycle on the propagation of Madden-Julian Oscillation convection across the Maritime Continent. *Journal of Advances in Modeling Earth Systems*, 8(4), 1552–1564.
<https://doi.org/10.1002/2016MS000725>
- Hartmann, D. L., Hendon, H. H., & Houze, R. A. (1984). Some Implications of the Mesoscale Circulations in Tropical Cloud Clusters for Large-Scale Dynamics and Climate. *Journal of the Atmospheric Sciences*, 41(1), 113–121.
[https://doi.org/10.1175/1520-0469\(1984\)041<0113:SIOTMC>2.0.CO;2](https://doi.org/10.1175/1520-0469(1984)041<0113:SIOTMC>2.0.CO;2)

- Hayden, L., Liu, C., & Liu, N. (2021). Properties of Mesoscale Convective Systems Throughout Their Lifetimes Using IMERG, GPM, WLLN, and a Simplified Tracking Algorithm. *Journal of Geophysical Research: Atmospheres*, 126(20), 1–21. <https://doi.org/10.1029/2021JD035264>
- Houze, Jr., R. A. (1982). Cloud Clusters and Large-Scale Vertical Motions in the Tropics. *Journal of the Meteorological Society of Japan. Ser. II*, 60(1), 396–410. https://doi.org/10.2151/jmsj1965.60.1_396
- Houze Jr, R. A. (2004). Mesoscale Convective Systems-Review paper. *Reviews of Geophysics*, 42, 1–43. <https://doi.org/10.1029/2004RG000150.1.INTRODUCTION>
- Houze, R. A., & Betts, A. K. (1981). Convection in GATE. *Reviews of Geophysics*, 19(4), 541. <https://doi.org/10.1029/RG019i004p00541>
- Houze, R. A., Geotis, S. G., Marks, F. D., & West, A. K. (1981). Winter Monsoon Convection in the Vicinity of North Borneo. Part I: Structure and Time Variation of the Clouds and Precipitation. *Monthly Weather Review*, 109(8), 1595–1614. [https://doi.org/10.1175/1520-0493\(1981\)109<1595:WMCITV>2.0.CO;2](https://doi.org/10.1175/1520-0493(1981)109<1595:WMCITV>2.0.CO;2)
- Houze, R. A., Rasmussen, K. L., Zuluaga, M. D., & Brodzik, S. R. (2015). The variable nature of convection in the tropics and subtropics: A legacy of 16 years of the Tropical Rainfall Measuring Mission satellite. *Reviews of Geophysics*, 53(3), 994–1021. <https://doi.org/10.1002/2015RG000488>
- Janiga, M. A., & Thorncroft, C. D. (2016). The influence of African easterly waves on convection over tropical Africa and the east Atlantic. *Monthly Weather Review*, 144(1), 171–192. <https://doi.org/10.1175/MWR-D-14-00419.1>
- Johnson, J. T., Mackeen, P. L., Witt, A., Mitchell, E. D., Stumpf, G. J., Eilts, M. D., & Thomas, K. W. (1998). The storm cell identification and tracking algorithm: An enhanced WSR-88D algorithm. *Weather and Forecasting*, 13(2), 263–276. [https://doi.org/10.1175/1520-0434\(1998\)013<0263:TSCIAT>2.0.CO;2](https://doi.org/10.1175/1520-0434(1998)013<0263:TSCIAT>2.0.CO;2)
- Kingsmill, D. E., & Houze Jr, R. a. (1999). Kinematic characteristics of air flowing into and out of precipitating convection over the west Pacific warm pool: An airborne Doppler radar survey. *Quarterly Journal of the Royal Meteorological Society*, 125(556), 1165–1207. <https://doi.org/10.1256/smsqj.55604>
- Leary C. A., Houze, R. (1979). The structure and evolution of convection in a tropical cloud cluster. *Journal of the Atmospheric Sciences*.
- Liu, C. (2011). Rainfall Contributions from Precipitation Systems with Different Sizes, Convective Intensities, and Durations over the Tropics and Subtropics. *Journal of Hydrometeorology*, 12(3), 394–412. <https://doi.org/10.1175/2010JHM1320.1>

- Liu, C., & Zipser, E. J. (2005). Global distribution of convection penetrating the tropical tropopause. *Journal of Geophysical Research Atmospheres*, *110*(23), 1–12. <https://doi.org/10.1029/2005JD006063>
- Liu, C., & Zipser, E. J. (2008). Diurnal cycles of precipitation, clouds, and lightning in the tropics from 9 years of TRMM observations. *Geophysical Research Letters*, *35*(4), 1–6. <https://doi.org/10.1029/2007GL032437>
- Liu, C., Zipser, E. J., & Nesbitt, S. W. (2007). Global distribution of tropical deep convection: Different perspectives from TRMM infrared and radar data. *Journal of Climate*, *20*(3), 489–503. <https://doi.org/10.1175/JCLI4023.1>
- Mapes, B. E., & Houze, R. A. (1993). Cloud Clusters and Superclusters over the Oceanic Warm Pool. *Monthly Weather Review*, *121*(5), 1398–1416. [https://doi.org/10.1175/1520-0493\(1993\)121<1398:CCASOT>2.0.CO;2](https://doi.org/10.1175/1520-0493(1993)121<1398:CCASOT>2.0.CO;2)
- Maranan, M., Fink, A. H., Knippertz, P., Francis, S. D., Akpo, A. B., Jegede, G., & Yorke, C. (2019). Interactions between convection and a moist vortex associated with an extreme rainfall event over southern West Africa. *Monthly Weather Review*, *147*(7), 2309–2328. <https://doi.org/10.1175/MWR-D-18-0396.1>
- Martin, D. W., & Schreiner, A. J. (1981). Characteristics of West African and East Atlantic Cloud Clusters: A Survey from GATE. *Monthly Weather Review*, *109*(8), 1671–1688. [https://doi.org/10.1175/1520-0493\(1981\)109<1671:COWAAE>2.0.CO;2](https://doi.org/10.1175/1520-0493(1981)109<1671:COWAAE>2.0.CO;2)
- Mathon, V., & Laurent, H. (2001). Life cycle of Sahelian mesoscale convective cloud systems. *Quarterly Journal of the Royal Meteorological Society*, *127*(572), 377–406. <https://doi.org/10.1256/smsqj.57207>
- Matthews, A. J., & Kiladis, G. N. (2000). A Model of Rossby Waves Linked to Submonthly Convection over the Eastern Tropical Pacific. *Journal of the Atmospheric Sciences*, *57*(23), 3785–3798. [https://doi.org/10.1175/1520-0469\(2000\)057<3785:AMORWL>2.0.CO;2](https://doi.org/10.1175/1520-0469(2000)057<3785:AMORWL>2.0.CO;2)
- McGarry, M. M., & Reed, R. J. (1978). Diurnal Variations in Convective Activity and Precipitation During Phases II and III of GATE. *Monthly Weather Review*, *106*(1), 101–113. [https://doi.org/10.1175/1520-0493\(1978\)106<0101:DVICAA>2.0.CO;2](https://doi.org/10.1175/1520-0493(1978)106<0101:DVICAA>2.0.CO;2)
- Murakami, T. (1972). Equatorial Tropospheric Waves Induced by Diabatic Heat Sources. *Journal of the Atmospheric Sciences*, *29*(5), 827–836. [https://doi.org/10.1175/1520-0469\(1972\)029<0827:ETWIBD>2.0.CO;2](https://doi.org/10.1175/1520-0469(1972)029<0827:ETWIBD>2.0.CO;2)
- Nesbitt, S. W., & Zipser, E. J. (2000). A census of precipitation features in the tropics using TRMM: Radar, ice scattering, and lightning observations. *Journal of*

- Climate*, 13(23), 4087–4106. [https://doi.org/10.1175/1520-0442\(2000\)013<4087:ACOPFI>2.0.CO;2](https://doi.org/10.1175/1520-0442(2000)013<4087:ACOPFI>2.0.CO;2)
- Nesbitt, Stephen W., & Zipser, E. J. (2003). The diurnal cycle of rainfall and convective intensity according to three years of TRMM measurements. *Journal of Climate*, 16(10), 1456–1475. <https://doi.org/10.1175/1520-0442-16.10.1456>
- Nesbitt, Stephen W., Zipser, E. J., & Cecil, D. J. (2000). A Census of Precipitation Features in the Tropics Using TRMM: Radar, Ice Scattering, and Lightning Observations. *Journal of Climate*, 13(23), 4087–4106. [https://doi.org/10.1175/1520-0442\(2000\)013<4087:ACOPFI>2.0.CO;2](https://doi.org/10.1175/1520-0442(2000)013<4087:ACOPFI>2.0.CO;2)
- Núñez Ocasio, K. M., Evans, J. L., & Young, G. S. (2020). Tracking Mesoscale Convective Systems that are Potential Candidates for Tropical Cyclogenesis. *Monthly Weather Review*, 148(2), 655–669. <https://doi.org/10.1175/MWR-D-19-0070.1>
- Poveda, G., Espinoza, J. C., Zuluaga, M. D., Solman, S. A., Garreaud, R., & van Oevelen, P. J. (2020). High Impact Weather Events in the Andes. *Frontiers in Earth Science*, 8(May), 1–32. <https://doi.org/10.3389/feart.2020.00162>
- Rydbeck, A. V., & Maloney, E. D. (2015). On the convective coupling and moisture organization of East Pacific easterly waves. *Journal of the Atmospheric Sciences*, 72(10), 3850–3870. <https://doi.org/10.1175/JAS-D-15-0056.1>
- Schumacher, C., & Houze, R. A. (2003). Stratiform rain in the tropics as seen by the TRMM precipitation radar. *Journal of Climate*, 16(11), 1739–1756. [https://doi.org/10.1175/1520-0442\(2003\)016<1739:SRITTA>2.0.CO;2](https://doi.org/10.1175/1520-0442(2003)016<1739:SRITTA>2.0.CO;2)
- Schumacher, C., Houze, R. A., & Kraucunas, I. (2004). The tropical dynamical response to latent heating estimates derived from the TRMM precipitation radar. *Journal of the Atmospheric Sciences*, 61(12), 1341–1358. [https://doi.org/10.1175/1520-0469\(2004\)061<1341:TTDRTL>2.0.CO;2](https://doi.org/10.1175/1520-0469(2004)061<1341:TTDRTL>2.0.CO;2)
- Silva Dias, M. A. F., Rutledge, S., Kabat, P., Silva Dias, P. L., Nobre, C., Fisch, G., et al. (2002). Cloud and rain processes in a biosphere-atmosphere interaction context in the Amazon Region. *Journal of Geophysical Research Atmospheres*, 107(20). <https://doi.org/10.1029/2001JD000335>
- Skok, G., Tribbia, J., Rakovec, J., & Brown, B. (2009). Object-based analysis of satellite-derived precipitation systems over the low- and mid-latitude Pacific Ocean. *Monthly Weather Review*, 137(10), 3196–3218. <https://doi.org/10.1175/2009MWR2900.1>
- Skok, G., Bacmeister, J., & Tribbia, J. (2013). Analysis of Tropical Cyclone Precipitation Using an Object-Based Algorithm. *Journal of Climate*, 26(8), 2563–2579.

<https://doi.org/10.1175/JCLI-D-12-00135.1>

- Whitehall, K., Mattmann, C. A., Jenkins, G., Rwebangira, M., Demoz, B., Waliser, D., et al. (2015). Exploring a graph theory based algorithm for automated identification and characterization of large mesoscale convective systems in satellite datasets. *Earth Science Informatics*, 8(3), 663–675. <https://doi.org/10.1007/s12145-014-0181-3>
- Williams, M., Houze, R. (1987). Satellite-Observed Characteristics of Winter Monsoon Cloud Clusters. *Monthly Weather Review*, 5(1), 1–8. [https://doi.org/https://doi.org/10.1175/1520-0493\(1987\)115<0505:SOCOWM>2.0.CO;2](https://doi.org/https://doi.org/10.1175/1520-0493(1987)115<0505:SOCOWM>2.0.CO;2)
- Woodley, W. L., Griffith, C. G., Griffin, J. S., & Stromatt, S. C. (1980). The Inference of GATE Convective Rainfall from SMS-1 Imagery. *Journal of Applied Meteorology*, 19(4), 388–408. [https://doi.org/10.1175/1520-0450\(1980\)019<0388:TIOGCR>2.0.CO;2](https://doi.org/10.1175/1520-0450(1980)019<0388:TIOGCR>2.0.CO;2)
- Yang, G. Y., & Slingo, J. (2001). The diurnal cycle in the tropics. *Monthly Weather Review*, 129(4), 784–801. [https://doi.org/10.1175/1520-0493\(2001\)129<0784:TDCITT>2.0.CO;2](https://doi.org/10.1175/1520-0493(2001)129<0784:TDCITT>2.0.CO;2)
- Zipser, E. J. (1977). Mesoscale and Convective–Scale Downdrafts as Distinct Components of Squall-Line Structure. *Monthly Weather Review*, 105(12), 1568–1589. [https://doi.org/10.1175/1520-0493\(1977\)105<1568:MACDAD>2.0.CO;2](https://doi.org/10.1175/1520-0493(1977)105<1568:MACDAD>2.0.CO;2)
- Zipser, E. J., Cecil, D. J., Liu, C., Nesbitt, S. W., & Yorty, D. P. (2006). Where are the most intense thunderstorms on earth? *Bulletin of the American Meteorological Society*, 87(8), 1057–1072. <https://doi.org/10.1175/BAMS-87-8-1057>

CHAPTER 2

COMPARISONS OF IMERG VERSION 06 PRECIPITATION AT AND BETWEEN PASSIVE MICROWAVE OVERPASSES IN THE TROPICS

Reproduced with <yet to receive permission> from Rajagopal, M., Zipser, E., Huffman, G., Russell, J., & Tan, J. (2021). Comparisons of IMERG Version 06 Precipitation at and between Passive Microwave Overpasses in the Tropics, *Journal of Hydrometeorology*, 22(8), 2117-2130.



Comparisons of IMERG Version 06 Precipitation at and between Passive Microwave Overpasses in the Tropics

MANIKANDAN RAJAGOPAL,^a EDWARD ZIPSER,^a GEORGE HUFFMAN,^b JAMES RUSSELL,^a AND JACKSON TAN^{b,c}

^a *University of Utah, Salt Lake City, Utah*

^b *NASA Goddard Space Flight Center, Greenbelt, Maryland*

^c *Universities Space Research Association, Columbia, Maryland*

(Manuscript received 22 September 2020, in final form 25 June 2021)

ABSTRACT: The Integrated Multisatellite Retrievals for Global Precipitation Measurement Mission (IMERG) is a global precipitation product that uses precipitation retrievals from the virtual constellation of satellites with passive microwave (PMW) sensors, as available. In the absence of PMW observations, IMERG uses a Kalman filter scheme to morph precipitation from one PMW observation to the next. In this study, an analysis of convective systems observed during the Convective Process Experiment (CPEX) suggests that IMERG precipitation depends more strongly on the availability of PMW observations than previously suspected. Following this evidence, we explore systematic biases in IMERG through bulk statistics. In two CPEX case studies, cloud photographs, pilot's radar, and infrared imagery suggest that IMERG represents the spatial extent of precipitation relatively well when there is a PMW observation but sometimes produces spurious precipitation areas in the absence of PMW observations. Also, considering an observed convective system as a precipitation object in IMERG, the maximum rain rate peaked during PMW overpasses, with lower values between them. Bulk statistics reveal that these biases occur throughout IMERG Version 06. We find that locations and times without PMW observations have a higher frequency of light precipitation rates and a lower frequency of heavy precipitation rates due to retrieval artifacts. These results reveal deficiencies in the IMERG Kalman filter scheme, which have led to the development of the Scheme for Histogram Adjustment with Ranked Precipitation Estimates in the Neighborhood (SHARPEN; described in a companion paper) that will be applied in the next version of IMERG.

KEYWORDS: Tropics; Mesoscale systems; Precipitation; Satellite observations; Field experiments

1. Introduction

Precipitation has direct impacts on human populations through natural disasters (e.g., Bodenreider et al. 2019; Paul et al. 2019) and by influencing the global economy through agriculture (e.g., Zhang et al. 2012; Sohoulane et al. 2019) and commerce (Steinker et al. 2017; Verstraete et al. 2019). Satellites are crucial for observing atmospheric variables, including precipitation, over remote locations such as oceans and mountains, where surface observations are often scarce. The most detailed precipitation measurement from space is possible through the precipitation radar on board the Tropical Rainfall Measuring Mission (TRMM; Kummerow et al. 1998) satellite and its successor, the Global Precipitation Measurement mission (GPM; Hou et al. 2014) *Core Observatory* satellite. The cloud radar on board the *CloudSat* satellite is

complementary to the precipitation radars since it is sensitive to light snow and rain (Hayden and Liu 2018). These precipitation and cloud radars have extremely sparse revisit times, so long-term global satellite precipitation products use passive microwave (PMW) sensor observations. These long-term precipitation records help us understand the hydrological cycle and climate change impacts at global and regional scales. These records include satellite precipitation data such as the Global Precipitation Climatology Project (GPCP; Huffman et al. 1997; Adler et al. 2018) and the TRMM Multisatellite Precipitation Analysis (TMPA; Huffman et al. 2007), which have regularly been used to study recent climate trends (e.g., Gu et al. 2007; Zhou et al. 2015). Despite their value in climate analyses, both GPCP and TMPA have relatively coarse time-space resolution; TMPA, for example, is available every 3 h with a spatial resolution of $0.25^\circ \times 0.25^\circ$ (Huffman et al. 2007). This relatively coarse temporal resolution makes TMPA less suitable for studying important objects in precipitation fields such as mesoscale convective systems (MCSs), which can produce severe weather events that cause damage through strong winds, floods, and hail (Akaeda et al. 1995; McCollum et al. 1995). Also, MCSs contribute more than 50% of annual rainfall in the tropics (Mohr et al. 1999; Nesbitt et al. 2006; Liu 2011).

Supplemental information related to this paper is available at the Journals Online website: <https://doi.org/10.1175/JHM-D-20-0226.s1>.

Corresponding author: Manikandan Rajagopal, mani.rajagopal@utah.edu

DOI: 10.1175/JHM-D-20-0226.1

© 2021 American Meteorological Society. For information regarding reuse of this content and general copyright information, consult the AMS Copyright Policy (www.ametsoc.org/PUBSReuseLicenses).

Brought to you by UNIVERSITY OF UTAH | Unauthenticated | Downloaded 08/05/21 11:59 PM UTC

The Integrated Multisatellite Retrievals for GPM (IMERG), the successor to TMPA, is a global precipitation product at a spatial resolution of $0.1^\circ \times 0.1^\circ$, available every 30 min, and is therefore more suitable to investigate MCSs and better resolve precipitation events. IMERG follows the pioneering TMPA approach, achieving near-global coverage by taking advantage of a virtual constellation (because their orbits are not coordinated) of low-Earth-orbit (LEO) satellites with PMW sensors. At the locations with PMW observations, IMERG uses the Goddard profiling algorithm (GPROF2017) that converts PMW brightness temperature (T_b) to precipitation estimates for various PMW sensors (Kummerow et al. 2015; Randel et al. 2020), except the Sounder for Probing Vertical Profiles of Humidity (SAPHIR), for which the Precipitation Retrieval and Profiling Scheme (PRPS) is employed (Kidd 2018). At locations without PMW observations, IMERG uses a time morphing scheme, based on Kalman filter (Joyce and Xie 2011), to estimate precipitation.

For both weather and climate research, it is vital to understand the strengths and limitations of IMERG precipitation. Past validation studies compared GPROF precipitation estimates for various PMW sensors to the GPM Dual-Frequency Precipitation Radar (DPR), rain gauges, or ground radar. They show that GPROF overestimates light precipitation rates and underestimates heavy precipitation rates (Tan et al. 2018; Kidd et al. 2018; You et al. 2020). In addition to differences in estimates, they found that PMW precipitation has a higher frequency of light rain rates and a lower occurrence of heavy precipitation rates than surface observations. The higher frequency of light precipitation rates may be attributed to the Bayesian nature of the GPROF algorithm, where the observed PMW brightness temperatures are matched to the closest values in a priori database. For each pixel, this produces multiple matches, i.e., multiple surface precipitation rates, including zeros. The Bayesian averaging of multiple values at each pixel results in fewer zeros and a higher frequency of light rain rates. IMERG uses GPROF precipitation after removing unreasonably low rain rates through thresholding and histogram adjustment to combined radar-radiometer precipitation. The past validation studies have evaluated GPROF precipitation estimates with observations, but there are fewer studies (Tan et al. 2016; Maranan et al. 2020) that examined IMERG precipitation estimates from the morphing algorithm, which is the focus of this work.

The studies mentioned above and many others (Gaona et al. 2016; Tan et al. 2017; Sungmin et al. 2017; Sharifi et al. 2016; Asong et al. 2017; Watters et al. 2018; Bytheway et al. 2020; Tapiador et al. 2020; Gowan and Horel 2020) involve point-to-point comparisons of GPROF or IMERG precipitation with other observations at different space and time resolutions. As an alternative to the point-to-point comparison, an object-based approach (e.g., Davis et al. 2006; Johnson et al. 2013) has recently been introduced for evaluating reanalyses, model forecasts, and other global gridded products. This entails identifying objects in the fields of interest and establishing biases or errors based on these objects' properties. However, object-based approaches to validating IMERG are rare. Cui et al. (2020) compared MCSs tracked in IMERG with MCSs

defined using ground-based radar precipitation estimates over the continental United States from 2014 to 2016. They found that MCSs in IMERG had systematically larger precipitation areas and higher precipitation volume than radar-observed objects. To our knowledge, there have not been similar object-based approaches to the validation of IMERG algorithmic components over tropical oceans.

In this work, we use an object-based approach and the aircraft data from two case studies from the Convective Processes Experiment (CPEX) to investigate the representation of MCSs in IMERG. These MCSs represented as IMERG precipitation objects occasionally exhibit an unrealistic change in precipitation area and maximum rain rate in the absence of PMW observations. Since these case studies are too few to provide definitive bias characteristics, we use bulk statistics to show the systematic differences between IMERG precipitation estimates from the GPROF and morphing algorithms.

The rest of the article is structured as follows. Section 2 describes the CPEX field program and the DC-8 aircraft instrumentation with the forward camera and pilot's radarscope used to compare with IMERG precipitation estimates. Then, we summarize the IMERG V06 Final Run procedure to estimate precipitation both during and, with greater complexity, between PMW overpasses. Section 3 presents the subjective tracking of MCSs and their properties inferred from IMERG for two case studies from the CPEX field program. Then a method for constructing precipitation rate distributions over the tropics from 2001 to 2019 is outlined. Results presented in section 4 show specific differences in IMERG precipitation during and between PMW overpasses, both for two case studies and bulk statistics from 2001 to 2019. Section 5 discusses these findings, and section 6 summarizes the conclusions.

2. Data

a. CPEX aircraft data

CPEX was a National Aeronautics and Space Administration (NASA) sponsored field program conducted in May–June 2017. The DC-8 aircraft carried a range of remote sensing instruments to measure vertical profiles of temperature, humidity, wind, and hydrometeors to study the environmental conditions and the convection. Also, the aircraft had a forward camera, a nadir camera, and a pilot's radarscope that provided visual references. During its 100 flight hours, the DC-8 investigated MCSs over the Gulf of Mexico, the Caribbean Sea, and the western Atlantic. The forward camera and forward-looking pilot's radar give a holistic view of each MCS and are more valuable for IMERG validation than the downward-pointing aircraft precipitation radar. This is because the aircraft precipitation radar resolution and its swath are smaller than most PMW sensor footprints, rendering their comparisons less useful. The IMERG animation overlaid with the aircraft track, position, and heading are visually compared with the forward camera and pilot's radar from multiple CPEX missions. Only the evaluation for MCSs observed on 6 and 10 June 2017, are

presented here. They both highlight the differences in IMERG precipitation during and between PMW overpasses.

b. IMERG Version 06

IMERG precipitation products are available at three different latencies, namely, Early Run (~4 h), Late Run (~14 h), and Final Run (~3.5 months), to cater to the time-sensitivities of different applications. In this study, we use the half-hourly precipitation from the Version 06 Final Run, which is a research-quality product. IMERG uses multiple algorithms/procedures for intercalibration, precipitation estimates, and bias corrections. Also, there exist differences in algorithmic steps between different runs. Since we use the half-hourly Final Run in this study, only its algorithmic components will be summarized here. Information on other runs, daily, and monthly products are available in the technical documentation and algorithm theoretical basis document (Huffman et al. 2020a,b).

IMERG uses observations from a virtual constellation of LEO satellites with PMW sensors to create near-global precipitation products. The final IMERG precipitation estimate is a multistep process starting with the intercalibration of T_b of various PMW sensors against the TRMM Microwave Imager (TMI) or GPM Microwave Imager (GMI), depending on available periods of coincidence. The GPROF (Version 2017) algorithm uses a Bayesian approach to convert the intercalibrated T_b of multiple PMW frequencies of a sensor to surface precipitation (Kummerow et al. 2015). The resulting PMW precipitation has a resolution that depends on sensor frequency channels (You et al. 2020, their Table 1). These GPROF precipitation estimates are regridded to a $0.1^\circ \times 0.1^\circ$ spatial grid using nearest-neighbor interpolation. The constellation PMW precipitation rates are calibrated to TMI or GMI precipitation rates through climatological histogram matching. This removes most differences in “precipitation rate frequency distribution” that would otherwise contaminate the IMERG inputs. All the PMW precipitation fields are then dynamically calibrated to TRMM or GPM’s Combined Radar Radiometer Algorithm (CORRA; Olson et al. 2011) precipitation, which is considered superior to individual radar or radiometer precipitation.

The available PMW observations during a 30-min interval have only partial global coverage. In the gaps between PMW sensor swaths, IMERG uses the Kalman filter (KF)-based time morphing scheme, adapted from the Climate Prediction Center (CPC) morphing technique (CMORPH-KF; Joyce et al. 2004; Joyce and Xie 2011; Xie et al. 2017), to interpolate precipitation between PMW observation times. The time morphing scheme uses the Kalman filter weighted averaging to combine precipitation estimates from three sources: 1) forward propagated precipitation from the past PMW observation, 2) backward propagated precipitation from the future PMW observation, and 3) IR precipitation from geostationary satellites at the analysis time. The motion vectors used to propagate precipitation in IMERG Version 06 (Final Run) are computed from a time sequence of the total column water vapor (TCV) fields as analyzed by the Modern-Era Retrospective Analysis for Research and Applications, Version 2 (MERRA-2; Gelaro et al. 2017; Tan et al. 2019). This is a change from the earlier versions of IMERG (and CMORPH-KF) that relied on motion

vectors diagnosed from geostationary IR data. The IR precipitation input to the Kalman filter is based on the Precipitation Estimation from Remotely Sensed Information Using Artificial Neural Networks–Cloud Classification System (PERSIANN-CCS) algorithm. This algorithm converts IR cloud-top T_b gradients into precipitation estimates using neural networks, trained on coincident IR and PMW observations (Hong et al. 2004; Nguyen et al. 2018). IMERG computes the weighted average of all three sources (forward propagated, backward propagated, and IR precipitation), using Kalman filter weights that are proportional to their respective locally estimated error variance. The Kalman weight for propagated PMW precipitation decreases with increasing propagation time since the PMW observation (Joyce and Xie 2011). Tan et al. (2016) and Maranan et al. (2020) defined three groups in the absence of instantaneous PMW observations: “morph,” “IR-only,” and “morph+IR,” based on whether the Kalman filter uses propagated PMW precipitation, IR precipitation, or both. In this article, we follow Joyce and Xie (2011) and use the alternative definition for “morphing” to refer to Kalman weighted average estimates that include all three groups. In other words, “morphing” here refers to output from the Kalman filter that strives to produce a smooth transition from one PMW observation to the next.

Finally, bias corrections computed using monthly rain gauge data from the Global Precipitation Climatology Center (GPCC; Schneider et al. 2014) are applied to merged precipitation fields from PMW and morphing. We use these gauge calibrated precipitation fields to compute bulk statistics; however, using the uncalibrated precipitation yielded similar results.

In addition to the estimated precipitation, each half-hour data file has variables to identify the source of precipitation estimates (Tan et al. 2016). The variable “HQprecipSource” has a PMW sensor index value for each grid cell, including the value zero when there is no PMW observation. The variable “IRkalmanFilterWeight” has Kalman weights for IR precipitation expressed in percentage, and the remaining percentage is the weight assigned to propagated PMW precipitation. In the half-hour interval immediately before and after a PMW observation, the morphing algorithm weights only the forward and backward propagated PMW precipitation. Hence, the “IRkalmanFilterWeight” is zero in such locations. More than 30 min away from a PMW observation, the morphing algorithm weights together forward propagated, backward propagated, and IR precipitation. The complete list of data variables, description, and index values for various PMW sensors are available in the IMERG documentation (Huffman et al. 2020a,b).

3. Methods

a. MCSs: Tracking and properties

The initial focus of our analyses is two MCSs that the DC-8 aircraft investigated during the CPEX field campaign. At 0900 UTC 6 June 2017, an MCS started as an isolated convective system (Fig. 1). Later, around 1300 UTC, the system connected with the adjacent precipitation area of low rain rates ($<4 \text{ mm h}^{-1}$), but the MCS remained distinct and subjectively

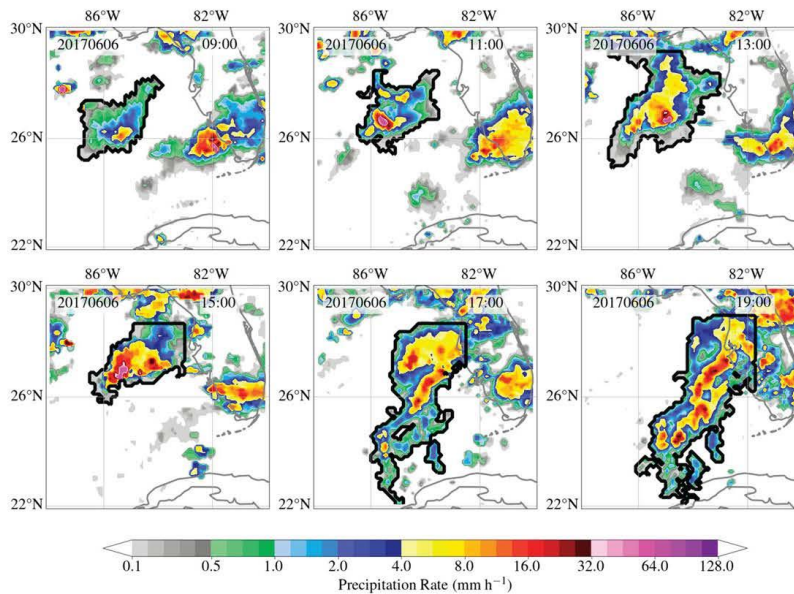


FIG. 1. The MCS observed on 6 June 2017, during the CPEX field program, is tracked as the IMERG precipitation object from 0900 to 2200 UTC. The multipanel figure shows a snapshot every 2 h with the object boundary denoted by a black contour.

identifiable. In the next 6 h, it grew upscale to become a large and intense MCS at 1900 UTC. At about 2200 UTC, the system merged with a precipitation band that extended into the western Atlantic. After this merger, the tracking was stopped because the MCS was indistinguishable from the contiguous precipitation band. Figure 1 shows the 2-h snapshots from the subjective tracking with the object boundary marked by a black contour. Though objective tracking is more desirable than a subjective method, most tracking algorithms define MCSs as contiguous precipitation areas. Such a traditional definition is not suitable for IMERG. Figure 2 from the broader region shows multiple MCSs connected by low precipitation rates to form a single contiguous area that extends thousands of kilometers. This contiguous area cannot be defined as a single MCS.

The MCS from the 6 June case study undergoes multiple mergers and splits. We looked at the IMERG animation repeatedly to discern the precipitation area that can be deemed an MCS. If an embedded cell breaks away and merges with a neighboring MCS, we exclude it from the MCS boundary in previous time steps. Similarly, if a cell joins with the MCS under study, we include it within the object boundary in the previous time steps. The IMERG animation is provided as supplemental material for the reader's reference. Choosing a different MCS boundary by including or excluding small cells will somewhat affect metrics such as area and rain volume; however, our conclusion remains the same.

On 10 June 2017, the DC-8 examined a small MCS in the western Atlantic near 73°W and 25°N. Manual identification of the MCS boundary in IMERG was more straightforward due to its isolated nature. This MCS was tracked until it dissipated on 11 June at 0200 UTC (Fig. 3).

For both MCSs, defined as IMERG objects, we compute the precipitation area, volumetric rain rate, and maximum rain rate at each half-hour from IMERG precipitation. The volumetric rain rate ($\text{mm km}^2 \text{h}^{-1}$) at each pixel is the product of the precipitation rate and the area. For an MCS, it is the sum over all pixels in the MCS of the volumetric rain rate at each pixel. Although rain volume is a time-integrated variable, we use it interchangeably with the volumetric rain rate. Also, despite the technical difference between "precipitation" and "rain," we use them interchangeably since all surface precipitation in these cases was rain.

b. Constructing precipitation rate distributions

In section 4c, we examine the frequency distribution of precipitation rates for nearly the full length of the IMERG record and global tropics extending from 30°N to 30°S. Following Tan et al. (2016, 2018) and Sungmin et al. (2017), we use a minimum threshold of 0.1 mm h^{-1} to determine if a grid cell is precipitating. We repeated this analysis for different thresholds such as 0.2 and 0.3 mm h^{-1} (figures not shown), and our conclusions are not sensitive to these choices.

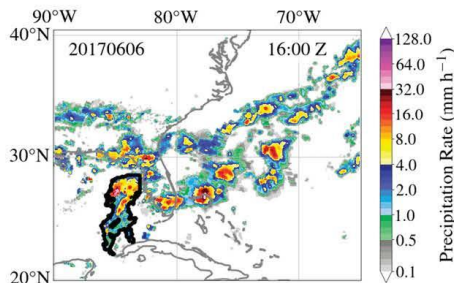


FIG. 2. The MCS from the CPEX case study on 6 June 2017, marked by a black contour, is connected to the neighboring MCSs by low precipitation rates. If the traditional object definition of contiguous area is used, the MCS will span thousands of kilometers.

The precipitating grid cells are categorized into different sources based on variables “HQprecipSource” and “IRkalmanFilterWeight,” as discussed in section 2b. Then, a precipitation rate distribution is computed for each source as a probability density function (PDF) (Lamb and Verlinde 2011). The resulting PDF will have the area under the curve equal to 1.0.

In some analyses, IMERG sources are combined into two broad categories—“All PMW” and “Morphing.” The “All PMW” category includes instantaneous precipitation estimates from all the PMW sensors and represents precipitation at locations with PMW observations. The “Morphing” category represents precipitation estimates from the Kalman filter at locations without PMW observations, which could be either propagated PMW or IR, or propagated PMW + IR. We also compute the precipitation rate distributions for these two broad categories.

The long-term statistics are essential to remove temporal variations and detect the systematic differences between PMW precipitation and morphing estimates. To reduce computation, we randomly selected 19 000 half-hour IMERG data files from 2001 to 2019 (with 1000 files per year). The PDF computed for each half-hour file is averaged over 19 000 files to produce a mean distribution. To test if 19 000 files are an adequate sample size to capture the systematic biases, we used a different random seed to select a new set of 19 000 half-hour files. The new sample set had PDFs similar to the original sample set with negligible differences (figure not shown), implying that 19 000 half-hour data were sufficient.

c. Computing precipitation occurrence (%)

In the global tropics, only a percentage of grid cells receive precipitation in a 30-min interval. The tropical precipitation

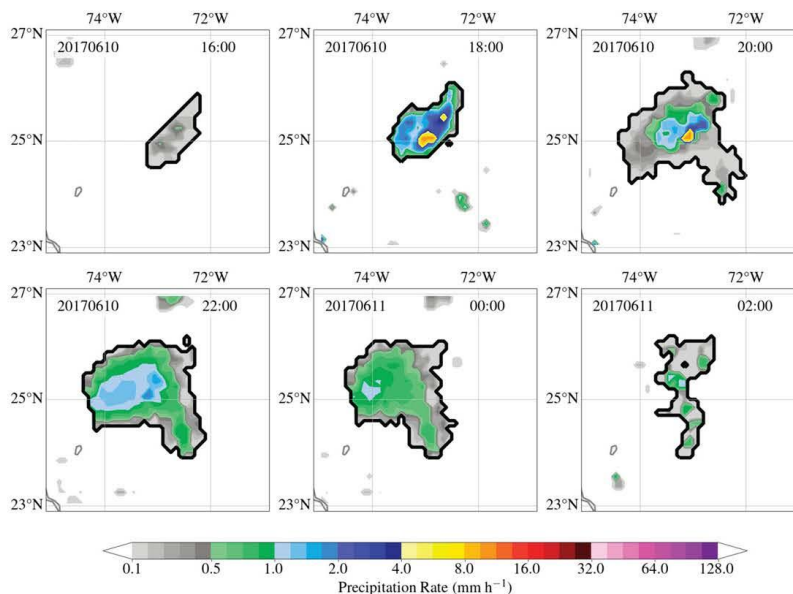


FIG. 3. The MCS observed on 10 June 2017, during the CPEX field program, is tracked as the IMERG precipitation object from 1600 to 0200 UTC the next day. The multipanel figure shows 2-h snapshots with MCS boundary marked by a black contour.

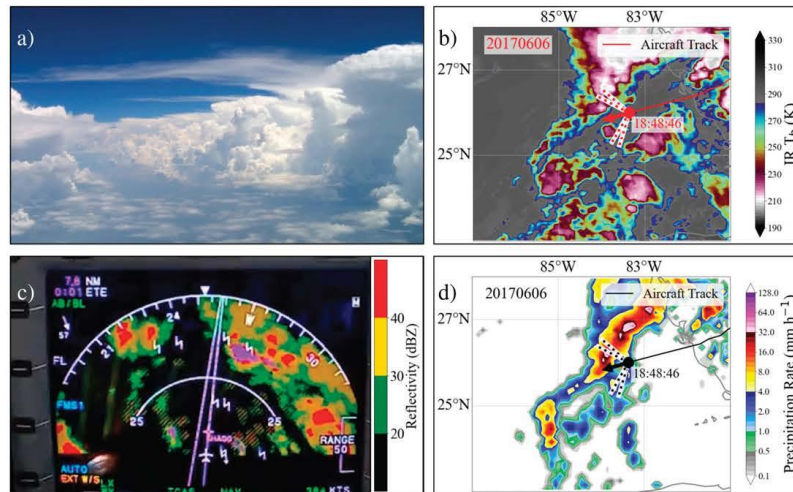


FIG. 4. Images from the CPEX mission on 6 June 2017 around 1848 UTC: (a) the DC-8 aircraft's forward camera, (b) Merged-IR data at 1900 UTC, (c) the DC-8 aircraft pilot's radar with range circles at 25 and 50 nm (1 nm = 1852 m), and (d) IMERG precipitation for the half-hour period 1830–1900 UTC. Infrared and IMERG images are overlaid with the DC-8 track (red and black line, respectively). The red/black dot represents the DC-8 aircraft location, the arrow points in the direction of the aircraft heading, and the two dotted lines represent the minimum (88°) and maximum (115°) horizontal field of view (FOV) for the forward camera.

occurrence varies temporally, and for the current climate, it will follow a certain distribution with a spread that represents the temporal variability. For each half-hour data, locations between 30°N and 30°S with and without PMW observations are grouped as “PMW” and “Morphing” grid cells, respectively. For each category, we determine precipitation occurrence, expressed as “percentage of grid cells with precipitation.”

We compute precipitation occurrence for randomly selected 19 000 half-hour files from 2001 to 2019 (with 1000 files per year). The histogram of precipitation occurrence for 19 000 half-hour data exhibits the variability in precipitation occurrence and the systematic bias between PMW precipitation and morphing estimates.

IMERG has precipitation rates below $10^{-3} \text{ mm h}^{-1}$, so the precipitation occurrence depends on the choice of minimum threshold. We apply various subjective thresholds 0.1, 0.5, 1.0, and 2.0 mm h^{-1} to understand their effects on precipitation occurrence.

4. Results

The following subsections describe differences in IMERG precipitation during and between PMW overpasses. First, we demonstrate the differences through two case studies investigated during the CPEX field campaign. Following the CPEX case studies, we use bulk statistics to confirm that the biases are

systematic by comparing precipitation rate distributions between locations with and without PMW observations.

a. Case study 1: 6 June 2017

The DC-8 aircraft mission on 6 June 2017 investigated a precipitation system extending from the central Gulf of Mexico northeastward to Florida's west coast. Figures 4b and 4d show the aircraft's location, just before making its first penetration of the convective system, about 200 km off Florida's west coast. The aircraft track, position, and heading are overlaid on IR T_b and IMERG precipitation fields. We use the merged-IR product (Janowiak et al. 2001) available every 30 min centered on the hour and half-hour. For example, in Fig. 4b, the IR T_b at 1900 UTC is from the observation period 1845–1915 UTC. However, the IMERG precipitation (Fig. 4d) is for the period 1830–1900 UTC. We use the IR data at 1900 UTC and not 1830 UTC because they are closest to the aircraft observation at 1848 UTC and PMW overpass at 1853 UTC.

The forward camera has a minimum and maximum horizontal field of view (FOV) of 88° and 115°, respectively. They are marked on IMERG and IR images to reference the area being viewed. The forward camera (Fig. 4a) clearly shows vigorous mature convective towers extending well above the aircraft altitude of approximately 32 000 ft (9800 m), which matches with heavily precipitating grid cells in IMERG. The pilot's radar also shows a long convective line oriented from

TABLE 1. DC-8 aircraft pilot's radar reflectivity codes (for signal gain set at calibration) based on IntuVue RDR-4000 Weather Radar Pilot's Guide. N/A indicates "not applicable."

Color	Returns	Reflectivity (dBZ)	Rainfall rate (mm h^{-1})
Black	Very light, or none	<20	<0.7
Green	Light	20–30	0.7–4
Yellow	Medium	30–40	4–12
Red	Strong	≥ 40	>12
Magenta	Turbulence	N/A	N/A

southwest to northeast, similar to the precipitation band on IMERG. Table 1 provides the pilot radar's reflectivity scale and corresponding rainfall rates. IMERG precipitation for this period was retrieved from the Advanced Microwave Scanning Radiometer (AMS-R-2), a PMW sensor, with an overpass around 1853 UTC, which is close to the aircraft observation time at 1848 UTC. These aircraft observations indicate that IMERG represents the observed convection qualitatively well at this PMW observation time. However, upon examination of the time series of this MCS, we note discrepancies between the PMW overpasses.

The MCS is subjectively tracked in IMERG and its properties such as precipitation area, rain volume, and maximum rain rate are diagnosed as described in section 3a. Figure 5 presents the time series of these MCS properties with PMW sensor names annotated on the x axis if there is an overpass in that half-hour period. The time series show that the MCS's maximum precipitation rate peaks near 80 mm h^{-1} several times when there are PMW overpasses. However, it "sags" to about 40 mm h^{-1} shortly before and after PMW overpasses. If we extend the MCS boundary to include adjacent cells, our conclusion does not change because most intense cells in the region are present within the current object boundary. The sagging of the maximum precipitation rate suggests a discrepancy between IMERG estimates from PMW observations and time morphing. If the MCS's maximum precipitation rate is linearly interpolated between two PMW observations, it would be a straight line connecting the peaks. However, it appears that the Kalman weighted averaging of propagated PMW and IR precipitation somehow creates this sag between the PMW overpasses, a concept that we will explore in section 5.

b. Case study 2: 10 June 2017

On 10 June 2017, the DC-8 aircraft investigated a small MCS located over the western Atlantic, approximately 100 km in each direction (east–west and north–south). The system was probably in its most active growth phase when the DC-8 aircraft approached it at 1914 UTC, at an altitude of 10 km. For the next 3 h, the aircraft penetrated and circumnavigated the MCS as it rapidly matured and entered its decay phase. Figure 6d shows the location of the DC-8 at 2030 UTC, flying at an altitude of 10 km, and its track from the previous hour overlaid on IMERG precipitation. At 2030 UTC, according to IMERG, the aircraft was about to penetrate a mesoscale

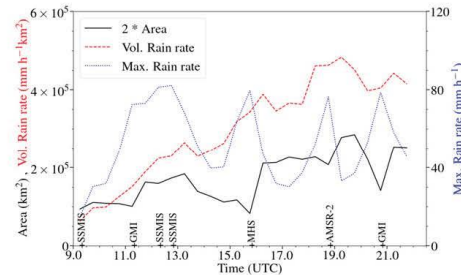


FIG. 5. Time series of the IMERG precipitation area, rain volume, and maximum rain rate of the MCS observed on the 6 June 2017 CPEX mission. Since the volumetric rain rate and precipitation area share the same y axis, the precipitation area is multiplied by a factor of 2 to make its variations more visible. PMW sensor names are annotated on the x axis at their respective half-hour overpass interval.

region of light precipitation after the turn. However, a careful inspection of the forward camera's cloud photo shows no deep or stratiform clouds but only scattered shallow cumulus. The forward camera has a minimum and maximum diagonal FOV of 100° and 126° , respectively. This is more relevant than horizontal FOV since the aircraft was making a turn. These diagonal FOVs are marked on the IMERG and IR images (Figs. 6b,d) as a reference to the area that the camera is observing. In the cloud photo, the horizon is approximately 356 km away from the aircraft's location for the flight altitude of 10 km, limiting the area viewed by the forward camera. Though the camera's FOV is limited, it is evident from the cloud photo that the area ahead does not have widespread precipitation. The 1-min camera video (provided as supplemental material) covers a much larger area that clearly shows the scattered shallow cumulus over this region as the camera's FOV swept through it when the DC-8 made the turn. Also, the pilot's radar (Fig. 6c) shows no widespread reflectivity other than a small echo ahead of the aircraft, possibly from an isolated cumulus. Since reflectivity values below 20 dBZ would mean very light rain or none (Table 1), we cannot rely solely on the radar. On the IR image (Fig. 6b) from 2030 UTC, which is closest to the aircraft observation time, we see no cold cloud top to the west of the MCS, where IMERG shows light precipitation. These pieces of evidence strongly suggest that the widespread light precipitation rates in IMERG on the west side of the MCS are spurious.

For this small MCS, Fig. 7 displays the time series of the precipitation area, rain volume, and maximum rain rate diagnosed from IMERG. In the half-hour period from 2000 to 2030 UTC, the IMERG precipitation area jumped to 3 times its previous value. This sudden growth comes from a spurious precipitation area, identified as such from the aircraft photo, pilot's radar, and IR. To trace the origin of this false precipitation, we examined the source of IMERG precipitation estimates. Figure 8 presents the MCS evolution from 1930 through

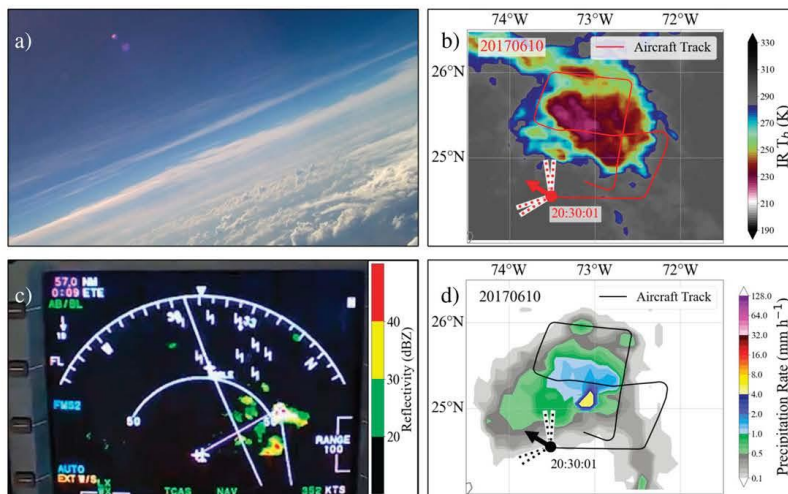


FIG. 6. Images from the CPEX mission on 10 June 2017 around 2030 UTC: (a) the DC-8 aircraft's forward camera, (b) Merged-IR data at 1830 UTC, (c) the DC-8 aircraft pilot's radar with range circles at 50 and 100 n mi. Note that the color bar in Fig. 6c differs from Fig. 4c due to different ambient lighting when recording them, and (d) IMERG precipitation for the half-hour period 2030–2100 UTC. Infrared and IMERG images are overlaid with the DC-8 track (red and black line, respectively). The red/black dot represents the DC-8 aircraft location, the arrow points in the direction of the aircraft heading, and the two dotted lines represent the minimum (100°) and maximum (126°) diagonal field of view (FOV) for the forward camera.

2300 UTC with the sources annotated in blue font. There were PMW observations at 1930 and 2300 UTC from a Microwave Humidity Sensor (MHS) and Special Sensor Microwave Imager/Sounder (SSMIS), respectively. At the time of the

aircraft observation (1830 UTC), the precipitation estimates were from the weighted average of propagated PMW and IR. Hence this spurious precipitation is likely an artifact from the morphing algorithm, as will be discussed in section 5.

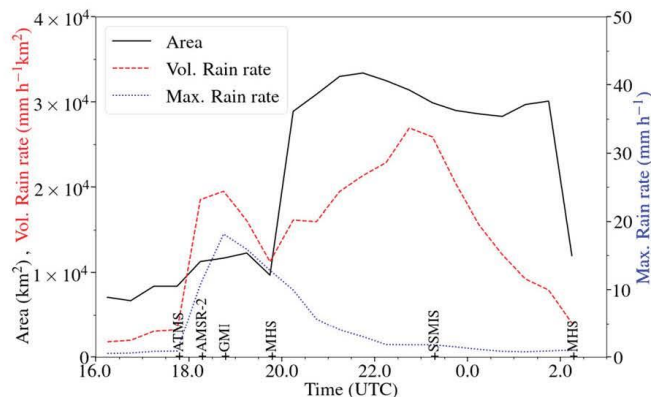


FIG. 7. Time series of the IMERG precipitation area, rain volume, and maximum rain rate of the MCS observed on the 10 June 2017 CPEX mission. PMW sensor names are annotated on the x axis at their respective half-hour overpass interval.

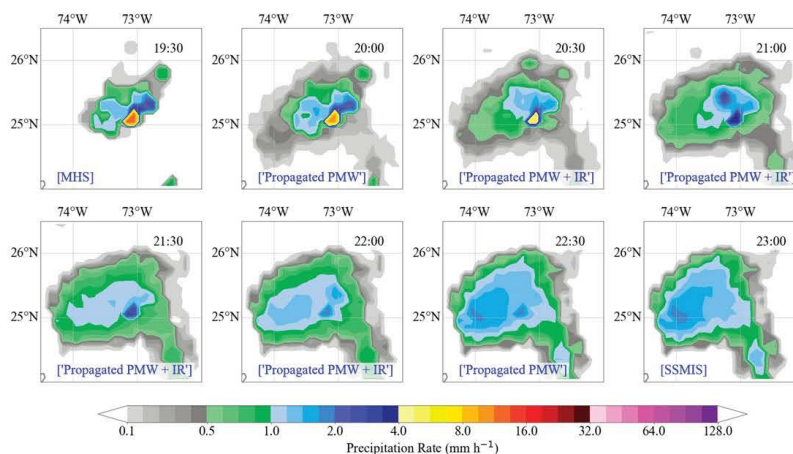


FIG. 8. IMERG precipitation from 1930 through 2300 UTC for the MCS observed on 10 June 2017. There were PMW overpasses during half-hours starting at 1930 and 2300 UTC. IMERG precipitation during intermediate intervals is estimated by the morphing algorithm using the Kalman weighted average of propagated PMW and IR precipitation.

The precipitation area for the CPEX case study on 6 June (Fig. 5) also shows a sudden growth during half-hours, starting at 1600 and 2100 UTC, immediately after PMW overpasses. If we chose a different MCS boundary by including or excluding small neighboring cells, it affects the metrics. However, the area would still grow unrealistically, as clearly noticeable at 1600 UTC in IMERG animation (provided as supplemental material). For both MCSs, if the precipitation areas were linearly interpolated between PMW overpasses, these sudden growths would not exist, and the MCS size would appear to grow more reasonably.

In both CPEX case studies, the unrealistic growth is not always present after a PMW observation. Similarly, the maximum precipitation rate for the 10 June case (Fig. 7) does not sag between PMW observations from 1800 to 2000 UTC. This contrasts with the CPEX case on 6 June 2017, where the maximum precipitation rate peaked during most PMW observations and sagged between overpass times (Fig. 5). Thus, these examples also suggest that the morphing issues uncovered are not uniformly present.

c. Precipitation rate distribution: PMW versus morphing

Given the apparent limitations in IMERG Version 06 revealed by this analysis of two MCSs from the CPEX field program, we explore the systematic biases in IMERG precipitation using bulk statistics. Specifically, we look at the precipitation rate distribution (as a probability density function) of PMW observations and morphing over a wider region from 30°N to 30°S and for an extended period of 19 years. Our initial analysis showed that TMI and GMI exhibit differences in their precipitation rate distribution, so the data are grouped into

TRMM (2001–13) and GPM (2015–19) periods. In the year 2014, PMW sensors are intercalibrated to TMI for dates before June 1st and to GMI for the rest of the year, so 2014 is excluded to avoid mixing the calibrations. The PDF differences between TMI and GMI are not analyzed further, since this is beyond the scope of this study.

The precipitation rate distributions from both the TRMM and GPM periods (Fig. 9) show that differences between PMW sensors are very small as expected, since they are intercalibrated to TMI or GMI histograms. However, differences between distributions for PMW and morphed precipitation stand out compared to differences between individual sensors. We can infer from Fig. 9 that the morphing estimates have a higher frequency of light precipitation rates and a lower frequency of heavy precipitation rates relative to PMW estimates. This conclusion is similar to the result from the CPEX mission on 10 June 2017, where the small MCS observed at 2030 UTC had spurious precipitation areas with light precipitation rates.

Another important conclusion from the CPEX case study on 6 June 2017 (Fig. 5) was that the MCS's maximum precipitation rate decreased further and further as the time interval from the PMW overpass increased. Figure 10 presents precipitation rate distributions for time intervals away from the PMW overpass (both past and future). The time interval "30 min away" represents time morphing estimates from the past PMW observations propagated forward to the next half-hour and future PMW observations propagated backward to the previous half-hour. Similar logic can be extended to other time intervals. The distributions show that the frequency of light precipitation increases slightly with increasing time intervals. In contrast, there is a prominent decrease in the frequency of heavy

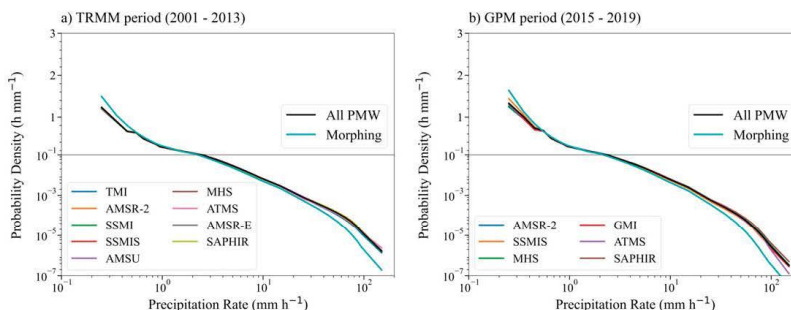


FIG. 9. The precipitation rate distribution of estimates from the GPROF algorithm (for various PMW sensors), and the morphing algorithm. The y axis is linear for the upper half, and it is logarithmic for the lower half to make differences more discernable at the tails of the distribution.

precipitation rates, as one moves further away from the PMW overpass times. This conclusion is consistent with the observed sag in the maximum precipitation rate away from PMW overpasses in the CPEX case study on 6 June 2017.

d. Precipitation occurrence: PMW versus morphing

Figure 11 displays histograms of PMW and morphing precipitation occurrence from 19 000 half-hour data for different minimum thresholds (0.1, 0.5, 1.0, and 2.0 mm h⁻¹). The spatial coverage of PMW sensors changes with time as they move over various regions on Earth. This introduces spatial variability and sampling variability in the tropical precipitation occurrence. Therefore, the spread in the histogram represents all three variabilities: temporal, spatial, and PMW coverage. The statistic “precipitation occurrence” also can be interpreted as the sum of frequencies of various precipitation rate bins in Fig. 9 expressed as a fraction of total grid cells in each category. This statistic is more intuitive and highlights the net effect of morphing on tropical precipitation occurrence.

For a minimum threshold of 0.1 mm h⁻¹, Fig. 11a shows that locations with PMW observations have a 6.56% median precipitation occurrence, whereas locations with estimates from morphing have an 8.86% median precipitation occurrence. This difference is considerable and implies that morphing creates 35% more precipitation for a same-sized region. Using a nonparametric significance test (permutation test; Wilks 2011), we found that the difference in median precipitation occurrence between PMW and morphing is statistically significant at a 99% confidence interval. This suggests that the difference in precipitation occurrence between PMW and morphing is substantially larger than the variabilities or spread in the histogram. The higher precipitation occurrence in morphing estimates implies that it produces spurious precipitation cells, consistent with the CPEX case study from 10 June 2017.

When the minimum threshold is increased to 0.5 mm h⁻¹, the absolute and relative difference in precipitation occurrence between PMW and morphing decreases sharply (Fig. 11b).

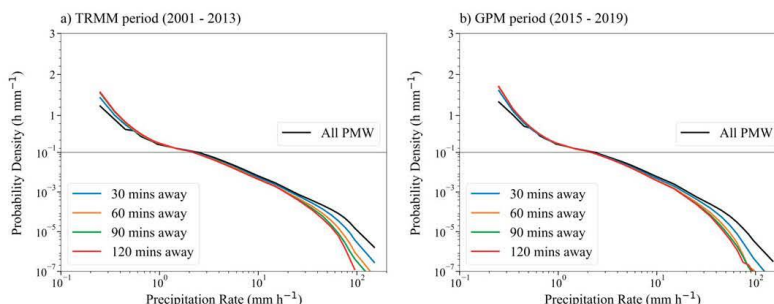


FIG. 10. The precipitation rate distribution for estimates from the morphing algorithm, as a function of time away from the PMW observation. The y axis is linear for the upper half, and it is logarithmic for the lower half to make differences more discernable at the tails of the distribution.

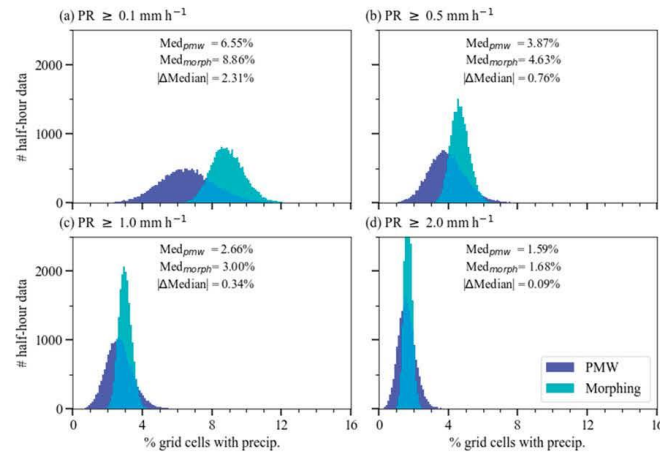


FIG. 11. Variability in tropical precipitation occurrence for PMW and morphing estimates, expressed as “% of grid cells with precipitation,” from 19 000 half-hour data randomly chosen from 2001 to 2019. Subplots show the change in precipitation occurrence for precipitation rate (PR) thresholds of (a) 0.1, (b) 0.5, (c) 1.0, and (d) 2.0 mm h^{-1} .

Results across the range of minimum thresholds (0.1, 0.5, 1.0, and 2.0 mm h^{-1}) show that light rain rates contribute to the significant difference in precipitation occurrence between PMW and morphing.

5. Discussion

The specific instances of spurious precipitation in the CPEX case can be traced back to the time morphing algorithm. In general, a precipitation system observed at two different times will often have different sizes and shapes of precipitation areas. At intermediate times, the morphing algorithm propagates these PMW observations in the forward and backward direction using motion vectors with “little change” in their shape and size. Even if the motion vectors place the centroid of a forward and backward propagated system on top of each other, the weighted averaging will create a larger area if the shapes are different. In addition, the increase in precipitation area may be exacerbated if the motion vectors have biases that offset the centroids of the forward and backward propagated systems.

The overlapping of different sizes and shapes from two observation times can explain the unrealistic growth sometimes observed in CPEX case studies. The precipitation area created from overlapping shapes is larger at intermediate times and suddenly changes to a smaller area at the closest PMW observation. This might show up as a sudden decay or growth in precipitation area immediately before or after PMW observations, as observed in the CPEX case studies.

Though overlaps produce larger areas at intermediate times, the propagated precipitation rates are reduced by their

Kalman weights that are roughly inversely proportional to propagation time (Joyce and Xie 2011). Some grid cells in the intersecting region of forward and backward propagated precipitation areas receive estimates from both. However, other cells receive estimates from only one. Though the morphing algorithm combines propagated precipitation with IR precipitation, the Kalman averaging will more likely produce light rain in grid cells with the contribution from only one input source. For example, say that the weights for forward propagated, backward propagated, and IR in a particular grid cell are 0.26, 0.34, and 0.40, respectively. If the grid cell’s only nonzero contribution is forward propagated precipitation of 2 mm h^{-1} , the Kalman averaging would estimate a value of 0.52 mm h^{-1} ($0.26 \times 2 + 0.34 \times 0 + 0.40 \times 0$).

Figure 8 shows the MCS from the CPEX case study on 10 June 2017, exhibiting different shapes and sizes during PMW observations at 1930 and 2300 UTC from an MHS and an SSMIS, respectively. At the intermediate times, the MCS takes a shape and size that is an overlap of these “PMW observations” propagated to the respective analysis time. At 2030 UTC, the west side of the MCS must be provided by the backward propagated precipitation because the IR image (Fig. 6b) shows no deep convection, and the forward propagated PMW observation from 1930 UTC has no rainfall over this region. The intensity of backward propagation of PMW precipitation fell from 2 to 0.5 mm h^{-1} on the west side of the MCS due to decreasing Kalman weights and lack of other sources. The aircraft photos and IR image in Fig. 6 show that the IMERG precipitation on the west side of the MCS is indeed spurious at 2030 UTC.

IMERG, with its high temporal resolution, is more suitable than the past gridded precipitation data to track MCSs

as precipitation objects and study their upscale growth. Understanding the IMERG biases presented in this article might help define MCSs and their upscale growth, more appropriately. This study shows that using rain volume to define the growth and decay of an MCS yields stable results, based on the CPEX case studies. In contrast, the use of precipitation area to define the MCS life cycle is sometimes contaminated by spurious precipitation. This can be remedied to some extent by using a low-end cutoff precipitation threshold. Figures 9 and 11 suggest that a precipitation map thresholded at or above 0.5 mm h^{-1} has minimal spurious rain areas. However, one should use the cutoff cautiously because it merely sets the low end of the PDF to zero, but it cannot recover the underestimation at the high end. Taken together, a cutoff will cause the overall mean and rain volume of the morphed estimates to be underestimated. The problem is more fundamental and affects the entire PDF.

This line of reasoning was developed in conversations with the IMERG team, leading them to develop a new algorithm called Scheme for Histogram Adjustment with Ranked Precipitation Estimates Neighborhood (SHARPEN) that resolves some of the biases reported here. This algorithm restores the precipitation rate distribution of morphing estimates to a distribution similar to the PMW estimates using a quantile mapping based approach. SHARPEN will most likely be implemented in the upcoming release of IMERG Version 07, and is described in the companion paper (Tan et al. 2021). Preliminary testing (not shown) demonstrated that SHARPEN reduced the spurious precipitation considerably for the 10 June CPEX case study.

6. Conclusions

In this study, an object-oriented approach is used to compare MCS properties, such as precipitation area, rain volume, and maximum precipitation rate during and between PMW observations. Two case studies are used to investigate and illustrate potential issues with the time morphing in IMERG before these issues are confirmed to be prevalent throughout IMERG using bulk statistics.

In the case studies, IMERG precipitation is evaluated against DC-8 aircraft observations from the NASA CPEX field program. The aircraft photos, pilot radar, and IR image indicate that at times of PMW observations, IMERG precipitation area is similar to aircraft observations. However, in the absence of PMW observations, IMERG appeared to have spurious precipitation areas. For the small MCS of 10 June 2017, the precipitation area grew unrealistically in the next 30 min after the PMW observation at 1930 UTC. We found that this sudden growth and the spurious precipitation originates from the morphing algorithm. Another finding was that for the intense, large MCS of 6 June 2017, the maximum precipitation rate peaked at most PMW overpass times, but sagged between those observation times. Although these are limited case studies, the evidence from CPEX guided us to investigate systematic biases in the IMERG's time morphing algorithm. The analysis of precipitation rate distribution and precipitation occurrence shows that there are systematic differences between precipitation estimates from PMW observations and time morphing. When PMW observations are absent, IMERG has a higher

frequency of light precipitation and a lower occurrence of heavy precipitation rates. The high occurrence of light precipitation rates may sometimes produce large precipitation areas.

In our work, we highlight biases in time morphed precipitation estimates compared to PMW precipitation. However, PMW precipitation estimates from GPROF have their own biases as highlighted in past studies. An ideal validation would be to compare morphing precipitation estimates with surface observations. Nevertheless, in the absence of global surface observations, comparing IMERG precipitation estimates for PMW observation and time morphing is still valuable to bring out their algorithmic differences. Identifying these morphing biases helped the IMERG team improve the next version of IMERG by bringing the morphing estimates more into line with the PMW (and PMW-calibrated IR) estimates. The end users of IMERG Version 06 should be cautious about the higher occurrence of light precipitation and lower precipitation intensity in the absence of PMW observations.

Acknowledgments. We appreciate the skill and dedication of the pilots, flight crews, instrument teams, and NASA supporting staff that made the CPEX field program successful. We are grateful for discussions on statistical techniques with Prof. Courtney Strong and Prof. Gannet Hallar at the Department of Atmospheric Sciences, University of Utah. We also thank the three anonymous reviewers whose comments and suggestions helped refine this manuscript. We appreciate the computing and storage support from the Center for High-Performance Computing (CHPC) at the University of Utah. This research was supported by NASA Grant NNX17AG74G (Univ. of Utah) and the GPM mission (G. Huffman) under the leadership of Ramesh Kakar and Gail Jackson.

Data availability statement. The aircraft track from the NASA's CPEX field program flights is accessible at <https://tcis.jpl.nasa.gov/data/cpeX/track/>. The aircraft's forward camera and pilots' radar videos from the CPEX program are available at <https://asp-archive.arc.nasa.gov/CPEX/Video/>. IMERG is a NASA's global satellite precipitation product available at different time resolution and latencies. IMERG Version 06 (Final Run) used in this study can be downloaded from the https://disc.gsfc.nasa.gov/datasets/GPM_3IMERGHH_06/summary?keywords=%22IMERG%20final%22. The web interface allows a user to choose the appropriate period (2001–19) and the domain (30°N–30°S).

REFERENCES

- Adler, R. F., and Coauthors, 2018: The Global Precipitation Climatology Project (GPCP) monthly analysis (new version 2.3) and a review of 2017 global precipitation. *Atmosphere*, **9**, 138, <https://doi.org/10.3390/atmos9040138>.
- Akaeda, K., J. Reisner, and D. Parsons, 1995: The role of mesoscale and topographically induced circulations in initiating a flash flood observed during the TAMEX project. *Mon. Wea. Rev.*, **123**, 1720–1739, [https://doi.org/10.1175/1520-0493\(1995\)123<1720:TROMAT>2.0.CO;2](https://doi.org/10.1175/1520-0493(1995)123<1720:TROMAT>2.0.CO;2).
- Asong, Z. E., S. Razavi, H. S. Wheeler, and J. S. Wong, 2017: Evaluation of Integrated Multisatellite Retrievals for GPM

- (IMERG) over Southern Canada against ground precipitation observations: A preliminary assessment. *J. Hydrometeorol.*, **18**, 1033–1050, <https://doi.org/10.1175/JHM-D-16-0187.1>.
- Bodenreider, C., L. Wright, O. Barr, K. Xu, and S. Wilson, 2019: Assessment of social, economic, and geographic vulnerability pre- and post-Hurricane Harvey in Houston, Texas. *Environ. Justice*, **12**, 182–193, <https://doi.org/10.1089/env.2019.0001>.
- Bytheway, J. L., M. Hughes, K. Mahoney, and R. Cifelli, 2020: On the uncertainty of high-resolution hourly quantitative precipitation estimates in California. *J. Hydrometeorol.*, **21**, 865–879, <https://doi.org/10.1175/JHM-D-19-0160.1>.
- Cui, W., X. Dong, B. Xi, Z. Feng, and J. Fan, 2020: Can the GPM IMERG final product accurately represent MCSs' precipitation characteristics over the central and eastern United States? *J. Hydrometeorol.*, **21**, 39–57, <https://doi.org/10.1175/JHM-D-19-0123.1>.
- Davis, C., B. Brown, and R. Bullock, 2006: Object-based verification of precipitation forecasts. Part I: Methodology and application to mesoscale rain areas. *Mon. Wea. Rev.*, **134**, 1772–1784, <https://doi.org/10.1175/MWR3145.1>.
- Gaona, M. F. R., A. Overeem, H. Leijnse, and R. Uijlenhoet, 2016: First-year evaluation of GPM rainfall over the Netherlands: IMERG day 1 final run (V03D). *J. Hydrometeorol.*, **17**, 2799–2814, <https://doi.org/10.1175/JHM-D-16-0087.1>.
- Gelaro, R., and Coauthors, 2017: The Modern-Era Retrospective Analysis for Research and Applications, version 2 (MERRA-2). *J. Climate*, **30**, 5419–5454, <https://doi.org/10.1175/JCLI-D-16-0758.1>.
- Gowan, T. A., and J. D. Horel, 2020: Evaluation of IMERG-E precipitation estimates for fire weather applications in Alaska. *Wea. Forecasting*, **35**, 1831–1843, <https://doi.org/10.1175/WAF-D-20-0023.1>.
- Gu, G., R. F. Adler, G. J. Huffman, and S. Curtis, 2007: Tropical rainfall variability on interannual-to-interdecadal and longer time scales derived from the GPCP monthly product. *J. Climate*, **20**, 4033–4046, <https://doi.org/10.1175/JCLI4227.1>.
- Hayden, L., and C. Liu, 2018: A multiyear analysis of global precipitation combining CloudSat and GPM precipitation retrievals. *J. Hydrometeorol.*, **19**, 1935–1952, <https://doi.org/10.1175/JHM-D-18-0053.1>.
- Hong, Y., K. Hsu, S. Sorooshian, and X. Gao, 2004: Precipitation Estimation from Remotely Sensed Imagery Using an Artificial Neural Network Cloud Classification System. *J. Appl. Meteorol.*, **43**, 1834–1853, <https://doi.org/10.1175/JAM2173.1>.
- Hou, A. Y., and Coauthors, 2014: The Global Precipitation Measurement mission. *Bull. Amer. Meteor. Soc.*, **95**, 701–722, <https://doi.org/10.1175/BAMS-D-13-00164.1>.
- Huffman, G. J., and Coauthors, 1997: The Global Precipitation Climatology Project (GPCP) combined precipitation dataset. *Bull. Amer. Meteor. Soc.*, **78**, 5–20, [https://doi.org/10.1175/1520-0477\(1997\)078<0005:TGPCPG>2.0.CO;2](https://doi.org/10.1175/1520-0477(1997)078<0005:TGPCPG>2.0.CO;2).
- , and Coauthors, 2007: The TRMM Multisatellite Precipitation Analysis (TMPA): Quasi-global, multiyear, combined-sensor precipitation estimates at fine scales. *J. Hydrometeorol.*, **8**, 38–55, <https://doi.org/10.1175/JHM560.1>.
- , and Coauthors, 2020a: NASA Global Precipitation Measurement (GPM) Integrated Multi-satellite Retrievals for GPM (IMERG). Algorithm Theoretical Basis Doc., version 06, 35 pp., https://gpm.nasa.gov/sites/default/files/2020-05/IMERG_ATBD_V06.3.pdf.
- , D. T. Bolvin, E. J. Nelkin, and J. Tan, 2020b: Integrated Multi-Satellite Retrievals for GPM (IMERG) technical documentation. NASA Tech. Doc., 83 pp., <https://gpm.nasa.gov/resources/documents/IMERG-V06-Technical-Documentation>.
- Janowiak, J. E., R. J. Joyce, and Y. Yarosh, 2001: A real-time global half-hourly pixel-resolution infrared dataset and its applications. *Bull. Amer. Meteor. Soc.*, **82**, 205–217, [https://doi.org/10.1175/1520-0477\(2001\)082<0205:ARTGHH>2.3.CO;2](https://doi.org/10.1175/1520-0477(2001)082<0205:ARTGHH>2.3.CO;2).
- Johnson, A., X. Wang, F. Kong, and M. Xue, 2013: Object-based evaluation of the impact of horizontal grid spacing on convection-allowing forecasts. *Mon. Wea. Rev.*, **141**, 3413–3425, <https://doi.org/10.1175/MWR-D-13-00027.1>.
- Joyce, R. J., and P. Xie, 2011: Kalman filter-based CMORPH. *J. Hydrometeorol.*, **12**, 1547–1563, <https://doi.org/10.1175/JHM-D-11-022.1>.
- , J. E. Janowiak, P. A. Arkin, and P. Xie, 2004: CMORPH: A method that produces global precipitation estimates from passive microwave and infrared data at high spatial and temporal resolution. *J. Hydrometeorol.*, **5**, 487–503, [https://doi.org/10.1175/1525-7541\(2004\)005<0487:CAMTPG>2.0.CO;2](https://doi.org/10.1175/1525-7541(2004)005<0487:CAMTPG>2.0.CO;2).
- Kidd, C., 2018: NASA Global Precipitation Measurement (GPM) Precipitation Retrieval and Profiling Scheme (PRPS). Algorithm Theoretical Basis Doc., version 01-02, 16 pp., https://pps.gsfc.nasa.gov/Documents/20180203_SAPHIR-ATBD.pdf.
- , J. Tan, P.-E. Kirstetter, and W. A. Petersen, 2018: Validation of the version 05 Level 2 precipitation products from the GPM Core Observatory and constellation satellite sensors. *Quart. J. Roy. Meteor. Soc.*, **144**, 313–328, <https://doi.org/10.1002/qj.3175>.
- Kummerow, C., W. Barnes, T. Kozu, J. Shiue, and J. Simpson, 1998: The Tropical Rainfall Measuring Mission (TRMM) sensor package. *J. Atmos. Oceanic Technol.*, **15**, 809–817, [https://doi.org/10.1175/1520-0426\(1998\)015<0809:TTRMMT>2.0.CO;2](https://doi.org/10.1175/1520-0426(1998)015<0809:TTRMMT>2.0.CO;2).
- , D. L. Randel, M. Kulie, N. Wang, R. Ferraro, S. Joseph Munchak, and V. Petkovic, 2015: The evolution of the Goddard profiling algorithm to a fully parametric scheme. *J. Atmos. Oceanic Technol.*, **32**, 2265–2280, <https://doi.org/10.1175/JTECH-D-15-0039.1>.
- Lamb, D., and J. Verlinde, 2011: *The Physics and Chemistry of Clouds*. Cambridge University Press, 70 pp.
- Liu, C., 2011: Rainfall contributions from precipitation systems with different sizes, convective intensities, and durations over the tropics and subtropics. *J. Hydrometeorol.*, **12**, 394–412, <https://doi.org/10.1175/2010JHM1320.1>.
- Maranan, M., A. H. Fink, P. Knippertz, L. K. Amekudzi, W. A. Atuah, and M. Stengel, 2020: A process-based validation of GPM IMERG and its sources using a mesoscale rain gauge network in the West African Forest Zone. *J. Hydrometeorol.*, **21**, 729–749, <https://doi.org/10.1175/JHM-D-19-0257.1>.
- McCollum, D. M., R. A. Maddox, and K. W. Howard, 1995: Case study of a severe mesoscale convective system in central Arizona. *Wea. Forecasting*, **10**, 643–665, [https://doi.org/10.1175/1520-0434\(1995\)010<0643:CSOASM>2.0.CO;2](https://doi.org/10.1175/1520-0434(1995)010<0643:CSOASM>2.0.CO;2).
- Mohr, K. I., J. S. Famiglietti, and E. J. Zipser, 1999: The contribution to tropical rainfall with respect to convective system type, size, and intensity estimated from the 85-GHz ice-scattering signature. *J. Appl. Meteorol.*, **38**, 596–606, [https://doi.org/10.1175/1520-0450\(1999\)038<0596:TCTTRW>2.0.CO;2](https://doi.org/10.1175/1520-0450(1999)038<0596:TCTTRW>2.0.CO;2).
- Nesbitt, S. W., R. Cifelli, and S. A. Rutledge, 2006: Storm morphology and rainfall characteristics of TRMM precipitation features. *Mon. Wea. Rev.*, **134**, 2702–2721, <https://doi.org/10.1175/MWR3200.1>.
- Nguyen, P., M. Ombadi, S. Sorooshian, K. Hsu, A. AghaKouchak, D. Braithwaite, H. Ashouri, and A. R. Thorstensen, 2018: The PERSIANN family of global satellite precipitation data: A review and evaluation of products. *Hydrol. Earth Syst. Sci.*, **22**, 5801–5816, <https://doi.org/10.5194/hess-22-5801-2018>.

- Olson, W. S., H. Masunaga, and the GPM Combined Radar-Radiometer Algorithm Team, 2011: GPM combined radar-radiometer precipitation. Algorithm theoretical basis document (version 2). PPS, NASA/GSFC, 58 pp., <http://pps.gsfc.nasa.gov/Documents/GPM2011CombinedL2ATBD.pdf>.
- Paul, S., D. Ghebreyesus, and H. O. Sharif, 2019: Brief communication: Analysis of the fatalities and socio-economic impacts caused by Hurricane Florence. *Geosciences*, **9**, 58, <https://doi.org/10.3390/geosciences9020058>.
- Randel, D. L., C. D. Kummerow, and S. Ringerud, 2020: The Goddard Profiling (GPROF) precipitation retrieval algorithm. *Satellite Precipitation Measurement*, V. Levizzani et al., Eds., Advances in Global Change Research, Vol 67, Springer, 141–152, https://link.springer.com/chapter/10.1007/978-3-030-24568-9_8.
- Schneider, U., and Coauthors, 2014: GPCP's new land surface precipitation climatology based on quality-controlled in situ data and its role in quantifying the global water cycle. *Theor. Appl. Climatol.*, **115**, 15–40, <https://doi.org/10.1007/s00704-013-0860-x>.
- Sharifi, E., R. Steinacker, and B. Saghaian, 2016: Assessment of GPM-IMERG and other precipitation products against gauge data under different topographic and climatic conditions in Iran: Preliminary results. *Remote Sens.*, **8**, 135, <https://doi.org/10.3390/rs8020135>.
- Sohoulande, C. D., K. Stone, A. Szogi, and P. Bauer, 2019: An investigation of seasonal precipitation patterns for rainfed agriculture in the southeastern region of the United States. *Agric. Water Manage.*, **223**, 105728, <https://doi.org/10.1016/j.agwat.2019.105728>.
- Steinker, S., K. Hoberg, and U. W. Thonemann, 2017: The value of weather information for e-commerce operations. *Prod. Oper. Manag.*, **26**, 1854–1874, <https://doi.org/10.1111/poms.12721>.
- Sungmin, O., U. Foelsche, G. Kirchengast, J. Fuchsberger, J. Tan, and W. A. Petersen, 2017: Evaluation of GPM IMERG Early, Late, and Final rainfall estimates using WegenerNet gauge data in southeastern Austria. *Hydrol. Earth Syst. Sci.*, **21**, 6559–6572, <https://doi.org/10.5194/hess-21-6559-2017>.
- Tan, J., W. A. Petersen, and A. Tokay, 2016: A novel approach to identify sources of errors in IMERG for GPM ground validation. *J. Hydrometeorol.*, **17**, 2477–2491, <https://doi.org/10.1175/JHM-D-16-0079.1>.
- , —, P. Kirstetter, and Y. Tian, 2017: Performance of IMERG as a function of spatiotemporal scale. *J. Hydrometeorol.*, **18**, 307–319, <https://doi.org/10.1175/JHM-D-16-0174.1>.
- , —, G. Kirchengast, D. C. Goodrich, and D. B. Wolff, 2018: Evaluation of global precipitation measurement rainfall estimates against three dense gauge networks. *J. Hydrometeorol.*, **19**, 517–532, <https://doi.org/10.1175/JHM-D-17-0174.1>.
- , G. J. Huffman, D. T. Bolvin, and E. J. Nelkin, 2019: IMERG V06: Changes to the morphing algorithm. *J. Hydrometeorol.*, **36**, 2471–2482, <https://doi.org/10.1175/JTECH-D-19-0114.1>.
- , —, —, —, and M. Rajagopal, 2021: SHARPEN: A scheme to restore the distribution of averaged precipitation fields. *J. Hydrometeorol.*, **22**, 2105–2116, <https://doi.org/10.1175/JHM-D-20-0225.1>.
- Tapiador, F. J., A. Navarro, E. García-Ortega, A. Merino, J. L. Sánchez, C. Marcos, and C. Kummerow, 2020: The contribution of rain gauges in the calibration of the IMERG product: Results from the first validation over Spain. *J. Hydrometeorol.*, **21**, 161–182, <https://doi.org/10.1175/JHM-D-19-0116.1>.
- Verstraete, G., E. H. Aghezzaf, and B. Desmet, 2019: A data-driven framework for predicting weather impact on high-volume low-margin retail products. *J. Retailing Consum. Serv.*, **48**, 169–177, <https://doi.org/10.1016/j.jretconser.2019.02.019>.
- Watters, D., A. Battaglia, K. Mroz, and F. Tridon, 2018: Validation of the GPM version-5 surface rainfall products over Great Britain and Ireland. *J. Hydrometeorol.*, **19**, 1617–1636, <https://doi.org/10.1175/JHM-D-18-0051.1>.
- Wilks, D. S., 2011: *Statistical Methods in the Atmospheric Sciences*. 3rd ed. Elsevier, 169 pp.
- Xie, P., R. Joyce, S. Wu, S. Yoo, Y. Yarosh, F. Sun, and R. Lin, 2017: Reprocessed, bias-corrected CMORPH global high-resolution precipitation estimates from 1998. *J. Hydrometeorol.*, **18**, 1617–1641, <https://doi.org/10.1175/JHM-D-16-0168.1>.
- You, Y., V. Petkovic, J. Tan, R. Kroodsma, W. Berg, C. Kidd, and C. Peters-Lidard, 2020: Evaluation of V05 precipitation estimates from GPM constellation radiometers using KuPR as the reference. *J. Hydrometeorol.*, **21**, 705–728, <https://doi.org/10.1175/JHM-D-19-0144.1>.
- Zhang, Q., P. Sun, V. P. Singh, and X. Chen, 2012: Spatial-temporal precipitation changes (1956–2000) and their implications for agriculture in China. *Global Planet. Change*, **82–83**, 86–95, <https://doi.org/10.1016/j.gloplacha.2011.12.001>.
- Zhou, Y., W. K. M. Lau, and G. J. Huffman, 2015: Mapping TRMM TMPA into average recurrence interval for monitoring extreme precipitation events. *J. Appl. Meteor. Climatol.*, **54**, 979–995, <https://doi.org/10.1175/JAMC-D-14-0269.1>.

CHAPTER 3

TRACKING MESOSCALE CONVECTIVE SYSTEMS AND SPATIAL VARIABILITY OF THEIR PROPERTIES IN THE TROPICS USING IMERG

3.1 Abstract

Mesoscale Convective Systems (MCSs) constitute only a small fraction of convective systems in the tropics but have a greater impact on tropical weather and global climate. Since surface observations are scarce over the tropics, past studies used satellite Infrared (IR) data to track and study MCSs' Lagrangian properties. These studies are regional and for a shorter period. The recent availability of Integrated Multi-satellite Retrieval for Global Precipitation Mission (IMERG) with rainfall data every 30 minutes and access to faster computers have enabled us to track MCSs over global tropics for a longer period. Using the Forward in Time (FiT) program to track MCSs for ten years, we present a long-term statistics of MCS properties and consistent regional comparison since the same tracking method is used.

Though IMERG is advantageous, it poses challenges due to connected MCSs and resolution differences between contributing Passive Microwave (PMW) sensors in IMERG. We smoothed and normalized the precipitation field to overcome this problem; then applied FiT's cascading thresholds to identify mesoscale objects and track them. Our results show that MCSs' contribute ~70% of IMERG annual precipitation, though they

are only ~7% of all tracked systems. Besides many regional differences observed in MCS properties, the land-ocean dichotomy is prominent. The large and long-lived MCSs occur more often over the ocean than on land except in the Amazon basin. Moreover, the heavy rain rates occur more frequently over the ocean, possibly because the heavy rain cores over land are narrower than the PMW sensor resolution.

3.2 Introduction

Mesoscale convective systems (MCSs) play a crucial role in tropical climate and weather. They constitute a small fraction of moist convection but contribute 50 - 90% of annual tropical precipitation (Feng et al., 2021; Nesbitt et al., 2006; Mathon and Laurent, 2001; Liu, 2011). As the largest contributor to tropical precipitation, an indirect measure of net latent heat, MCSs are the actual hot towers that drive global atmospheric circulation (Zipser, 2003; Riehl and Malkus, 1958;). An MCS produces a top-heavy latent heating profile compared to cumulonimbus and congestus clouds with a bottom-heavy heating profile (Schumacher et al., 2004; Houze, 1989). Such top-heavy heating affects the weather through atmospheric waves (Matthews & Kiladis, 2000; Murakami, 1972) and global circulation through elevated circulation centers with stronger upper-level winds (Hartmann et al., 1984; Houze, 1989; Schumacher et al., 2004). MCSs also have large cloud shields that affect the earth's radiation budget by reflecting shortwave and absorbing longwave radiation. The radiative effects of MCSs are significant, but even more important is their rain contribution. In addition to being major rain producers, MCSs can produce lightning, floods, and landslides that lead to loss of life and property

(Maranan et al., 2019; Poveda et al., 2020). Therefore, it is critical to learn about MCS properties and their regional variability.

Surface radars help study MCS structure and their properties, but they are scarce over the tropics; therefore, satellite data are valuable. Early studies used Infrared (IR) brightness temperature (T_b) or space-borne precipitation radar (PR) data to characterize MCSs over various tropical regions. Though IR-based studies helped understand the broader aspects of MCSs distribution and their properties, they have biases or limitations in determining an MCS's rain rates, area, lifetime, and propagation velocity. The IR T_b -based rain retrieval algorithms underestimate the rain rates for shallower convection with a dominant warm rain process and overestimate rain rates over stratiform regions with colder cloud shields (Liu et al., 2007; Berg et al., 2002; Woodley et al., 1980). Many past studies defined the MCS area by IR T_b thresholds that were assumed to represent surface precipitation (Futyan and Del Genio, 2007; Laurent et al., 2002a; Mathon and Laurent, 2001; Machado et al., 1998; Evans and Shemo, 1996; Mapes and Houze, 1992;). Using coincident IR and PR data, Liu et al. (2007) found that only 35% (54%) of pixels with IR $T_b < 235$ K (210 K) had surface precipitation detected by the PR. Hence, the IR-based MCS identification may not represent the intended MCS precipitation area. A bias in MCS's lifetime often occurs when these IR cloud shields continue to exist long after precipitation ceases due to the radiative heating at the cloud base and cooling at the top (Houze, 1982).

Other widely used data to characterize tropical MCSs are the space-borne precipitation radar on board Tropical Rainfall Measuring Mission (TRMM) and Global Precipitation Mission (GPM) core satellites. Houze et al. (2015), Liu et al. (2008), and other studies

used PR data to study convective regimes over different tropical regions. The PR data has a finer spatial resolution of 5 km and is closer to surface precipitation observations than IR. However, PR has a narrower swath that limits the MCS size identified in the PR reflectivity or precipitation field. Nesbitt et al. (2006) reported that nearly 9% of precipitation features touched the swath edges, but they contributed ~42% of total precipitation. These edge features may extend outside the swath and are probably larger. The PR also has a poor temporal resolution and provides only snapshots of MCSs; hence, these features cannot be tracked to obtain Lagrangian properties such as lifetime and propagation velocity.

The Integrated Multi-satellite Retrieval for Global Precipitation Measurement Mission (IMERG; Huffman et al. 2020a, 2020b) is NASA's most recent global precipitation data available every 30 minutes at a spatial resolution of 0.1° . IMERG mainly uses passive microwave (PMW) precipitation retrievals as high-quality observations and, in their absence, combines advected PMW precipitation with IR rain retrievals based on IR T_b gradients rather than direct IR T_b . IMERG precipitation values are less affected by the non-precipitating anvils than IR since the PMW rain retrievals depend on total column ice and/or liquid water content. In addition, when compared to space-borne PR data, the IMERG precipitation field is not limited by satellite swath. IMERG also has a finer temporal resolution than PR, making it more suitable for tracking MCSs.

Defining and identifying the MCSs as individual spatio-temporal objects that move and evolve during their lifespan is beneficial for numerical model validation and learning the MCS regional variability. The object-based verification method (one of the five spatial verification methods listed in Dorninger et al., 2018) avoids "double penalty" and other

problems that face the traditional contingency table-based verification method (Brown et al., 2012)(Dorninger et al., 2018). The object-based method also provides practical ways to improve the numerical model's convective parameterization in terms of frequency, size, lifetime, rain volume, and propagation velocity (Davis et al., 2006). Past object-based studies that use IR data were over a small region and for a short period. The availability of long-term global precipitation data and fast-computing power motivated us to track MCSs over the global tropics (30° N to 30° S) for ten years (2011 - 2020). We use the Forward in Time (FiT; Skok et al., 2013; 2009) algorithm to track MCSs and present the long-term statistics with a more consistent regional comparison since the same tracking method is used.

Although IMERG is advantageous over IR, the tracking is challenging due to connected MCSs forming transient precipitation bands (Virts & Houze, 2015; Mapes and Houze, 1992;), and differences in PMW sensor resolutions (You et al., 2020). The FiT is a generic tracking algorithm that can identify and track objects in a sequence of two- or three-dimensional fields. Therefore, one of our goals in this work is to find the optimal FiT parameters to track MCSs in IMERG. The other goal is to study the regional variability of MCS properties such as rain contribution, frequency, area, maximum rain rate, lifetime, and propagation velocity. The regional environment affects the MCS properties, including the strong diurnal cycle over land and the associated mesoscale circulations. This article broadly compares the MCS properties over land vs. ocean and onshore vs. offshore regions. Nevertheless, some land regions also have atmospheric processes unique to their locations, like the dominating diurnal cycle over the maritime continent, easterly jet over west Africa, and moist boundary layer over the Amazon basin.

We make the regional comparison of MCS properties through their occurrence frequency and percentile values which complement recent IMERG-based studies that use different tracking algorithms (Feng et al., 2021a; Hayden et al., 2021).

The rest of the article is organized as follows: Section 2 discusses the IMERG precipitation product, the FiT tracking algorithm, the challenges of tracking precipitation systems in IMERG, and the optimal tracking parameters for IMERG. Regional variability of MCS properties, including broad categories such as land vs. ocean, and onshore vs. offshore, are presented in section 3. We summarize important findings and future work in section 4.

3.3 Data and Methods

3.3.1 IMERG version 06B

IMERG is a global precipitation product available at a higher temporal resolution (30 minutes) and a finer spatial resolution (0.1°) than its predecessor, TRMM Multisatellite precipitation analysis (TMPA; Huffman et al. 2007). IMERG has three runs: Early, Late, and Final, available at various latencies targeted for different applications. This paper uses the IMERG Final run, a research quality product that includes more passive microwave (PMW) satellite observations and rain gauge bias correction compared to other runs. IMERG combines the precipitation retrievals from PMW sensors onboard the virtual constellation of low earth orbit (LEO) satellites and retrievals from Infrared (IR) sensors onboard geostationary satellites. PMW-derived precipitation is considered as higher quality compared to IR-based precipitation. Therefore, at locations with PMW

overpasses, IMERG uses PMW precipitation retrievals. However, over other locations, IMERG uses a Kalman Filter based time morphing algorithm to compute the weighted sum of IR precipitation, backward advected PMW precipitation from future observations, and forward advected PMW precipitation from past observations. IR precipitation retrievals are based on IR T_b gradients rather than direct values. IMERG precipitation is less affected by non-precipitating anvils since it mainly uses PMW precipitation retrievals that are dependent on total column liquid water content and ice water content. Rajagopal et al. (2021) reported that at locations without PMW observations, IMERG version 06B sometimes had spurious precipitation, mostly $< 1 \text{ mm hr}^{-1}$, or underestimated heavy precipitation rates. SHARPEN, a new algorithmic component of IMERG, will significantly decrease these issues in IMERG version 07 (Tan et al., 2020). In subsection 2f, we discuss applying a threshold of 1 mm h^{-1} to mitigate the spurious precipitation. The PMW sensors on board the LEO satellites observe at multiple frequencies of different spatial resolutions. IMERG uses the Goddard Profiling algorithm (GPROF2017; Kummerow et al. 2015) and Precipitation Retrieval and Profiling scheme (PRPS; Kidd et al. 2018) to convert the PMW brightness temperature (T_b) at multiple frequencies into a precipitation estimate of nominal resolution. You et al. (2020) lists the nominal resolution for various PMW sensors. It ranges from 10 km for Sounder for Probing Vertical Profiles of Humidity (SAPHIR) to 55 km for Special Sensor Microwave Imager/Sounder (SSMIS). IMERG maps the PMW precipitation from nominal resolution to $0.1^\circ \times 0.1^\circ$ global grid using the nearest-neighbor interpolation. The PMW precipitation of constellation satellites is then intercalibrated to TRMM microwave imager (TMI) or GPM microwave imager (GMI) precipitation through histogram matching.

The IMERG final run has global rainfall data for approximately 20 years, from June 2000 to the near present, with a latency of ~ 3.5 months. Many PMW sensor satellites are added or decommissioned from the virtual constellation during this period. Therefore, merging the various PMW sensor retrievals to produce a global precipitation product presents some challenges to tracking the precipitation systems (discussed in section 3c). However, the higher spatial and temporal resolution with the continuous availability of rainfall data over two decades makes IMERG more suitable for tracking and studying MCSs globally.

3.3.2 Tracking algorithm

We use the FiT algorithm (Skok et al., 2013; 2009) to identify and track precipitation systems in IMERG. FiT is a generic tracking algorithm capable of tracking objects in a sequence of two- or three-dimensional variable fields. The algorithm tries to mimic object identification performed by a human analyst via subjective analysis. Earlier versions of the FiT algorithm was used to track precipitation systems in the TMPA 3B42 precipitation product, a predecessor to IMERG (White et al., 2017; Skok et al., 2013, 2010, 2009). The current version of the FiT program has two additional modifications described in subsection 2c. The FiT algorithm software package can be obtained at no cost from author Dr. Gregor Skok (gregor.skok@fmf.uni-lj.si).

FiT and other tracking methods involve two major steps: (i) identifying objects in each time step and (ii) relating objects across multiple time steps as the same time-evolving precipitation system. In conventional tracking methods, objects are identified as the contiguous area below or above a single threshold; for instance, $IR T_b < 235$ K has been widely used to represent regions with deep convection (Laurent et al., 2002; Mathon and

Laurent, 2001; Chen et al., 1996; Mapes and Houze, 1992). In contrast, FiT uses a technique called "cascading thresholds", which uses multiple thresholds to identify objects. This object identification method is similar to the Detect And Spread (DAS) technique used in many recent tracking algorithms(Feng et al., 2021; Fiolleau and Roca, 2013; Boer and Ramanathan, 1997). A DAS technique typically has two thresholds – the higher threshold detects the inner convective core, which spreads to the surrounding region defined by a lower threshold.

With the FiT, more than two thresholds can be used. For example, let's assume we use four thresholds (1, 3, 9, 27) mm h⁻¹, which may be interpreted as heavy, moderate, low, and light precipitation. First, the highest threshold (27 mm h⁻¹) is used to identify the extent of the core objects. Next, the core objects grow iteratively by one pixel in all directions into the surrounding region of moderate rainfall (9 – 27 mm h⁻¹). Once all the nearby pixels in this precipitation interval are claimed, the growth stops. Then, a check is made if some non-claimed regions with moderate rainfall still exist somewhere. These represent distinct areas of moderate rainfall that are not spatially linked to any region of heavy rainfall and are defined as additional core objects. The procedure (growth of existing objects and identification of additional core objects) is then repeated for all lower thresholds. Skok et al. (2013) discuss the complete workings of cascading thresholds, including other scenarios.

The next step in the FiT algorithm is to relate objects in multiple timesteps to define precipitation systems. FiT uses the areal overlap method to relate objects in consecutive time steps. This method has been widely used in other studies (Feng et al., 2021; Ocasio et al., 2020; Mathon and Laurent, 2001; Evans and Shemo, 1996; Williams and Houze,

1987). We use the term "system" to refer to a set of spatial objects in multiple time steps that are related to one another and can be considered part of the same time-evolving precipitation system. Tracking a precipitation system is complicated when a system splits into many pieces or merges with another system. Some algorithms terminate a system's tracking when a split or merger occurs and treat the resulting objects as a new system (Moseley et al., 2013; Fiolleau and Roca, 2013). However, the FiT algorithm continues to track a system after a split or merger, providing more accurate evolution and lifecycle information.

During a merger, multiple systems tracked through previous timesteps might overlap with an object in the next timestep. In this case, FiT allows the system with the biggest overlap with the object to persist. The other overlapping systems are either terminated or allowed to continue if there are other objects they overlap in the next timestep. During a split, a system will overlap with more than one object in the following time step. If this happens, the algorithm allows the system to continue as multiple pieces, and they are all considered part of the same system. In short, the FiT algorithm allows a system to have multiple pieces after the split but does not retroactively treat the pieces (systems) that merge as one precipitation system in previous timesteps. Hence, the name "Forward in Time".

3.3.3 Recent improvements to the FiT

The newer version of the FiT algorithm used in this study includes two major improvements: (i) a new parameter called the "separation distance", and (ii) support for the periodic domain in the zonal direction.

After a precipitation system splits into multiple pieces, some can grow to large sizes and move farther away from the other pieces, particularly in regions such as the Inter-tropical Convergence Zone (ITCZ) and cold fronts. If these breakaway pieces are considered to be part of the same system, it can lead to an unrealistic estimation of the system's lifetime, accumulated rain volume, and frequency. This led to the development of a new user-defined parameter called "separation distance" for the FiT. The separation distance controls when a breakaway piece should become its own system. If the distance between the centroid of a piece and the centroid of the system (all pieces) becomes larger than the separation distance, then the piece is reclassified as a separate system.

The second modification to the FiT allows for a periodic domain in the zonal direction. The IMERG precipitation data has periodic zonal domain boundaries at 180° W to 180° E (dateline). In the earlier versions of the algorithm, the systems crossing the periodic domain boundary were terminated and tracked as a new system on the other side. Since the newer version supports a zonally periodic domain, we can successfully track the precipitation systems traversing the periodic boundary and study their properties without discontinuity near the dateline.

3.3.4 Tracking challenges

Tracking MCSs in IMERG over the global Tropics presented two challenges: (i) the transient precipitation bands that span thousands of kilometers and (ii) differences in PMW sensor resolution and retrievals. A precipitation band that spans thousands of kilometers (fig. 3.1a) is not uncommon in the ITCZ region. These precipitation bands are usually formed when multiple MCSs come together for a short period (< 3 hours) but

break apart later. Past studies have observed superclusters similar to precipitation bands. Leary and Houze (1981) reported the formation of double clusters (akin to a precipitation band) in radar from the interaction of multiple mesoscale precipitation features over the eastern Atlantic Ocean. The precipitation bands could also be connected MCSs observed over the Indo-Pacific warm pool region (Virts & Houze, 2015). These MCSs that join to form a precipitation band are different from the smaller convective cells that coalesce to form a mesoscale system. The precipitation bands are transient with a lifetime of < 3 hours, have distinct mesoscale structures, and lack coherent propagation (fig. 3.1a). However, an MCS is longer lived and propagates as a coherent system. Since a precipitation system's lifetime increases with its size (Machado et al., 1998; Chen and Houze, 1997), one would expect a precipitation band to live longer, yet it is brief. A conventional tracking method, which uses a single threshold to identify contiguous pixels as an object, will track the precipitation band as a short-lived precipitation system. In this method, we lose the tracking information of MCSs that form the band briefly and break later. However, since the FiT algorithm uses the "cascading thresholds" technique to define the extent of objects, it can successfully identify mesoscale objects within a precipitation band and track them individually (fig. 3.1b). These precipitation bands are not infrequent, and the bands with longitudinal width (W) of $\sim 10^\circ$ occur at least once every 30 minutes in the global tropics (fig. 3.3a). The use of cascading threshold does not completely eliminate the identification of precipitation bands but reduces their occurrence to one per day and increases the number of mesoscale objects identified (fig 3.3a). The other challenge in tracking MCSs is the differences between PMW sensors resolution and retrievals in IMERG. PMW precipitation has a nominal resolution that varies from 10

km (for SAPHIR PMW sensor) to 55 km (for SSMIS PMW sensor). Fig. 3.2 presents an MCS's precipitation field observed on 07 June 2018 from the SAPHIR and SSMIS overpass during a half-hour period starting at 04:30 and 05:00 UTC, respectively. The precipitation retrieval from SAPHIR is very noisy compared to SSMIS retrieval (fig. 3.2a and 2d). To mitigate the noise and the resolution differences, we apply the uniform smoothing filter (moving average with the square kernel) of width 0.5° , which is approximately the SSMIS resolution. Despite smoothing, we can see the multicellular structure of the MCS in SAPHIR precipitation retrievals (fig. 3.2b) but absent in SSMIS precipitation retrievals (fig. 3.2e). When the direct cascading thresholds (1, 3, 9, 27) mm h^{-1} are applied to this MCS, it identifies a single object for SSMIS (fig. 3.2e). However, for a multicellular precipitation field of SAPHIR (fig 3.2b), it identifies convective cells within an MCS as objects. Since our objective is to identify MCS and not the convective cells, this is an undesirable behavior of cascading thresholds. This issue would exist even in other tracking algorithms that use DAS-based object identification (Huang et al., 2018).

The cascading threshold technique helps break a precipitation band into multiple mesoscale objects (fig. 3.1b). However, on the other hand, it breaks an MCS into numerous convective cells (fig. 3.2b), which is undesirable. We normalize the IMERG precipitation field by the maximum precipitation rate within each blob to overcome this issue. Normalization transforms the precipitation field to values between 0 and 1. The motivation to use normalization comes from our understanding that the precipitation field is multicellular, with a large precipitation gradient around the heavy precipitation region. Despite differences in precipitation intensity between various PMW sensors or tropical

regions, this structure is similar. Therefore, normalization helps choose a core region that encompasses all cells but is independent of the PMW sensor or region.

The cascading thresholds for the normalized precipitation field are chosen as a series of decimal values between 0 and 1. For example, the cascading threshold (0, 0.11, 0.33) implies that the normalized precipitation with values ≥ 0.33 will represent core objects, and the values ≥ 0.11 and < 0.33 will be relatively moderate rain areas. The region with values > 0 and < 0.11 will present relatively low precipitation values. fig 3.2c and 3.2f show that the normalized cascading thresholds identify an MCS as a single object without breaking it into multiple cells even though the PMW sensors are different. The normalized cascading threshold can be seen as dynamic thresholds that change with the precipitation blob or PMW sensor. In fig. 3.2c, the precipitation blob has a maximum precipitation rate of $\sim 18 \text{ mm h}^{-1}$, and the normalized thresholds of (0, 0.11, 0.33) translate to a physical threshold of $18 \text{ mm h}^{-1} * (0, 0.11, 0.33)$, which are approximately (0, 2, 6) mm h^{-1} . For the precipitation field in fig. 3.2f, the maximum precipitation is 30 mm h^{-1} which approximately translates to (0, 3.3, 10) mm h^{-1} . These dynamically varying thresholds help identify the mesoscale object more appropriately than the direct cascading thresholds. The following subsection discusses how the normalization fits into the tracking procedure and computation of system properties.

3.3.5 Tracking procedure

Before running the FiT tracking, we perform three custom pre-processing steps on the IMERG precipitation field to make it suitable for tracking MCSs. The values for parameters in the pre-processing steps are chosen based on the literature and our

understanding of IMERG. For the FiT tracking, the cascading thresholds and separation distance are the two most important parameters which have a greater influence on its behavior. We determine the optimal value for these parameters through extensive sensitivity tests and visual analysis of fields with identified MCSs.

The three custom pre-processing steps are: i) smooth the IMERG precipitation field, ii) apply precipitation or no precipitation condition, and iii) normalize the precipitation field. In the first pre-processing step, we smooth the IMERG precipitation field with a uniform filter of 0.5° width (coarsest PMW resolution) to mitigate PMW resolution differences and reduce the noise (sudden changes). In the next step, the precipitation rate of 1 mm h^{-1} is used as a precipitation or no-precipitation condition to remove light precipitation that may be spurious. The spurious precipitation affects the precipitation system's area but has little effect on rain volume (Rajagopal et al., 2021). As a final pre-processing step, we identify the contiguous areas (blobs) in the precipitation field and normalize each blob with its maximum precipitation rate. The resulting normalized precipitation field has values between 0 and 1. Though helpful, smoothing tends to extend the regions with precipitation as well as reduce the precipitation extremes, whereas normalization changes the precipitation field to values between 0 and 1. Therefore, we used the smoothed and normalized precipitation field to identify and track the precipitation systems and unsmoothed and unnormalized precipitation to compute systems' properties such as area, rain volume, and maximum rain rate.

3.3.6 Optimal tracking parameters

For the FiT tracking parameters (cascading thresholds and separation distance), we performed extensive sensitivity tests and visual analysis to determine their optimal values. We tested four choices of normalized cascading thresholds: (0, 0.25, 0.50), (0, 0.11, 0.33), (0, 0.06, 0.25), and (0, 0.04, 0.20), and four choices of separation distance: 1°, 2°, 3°, and 4°. Each choice of normalized thresholds is obtained through two-step reduction by a factor from the maximum normalized precipitation value of 1. For example, the thresholds (0, 0.25, 0.50) is obtained when the maximum value of 1 is reduced by a factor of 2 to get 0.50. A further reduction by a factor of 2 is 0.25. The four threshold choices correspond to the reduction factor of 2, 3, 4, and 5, respectively. This technique of determining cascading thresholds by a reduction factor is based on Skok et al. (2013) and White et al. (2017). They tracked precipitation systems in an unnormalized precipitation field and used fixed physical cascading thresholds (40, 56, 80, 120) mm day⁻¹ with a reduction factor of 1.5. In their work, an additional lower threshold of 24 mm day⁻¹ was required for the northeast pacific because there were many systems of lower intensity. We do not require such adjustments for different tropical regions or PMW sensors since the normalization will effectively handle it. For the other tracking parameter, separation distance, we chose to test four options: 1°, 2°, 3°, and 4°, because they are approximately 100, 200, 300, and 400 kilometers and represent mesoscale dimensions.

The four cascading threshold choices and four separation distance choices give 16 possible combinations. We visually analyzed the tracking animation of each combination. Visual analysis is crucial because identifying an isolated MCS is easier both subjectively

and objectively. However, in a precipitation band, different cascading thresholds will identify a different set of mesoscale objects. Since there are no objective criteria to identify an MCS within a precipitation band, we look at the animation to identify the regions of the precipitation band that stayed together and the regions that did not. Hence visual analysis is vital to determine the cascading thresholds that were close to human identification and tracking. Since the visual examination is tedious and time-consuming, we performed this analysis only for 15 days (01 – 15 June 2018) over a smaller domain of the tropical Atlantic Ocean (60° W to 10° W and 10° N to 5° S). We prioritized choices that tracked MCSs without premature termination during this analysis than missing out on a small cell in the periphery. If a small cell is left out, it will slightly affect the system's area and rain volume, but system properties such as lifetime and propagation velocity are least affected. However, a premature termination will severely affect properties such as lifetime, propagation velocity, accumulated rain volume, and MCS frequency.

Our visual analysis showed that the separation distance had a more significant impact on systems' size than the cascading thresholds. Though not perfect, the separation distance of 2° performed more reasonably. The values of 3° and 4° more often produced connected MCS or treated two mesoscale objects that are farther apart as a single tracked system. However, the separation distance of 1° frequently excluded cells on the periphery, which is also undesirable. For the next tracking parameter, cascading thresholds, the choices (0, 0.11, 0.33) and (0, 0.06, 0.25) identified objects more effectively than others. The cascading thresholds (0, 0.04, 0.20) often identified connected MCSs as a single object but the values (0, 0.25, 0.50) sometimes broke an

MCS into cells. There were no perfect tracking parameters, but the normalized thresholds (0, 0.11, 0.33) and separation distance of 2° did relatively well compared to other combinations. Two animations of an MCS over the Amazon basin are provided as supplemental materials, each with different tracking parameter values. One showcases the working of the FiT algorithm with optimal parameters values of normalized thresholds (0, 0.11, 0.33) and a separation distance of 2° . The other animation illustrates the issue of premature termination when convective cells are identified as objects for fixed physical thresholds (1, 3, 9, 27) mm h^{-1} and a separation distance of 2° .

The visual analysis of tracking animation helped us understand the workings of the FiT algorithm, but it is still a partly subjective analysis. Therefore, we performed sensitivity tests over the global tropics (30° N to 30° S) and tracked the precipitation systems for 24 hours on 100 random days between 2001 and 2020. The sensitivity test is run only for seven combinations of parameters since the test was computationally expensive. The visual analysis showed that cascading thresholds of (0, 0.11, 0.33) and separation distance of 2° performed reasonably. Hence for the first sensitivity test, we fixed the separation distance of 2° and varied the four choices of cascading threshold (fig. 3.3a). Similarly, for the second sensitivity test, we fixed the cascading thresholds of (0, 0.11, 0.33) and varied four choices of separation distance (fig. 3.3b). Though precipitation systems can last longer, tracking them for one day would be sufficient to understand the effect of various choices. The first six hours of each random day were treated as a spin-up time for the tracking algorithm. We used the tracking data from the remaining 18 hours to assess the choices of the tracking parameters by comparing the precipitation object or system's longitudinal width (W), as shown in fig.3.3. The longitudinal width of an object

or a system is the longitudinal difference between the westernmost and the easternmost grid cells. We use longitudinal width since it is intuitive as most precipitation bands in the ITCZ are zonally oriented (Liu and Zipser, 2013). If a precipitation system has multiple pieces after splitting, then the longitudinal width is computed for the entire group.

Fig. 3.3a shows that all "cascading thresholds" choices identify fewer precipitation bands as objects than the conventional tracking method. We imitate conventional tracking by running the FiT algorithm with a single physical threshold of 1 mm h^{-1} and a separation distance of 2° . The cascading thresholds broke the precipitation bands into more mesoscale objects smaller than 4° wide. Amongst various choices of "cascading thresholds", the values (0, 0.11, 0.33) have a lower frequency of precipitation bands ($W \geq 10^\circ$) by two orders of magnitude than conventional tracking.

When we compared different choices of separation distance, in fig. 3.3b, for the same cascading thresholds (0, 0.11, 0.33). As expected, the frequency of precipitation bands ($W \geq 10^\circ$) increased with separation distance because an object that broke off will continue as part of the parent system if the separation distance is large. Though the values 1° and 2° have a similar frequency of precipitation bands in the sensitivity test, during our visual analysis, we found that 2° did better. Hence, we chose the cascading thresholds (0, 0.11, 0.33) and separation distance of 2° as optimal tracking parameters. We used these optimal parameters to track precipitation systems in IMERG for ten years, from 2011 to 2020. The precipitation systems that satisfy our MCS criteria are stored in a publicly available dataset called Tracked IMERG Mesoscale Precipitation System (TIMPS; Russell et al., 2022).

3.3.7 TIMPS dataset

There are approximately 2.3 million tracked precipitation systems each year, but only the systems that satisfy our MCS criteria, approximately 160,000, are stored in the TIMPS dataset. A precipitation system is classified as an MCS if it meets all three criteria: i) it reaches a maximum area of 3000 km² or larger, ii) it exists for six hours or longer, and iii) it has a maximum rain rate of 10 mm h⁻¹ or more at least once during its lifetime. The criterion for the maximum size of 3000 km², though subjective, is based on past studies. Our size criterion is between 5000 km² used by Williams and Houze (1987) on IR data and 2000 km² used by Nesbitt et al. (2000) on PR data. The next criterion limits MCSs as tracked systems with a lifetime of six hours or longer and assumes that a large system lives longer. A similar criterion was used by Evans and Shemo (1996). The final criterion of maximum precipitation rate of 10 mm h⁻¹ ensures that an MCS has a stronger convective cell (Feng et al., 2021). Though these are subjective choices, they may affect the quantitative values such as MCS frequency and rain contribution. However, the qualitative conclusions and the observed regional differences will remain the same. This study specifically omits any MCSs close to tropical cyclones (TC) or those touching the northern or southern domain boundaries at any timestep during their lifetime. An MCS is assumed to be influenced by or part of a TC if its centroid is less than twice the TC radius distance from the cyclone's center. Such MCSs are marked in the TIMPS dataset as "near TC"(Russell et al., 2022). Tropical cyclones' track, center, and radius information are

obtained from the International Best Track Archive for Climate Stewardship (IBTrACS; Knapp et al., 2010).

For each MCS, properties such as area, volumetric rain rate (also referred to as rain volume), maximum rain rate (also referred to as precipitation intensity), weighted centroid, and propagation velocity are computed at every timestep and stored in a netCDF file. We use only these MCS properties in our study, but a complete list of MCS properties is described in Russell et al., (2022). Area, A (km^2), is the sum of all pixel areas inside an MCS. It is important to note that pixel area changes with latitude.

Volumetric rain rate, VRR ($\text{km}^2 \text{mm h}^{-1}$), is the sum of the products of pixel rain rate and pixel area. The maximum rain rate, MaxRR (mm h^{-1}), is defined as the maximum of rain pixel values in an MCS. Weighted centroid, expressed in latitude and longitude, is the rain weighted mean of latitudinal values of all pixels, and rain weighted mean of longitudinal values of all pixels, respectively. The weighted centroid computation accounts for the periodic zonal boundary at the dateline. Propagation velocity, PV (m s^{-1}), is the ratio of the geodesic distance between MCS's weighted centroid in consecutive timesteps and time, i.e., 1800 seconds. Lifetime, L (h), is not stored in the file, but it is computed as half the number of timesteps an MCS was tracked since each timestep is 30 minutes long.

MCS properties such as area, volumetric rain rate, maximum rain rate, and propagation velocity are available at each timestep and change as an MCS evolves. These property values at each timestep are instantaneous values and denoted with a subscript "inst". In addition, we can compute lifetime statistics such as maximum or average from instantaneous property values; for example, the instantaneous area at each timestep is

denoted as A_{inst} , and the maximum area attained during an MCS lifetime is denoted as A_{Lmax} . We use either instantaneous or lifetime statistics as we see fit to describe the probability and spatial distribution of MCS properties.

3.4 Results

The following subsections discuss the MCSs' rain contribution, frequency, and spatial variability of MCS properties in the global tropics. Since we ignore the MCSs that touch north and south domain boundaries, it creates a data void near the boundaries. Therefore, we present only the spatial distribution of MCS properties from 28° N to 28° S.

3.4.1 Rain contribution

IMERG provides much better annual precipitation and MCSs rain contribution than the IR and space-borne precipitation radars. This is because IR-based precipitation has a negative bias over regions with warmer cloud top temperatures from weak convection intensity and the dominant warm rain process. On the other hand, the non-precipitating anvil with a cold cloud top temperature might be mistaken for stratiform rain, leading to positive biases (Liu et al., 2007; Berg et al., 2002; Woodley et al., 1980). The space-borne PR precipitation values are closer to surface observations; however, they do not provide annual precipitation amounts due to poor temporal resolution.

Fig. 3.4 presents the IMERG annual precipitation and MCSs annual rain contribution averaged over ten years (2011-2020) at the native IMERG resolution ($0.1^\circ \times 0.1^\circ$).

IMERG annual precipitation is closer to surface observations at large spatial and time scales since rain gauge derived bias corrections are applied at 1° spatial and monthly

accumulation (Tan et al., 2017). Prominent land locations with copious annual precipitation ($>3000 \text{ mm yr}^{-1}$) are the Pacific coast of Colombia; the upper Amazon basin; the west coasts of Sierra Leone, Myanmar, and Sumatra; the east and west coast of New Guinea; and the north coast of Borneo. Though central Africa has a higher frequency of intense thunderstorms (Bang and Zipser, 2016; Zipser et al., 2006), its annual precipitation is lower than coastal Cameroon. On a large scale, the ITCZ over the Maritime Continent, the adjacent western Pacific Ocean, and the eastern Indian Ocean are heavy rain producers. The convection over this region significantly impacts the global meridional and zonal atmospheric circulation (Houze et al., 1981; Krishnamurti et al., 1973; Ramage, 1968).

The spatial distribution of MCSs annual precipitation in fig. 3.4b looks similar to IMERG annual precipitation. The MCSs contribution to annual precipitation is about 70 to 90% in the ITCZ region and decreases as we approach the north and south domain boundaries (fig. 3.4c). This percentage is slightly higher than earlier studies (Nesbitt and Zipser 2000; Liu 2011; Feng et al. 2021), probably due to the coarse PMW resolutions missing smaller precipitation systems and our less restrictive MCS criteria. Though the double ITCZ in the Pacific Ocean is conspicuous during boreal spring, the annual accumulation is small. The MCSs rain contribution reveals that major rain-producing convective systems in the double ITCZ and the western Indian Ocean are mesoscale.

In fig. 3.5, we present the MCSs rain contribution as a function of their characteristic properties, namely Area ($A_{L_{\max}}$) and lifetime (L). The MCSs contribute $\sim 70\%$ of annual tropical precipitation, though they account for $\sim 7\%$ of all tracked precipitation systems in this study. The rain contribution increases with size up to $\sim 10^5 \text{ km}^2$ and decreases beyond

this size (fig 3.5a). This scale break can also be seen in the MCS frequency distribution in fig. 3.7a. Past studies attributed this scale break to different physical processes in large systems and limits to growth (López, 1977). The MCSs with a lifetime < 24 hours contribute 80% of annual tropical rainfall, and they follow a diurnal cycle with a maximum frequency at specific local times (Nesbitt and Zipser, 2003). The maximum rain contribution is from MCSs that live for 18 hours (fig. 3.5b).

3.4.2 MCS frequency

Calculation of rain contribution at each IMERG pixel ($0.1^\circ \times 0.1^\circ$) proved tedious and computationally expensive. Therefore, the MCS path or track is used in the following subsections to capture the spatial distribution of MCS frequency and its properties. For this purpose, we divide the study domain ($30^\circ \text{ N} - 30^\circ \text{ S}$) into coarser $1^\circ \times 1^\circ$ grid cells. Then, each MCS and its properties are linked to grid cells through which the MCS's weighted centroid traverses during its lifetime.

The MCS track frequency presented in Fig. 3.6a shows that 80 - 100 MCSs occur each year over ITCZ regions of tropical oceans, but 50% more MCSs occur over much of the Maritime Continent and the western Amazon Basin. Though the western Pacific Ocean receives more annual rainfall than the Maritime Continent, it has fewer MCSs. This implies that the MCSs over the western Pacific produce more rain per system. In equatorial South America, the high frequency of MCSs occurs over Brazil's north coast near the mouth of the Amazon River, the western Amazon basin, and Colombia's Pacific coast. Africa has relatively fewer MCSs than other equatorial land regions except for

locations around Lake Victoria. There are few or no MCSs over northern Africa, the southeast Atlantic Ocean, and the southeast Pacific Ocean.

Comparing the MCS frequency with the lightning frequency (Fig 3.6b) reveals the different convective regimes over various tropical land areas. Zipser et al. (2006) showed that convection over central Africa has higher flash rates (a proxy for intense convection) than in the Amazon basin and Maritime Continent. In contrast, Fig. 3.6a shows fewer MCSs over central Africa than in the Amazon basin and Maritime continent. The environment that produces small and intense convective systems over central Africa must be very different from the environment that favors MCSs over the Amazon basin and Maritime Continent. Comparing the environmental conditions between these land regions might help understand the factors and lead to developing or tuning the parameterization schemes for the different convective regimes.

Complementary to spatial distribution, the frequency distribution of MCS occurrence by maximum area (A_{Lmax}) and lifetime (L) is presented in Fig. 3.7. From this figure, we infer that in the global tropics, ~ 99% of MCSs have a size $< 10^5 \text{ km}^2$ (fig. 3.7b), and they contribute 80% of IMERG annual precipitation (fig.3.5b). Similarly, 90% of MCSs in the global tropics have a lifetime < 24 hours (fig. 3.7d), and they contribute 80% of IMERG annual precipitation (fig. 3.5d). In addition to these statistics, the frequency distribution is useful for understanding the statistical nature of convection. Lopez (1977) argued that rain area size distribution follows a log-normal function since the cloud growth through entrainment is a random process that follows the law of proportionate effects. If the MCS size distribution follows a log-normal distribution, its cumulative distribution function (CDF) on a gaussian scale would appear as a straight line (fig. 3.7b). The MCS size

distribution from this study (fig. 3.7b) looks similar to the size distribution reported in Mapes and Houze (1992), and both are not straight lines on the gaussian scale. Past studies attributed the deviation from log-normal function to the truncated distribution and limits to growth at the larger sizes (Mapes and Houze, 1992; López, 1977).

We think the deviation from log-normal distribution is more subtle than just truncated distribution at large sizes. In fig. 3.7a, the size distribution for all tracked systems (MCSs and non-MCSs) follows a power-law function with a slope close to -1. The MCS-only size distribution departs from this power law distribution because of the MCS criteria imposed on lifetime and precipitation intensity. In the past studies, the size distribution was attributed to one of these parametric distributions: power law (Jiang et al., 2008; Neggers et al., 2003; Benner and Curry, 1998), exponential (Wielicki & Welch, 1986), and log-normal (Mapes and Houze, 1992; Williams and Houze, 1987; Lopez 1977). We suspect there are various reasons for associating different parametric functions for size distribution: (i) no observation can completely capture the size spectrum of convective clouds leading to a truncated distribution, (ii) imposing multiple MCS criteria changes the distribution, and (iii) the truncated distribution looks similar to all three parametric functions. Mesnard and Sauvageot (2003) showed that the truncated radar rain area distribution fit all three parametric functions (exponential, power-law, log-normal) with minimal error. The truncation can be on the smaller or larger end of the size spectrum. Surface radars can observe small, deep convection but miss out on shallow convection and only partially capture large MCSs. In contrast, satellites can observe large MCSs but miss out on smaller systems due to coarser resolution.

Though determining the parametric function for size distribution could be challenging for the above reasons, the frequency distribution is still useful for model validation. The frequency and cumulative distribution of all precipitation systems in fig. 3.7a and fig. 3.7c can be compared to global climate models to evaluate if they simulate a similar number of precipitation systems for a given size or lifetime.

3.4.3 Area

The spatial distribution of MCSs' area is presented in fig. 3.8. This plot and figures 9, 10, and 12 for other MCS properties have similar panels. Panels a and b show the frequency of small and large property values, whereas panel c shows the property value at the 90th percentile from all MCSs occurring at that location. Presenting frequency in absolute numbers and property's percentile value provide different perspectives. The frequency, in absolute numbers, tells us which region has a high occurrence of specific MCS categories (large, intense precipitation, long-lived, and fast-moving). In a complementary view, the property value at the 90th percentile characterizes most MCSs occurring at that location. Comparing fig. 3.8a and fig. 3.8b reveals the regional differences in MCSs size. The smaller MCSs occur more often over the Maritime Continent, Amazon basin, around Lake Victoria, and Ethiopian highlands. Although tropical oceans have a significant number of smaller MCSs, they have a higher frequency of large MCSs than land, possibly due to the larger stratiform region of oceanic MCSs (Houze et al., 2015; Schumacher and Houze, 2003). This difference is also visible in the percentile plot, with oceans having slightly larger MCSs at the 90th percentile (fig. 3.8c).

The eastern Indian Ocean and the western Pacific Ocean have the highest frequency of large MCS than other tropical regions. These large systems are likely associated with the active phase of Madden Julian Oscillation (Virts and Houze, 2015; Chen et al., 1996).

Over equatorial South America, the Amazon basin has a higher occurrence of large MCSs similar to the ocean (Rasmussen et al., 2016; Schumacher and Houze, 2000).

Nearby, the offshore locations near Colombia's Pacific coast also have a higher frequency of large MCSs with broad stratiform regions. These MCSs have strong upper tropospheric heating, and they sometimes develop into easterly waves and tropical cyclones (Molinari et al., 2000; Rydbeck & Maloney, 2015).

In the percentile plot (fig. 3.8c), the strong contrast between onshore and offshore MCS size can be observed over the Maritime Continent; west coasts of Colombia, Cameroon, India, and Myanmar; and the northern Bay of Bengal. Other notable regions with large MCSs at the 90th percentile are subtropical locations east of Hawaii in the North Pacific Ocean and locations on either side of the dateline in the south Pacific Ocean. These MCSs are probably due to the influence of mid-latitude synoptic-scale systems. Such regions do not show up in the frequency plot (fig. 3.8b) because the total MCS frequency is low, but many of them have large areas. This demonstrates the usefulness of the percentile plot.

Regional studies have described various processes that may create onshore and offshore differences mentioned in the previous paragraph. Houze et al. (1981) reported that the MCSs are larger offshore than over the islands in the Maritime continent region. They found that the daytime heating and sea breeze circulation initiate deep convection over the islands in the late afternoon, which grows into mature MCSs before midnight. The

outflow from the land convection or land breeze triggers new convection offshore around midnight, which then grows into a mature MCS the following morning near 0900 hours local time. These MCSs dissipate in the afternoon as new convection develops over land. The MCSs' lifetime in fig. 3.11c also shows a strong contrast between offshore and islands of the Maritime Continent. These offshore MCSs live longer; hence have more time to grow into a larger system. Similar processes must play a role at other offshore-onshore locations such as the west coast of Colombia and Cameroon. However, over the west coast of India and Myanmar, the MCSs do not have the typical squall line or non-squall line structure described in Houze (2004). These offshore MCSs with large areas form from the interaction of synoptic-scale monsoon winds and coastal mountains during boreal summer (Houze et al., 2015). Hence diurnal land and sea breeze circulations have a weak influence.

3.4.4 Precipitation intensity

We consider the maximum rain rate of an MCS to represent its precipitation intensity. The spatial distribution of the maximum rain rate ($\text{MaxRR}_{\text{inst}}$) is shown in fig. 3.9. The moderate rain rates ($10 - 30 \text{ mm h}^{-1}$) occur more frequently over land and coincide with locations of smaller MCSs (fig 3.9a). The heavy rain rates ($50 - 100 \text{ mm h}^{-1}$) often occur offshore of the west coasts of Colombia, Cameroon, Myanmar, Sumatra, and Borneo. Farther from the coasts, the heavy rain rates also occur over open oceans of the western Pacific, eastern Pacific, eastern Indian Ocean, and the Bay of Bengal; however, they are less frequent than in some coastal areas. The inland tropical regions have a lower frequency of heavy precipitation rates except in the Amazon basin. In short, the

frequency of heavy precipitation rates decreases from the coastal areas to the open ocean basins to land regions.

The land-ocean contrast in the frequency of heavy precipitation is surprising, and it is possibly due to differences in PMW retrievals or the nature of convection. GPROF uses both low frequency (emission) and high frequency (ice scattering) PMW channels for precipitation estimates over the ocean but only high-frequency PMW channels for precipitation estimates over land. This might have led to the observed differences between land and ocean. Nevertheless, it is also possible that the differences in precipitation intensity are due to differences in the nature of convection. Hamada et al. (2014) studied the extreme precipitation over the tropics using TRMM precipitation radar with a spatial resolution of ~ 5 km. They found that extreme precipitation exists over tropical land areas with values greater than 50 mm h^{-1} , but these precipitation features are small and occur between 1200 - 1800 hours local time. Zipser et al. (2021) and Wang et al. (2020) noted that mesoscale-sized features with extreme precipitation but weak convection intensity (category: R-only medium) occurred mainly over oceans and the Amazon basin region in the global tropics. This led us to believe that heavy precipitation over central Africa and other land regions must occur over a narrow area that is too small to be shown accurately with coarse PMW sensor resolutions. We plan to explore this issue in the future to understand the reason for the observed land-ocean differences in IMERG's heavy precipitation rates.

The land-ocean differences also show up in the 90th percentile value of maximum rain rates, with different ocean basins having higher values than land (fig. 3.9c). Other regions that stand out are central America and Peru, with MCSs of moderate rain rates; the Bay

of Bengal and the Arabian sea have a higher fraction of MCSs with heavy rain rates. We can see this regional variation only in the percentile plot and not in the frequency plots (fig. 3.9a and fig. 3.9b) because only a few MCSs occur over these regions.

3.4.5 Lifetime

Unlike the MCS's area or maximum rain rate that evolves with time, their lifetime and average propagation velocity have the same values attached to grid cells along an MCS track. In fig. 3.10a, many MCSs with shorter lifetimes (6 - 9 hours) occur over the Amazon basin, around Lake Victoria, Ethiopian highlands, and the Maritime continent. These regions also have a higher occurrence of small MCSs with moderate precipitation. The long-lived MCSs occur more often over the ITCZ region of tropical oceans, the west coasts of Colombia, India, Myanmar, and the Amazon basin (fig. 3.10b). Over the mountainous, coastal, or large lake regions, the diurnally varying mesoscale circulations such as upslope-downslope flows or land-sea breeze might affect an MCS lifetime. In contrast, the open tropical oceans have many long-lived MCSs, probably because of the weak diurnal cycle and the lack of mountain barriers.

Over the Maritime Continent, the diurnally varying land and sea breeze circulations play a major role in convection initiation and their lifetime. These offshore convection are long-lived and have large areas (Houze et al., 1981; Chen and Houze, 1997). Though convection over many land areas weakens or dissipates due to diurnally varying mesoscale circulations, the Amazon basin and West Africa have been observed to have active convection at night. Besides having many short-lived MCSs, the Amazon basin

also has a higher frequency of long-lived MCSs. Houze et al. (2015) and Liu et al. (2008) noted that convection over the Amazon region is weaker and shallower than other land regions but similar to oceans. In addition, we find that the Amazon basin has a higher frequency of large and long-lived MCSs similar to oceans; hence the region is aptly named as "green ocean" (Silva Dias et al., 2002). Nevertheless, the Amazon basin is also similar to other land regions by having many small and short-lived MCSs, possibly due to a strong diurnal heating cycle. Another region of interest is west Africa; though it has only a few MCSs, a large fraction of them are long-lived. Therefore, it does not show up in the frequency plot (fig. 3.10b), but its 90th percentile value is comparable to open oceans (fig. 3.10c).

Early studies over the Amazon basin found that squall lines form near the mouth of the Amazon River due to sea breeze circulation (Garstang et al., 1994; Greco et al., 1990). Some of these squall lines are long-lived and propagate into central and upper Amazon basins. Though other squall lines are short-lived and dissipate inland closer to the coast, they may trigger new convection downstream that propagates into the central and upper Amazon basin (Anselmo et al., 2021). These long-lived MCSs terminate near the eastern foothills of the Andes, which acts as a barrier and prevents further propagation. The barrier effect of the Andes is clearly seen in fig. 3.10b. However, the squall lines over west Africa propagate into the adjacent Atlantic Ocean without any hindrance. In the Amazon basin and west Africa, MCSs grow at night despite the nocturnal stable boundary layer. This is possible because of the moist low-level jet that feeds the convection (Anselmo et al., 2020; Janiga and Thorncroft, 2016; Hodges and Thorncroft,

1997; Houze and Betts, 1981), or the cold pools, denser than nocturnal stable boundary layer (Provod et al., 2016), lift the near-surface moisture.

A notable regional difference is that the eastern Pacific has more long-lived MCSs than the western Pacific (similar to White et al., 2017). Likewise, there are many long-lived MCS in the eastern Atlantic Ocean than in west Africa (similar to Houze and Betts, 1981; Hodges and Thorncroft, 1997). At the 90th percentile, most MCSs over central America and Peru are short-lived. In contrast, the Bay of Bengal, the Arabian Sea, and the west coasts of India and Myanmar have MCSs with lifetime > 24 hours, most likely associated with the boreal summer monsoon.

3.4.6 Propagation velocity

The instantaneous propagation velocity, PV_{inst} , is computed from the translation of a system's weighted centroid in consecutive time steps. From the instantaneous velocities during an MCS lifetime, we compute the median propagation velocity and maximum propagation velocity of an MCS. Fig. 3.11a shows that the frequency distribution of the median propagation velocity peaks at 10 m s^{-1} , which is unrealistic for MCSs over the tropics. Though some squall lines over west Africa and the Amazon basin have velocities $10 - 16 \text{ m s}^{-1}$ (Houze and Cheng, 1977; Kingsmill and Houze, 1999; Anselmo et al., 2021), many MCSs have slower propagation speeds in the tropics. The high median propagation velocity values are likely due to shape changes during a system's evolution, particularly from rapid change during a merger or split, which shifts the centroid quickly to create a false instantaneous propagation speed of $20 - 50 \text{ m s}^{-1}$ (fig. 3.11b). Therefore, we compute the average propagation velocity (PV_{Lavg}) between the start and end

positions of the system's weighted centroid without using the instantaneous values, thereby minimizing the error. In fig. 3.11a, the frequency distribution of average propagation velocity peaks at 5 m s^{-1} , which is typical for tropical precipitation systems. The frequency distribution also has a few MCSs with average speeds between 10 and 15 m/s, which are probably squall lines.

The spatial distribution of average propagation velocity is presented in fig. 3.12. The slow-moving MCSs ($0 - 5 \text{ m s}^{-1}$) occur more often over Colombia's pacific coast (both onshore and offshore), the west coast of India, and the Maritime Continent. Previous subsections discussed that MCSs onshore of Colombia's pacific coast are smaller, short-lived, and have moderate rain rates. However, being a slow-moving system, these MCSs produce flash floods and landslides over this region (Poveda et al., 2020). The MCSs over the maritime continent are bound to stay over land until convection moves offshore around midnight (Williams & Houze, 1987). Hence slower propagation velocity.

The fast-moving ($10-15 \text{ m s}^{-1}$) MCSs frequently occur over the Amazon basin, west Africa, western and central Pacific Ocean. The coastal squall lines that form near the mouth of the Amazon River and the squall lines over west Africa usually propagate at speeds between 10 and 16 m s^{-1} (Janiga and Thorncroft, 2016; Hodges and Thorncroft, 1997; Garstang et al., 1994; Tang et al., 2016). These squall line MCSs have a leading convective line and a trailing stratiform region. The mesoscale downdrafts, which form from the evaporation of stratiform precipitation, transport momentum from ambient winds at mid-troposphere and low-level jets to the surface (Houze, 2004; Zipser, 1977). Such momentum transport through downdrafts into cold pool outflow causes the squall lines to propagate faster than non-squall line MCSs. The momentum transport from low-

level jets over the Amazon basin (Anselmo et al., 2020) and the easterly jet over west Africa (Houze and Cheng, 1977; Houze and Betts, 1981; Mathon and Laurent, 2001) may contribute to the observed fast propagation speeds in these regions.

Over the western Pacific Ocean, there are higher frequencies of fast-moving MCSs similar to Africa and Amazon. Chen et al. (1996) also reported many westward-moving MCSs with a velocity of 10-15 ms⁻¹ over this region. During the Tropical Ocean Global Atmosphere Coupled Ocean-Atmosphere Response Experiment (TOGA COARE) field program, Kingsmill and Houze (1999) reported a higher occurrence of non-squall line MCSs and fewer squall lines over the western Pacific region. They also noted that many non-squall line MCSs had slower propagation speeds, but some had propagation speeds ≥ 10 ms⁻¹. The squall line's structure aids the momentum transport from the middle or lower troposphere to the surface, but non-squall lines are less effective in momentum transport (LeMone et al., 1984). Further research is required to understand the mesoscale mechanism behind the fast-propagating MCSs in the western Pacific and the possible role of faster synoptic-scale winds in their propagation.

Fig. 3.12c reveals the regional contrast in propagation speed between west Africa vs. the eastern Atlantic, offshore vs. onshore locations of the Maritime Continent, and the eastern vs. western Pacific Ocean. The regional difference between west Africa and the eastern Atlantic had been reported in past studies (Hodges & Thorncroft, 1997b; Martin & Schreiner, 1981). Houze and Betts (1981) reported a higher occurrence of squall lines over west Africa than in the eastern Atlantic. Though the synoptic conditions might vary slightly over the shorter distances between west Africa and the eastern Atlantic, squall lines often occur over west Africa. This is because of stronger cold pools over west

Africa from its deeper and drier boundary layer (Provod et al., 2016), which help organize the convection into a squall line. The percentile plot (fig. 3.12c) also shows that most MCSs over central America, Peru, and the west coast of India are slow-moving. Most MCSs close to the northern and southern domain boundary are fast-moving, possibly due to the influence of mid-latitude synoptic systems and westerlies.

3.4.7 Motion vector

Similar to propagation speed, the propagation direction is affected by mergers and splits, creating an incorrect direction due to shape changes. Therefore, we plot a motion vector that connects the start and end position of an MCS. Fig. 3.13a shows the motion vector of MCSs with a lifetime between 24 to 48 hours from 2017. Only the long-lived MCSs were chosen to reduce computation time and avoid clutter. These long-lived MCSs are adequate to understand the MCSs movement broadly.

The MCSs motion vectors for boreal summer (JJA) and winter (DJF) months exhibit interesting regional and seasonal differences (fig. 3.13b and fig. 3.13c). The Pacific and Atlantic ITCZ have most MCSs moving westward in both seasons. However, over the Indian ocean, the MCS direction is different during the boreal summer and winter months due to monsoonal circulation changes. During the boreal summer monsoon, the MCSs move eastward with monsoon winds over regions such as the Arabian sea, Bay of Bengal, Southeast Asia, East Asia, and the northern-equatorial Maritime continent. However, during boreal winter, the MCSs over the northern-equatorial Maritime Continent move westward with the returning trade winds. After crossing the equator, these trade winds become westerlies associated with the Australian monsoon. Therefore, the MCSs in the

southern-equatorial Maritime Continent moves eastward in the Australian monsoon winds.

Another region with strong seasonal contrast is the Amazon basin. Most MCSs are north of the equator during boreal summer and move westward. However, during boreal winter, the MCSs are south of the equator and move westward and eastward. Past studies have reported alternating easterly and westerly wind regimes over the Amazon basin during boreal winter that affects MCS propagation (Cifelli, 2002; Halverson et al., 2002; Liebmann et al., 2009; Anselmo et al., 2021).

Another notable feature in motion vectors is the double ITCZ over the Pacific Ocean (fig. 3.13a). Though this is common in boreal spring (MAM), some MCSs occur over this region during boreal winter, most likely in the later months. Farther from the ITCZ region and closer to the northern and southern domain boundary, the influence of mid-latitude westerlies is recognizable as far as 15° N and 15° S. This explains the fast propagation velocity and large MCS area reported in sections 3c and 3f over locations east of Hawaii and on either side of the dateline.

3.4.8 Relationship between MCS properties

Previous subsections discussed the spatial distribution of various MCS properties and their regional differences. In fig. 3.14, the relationship between MCS maximum area (A_{Lmax}) and other properties is explored through a joint histogram. Fig. 3.14a shows that the MCS lifetime increases with MCS size, but some large MCSs also have a shorter lifetime, possibly due to mergers. When a merger occurs, the FiT tracking algorithm terminates tracking of all systems but one with maximum overlap with the object in next

timestep. The correlation between MCS size and lifetime is 0.65, but the correlation would be higher for tracking algorithms that retroactively tag all objects that merged as the same MCS. A similar relationship between MCS size and lifetime had been reported in past regional studies (Chen and Houze, 1997; Machado et al., 1998; Laurent et al., 2002).

Like lifetime, the accumulated rain volume increases with MCS size and has the highest correlation of 0.94 because the large MCSs have more rain pixels and a longer lifetime. The next MCS property, maximum rain rate, has a weak correlation of 0.52 with MCS size. It increases with size up to $2 \times 10^4 \text{ km}^2$; above this value, there is no discernable relationship between them. The relationship between MCS size and average propagation velocity is even poorer. This is expected since the propagation speed depends mainly on environmental factors such as ambient winds and the strength of the cold pool, which is in turn influenced by mid-tropospheric relative humidity, boundary layer depth, and humidity.

3.5 Summary

Scarce surface observations over tropical oceans and most tropical land areas make satellite data valuable for studying MCSs and their properties in these regions. Past studies that tracked MCSs with satellite IR data are regional and for a limited period. The access to faster computing and the availability of global rainfall data every 30 minutes over the past two decades has enabled us to track MCSs for ten years. Our regional comparisons are more consistent than previous local studies since we use the same FiT tracking algorithm over the entire tropics.

The FiT program is a generic tracking algorithm and requires tuning to work reasonably with IMERG. Two major challenges to tracking MCSs in IMERG were: i) PMW sensors that may or may-not detect multicellular structures depending on the resolution, and ii) precipitation bands or superclusters that are actually connected MCSs. We smooth the IMERG precipitation field to mitigate PMW resolution differences. The cascading thresholds of the FiT algorithm can detect mesoscale objects in precipitation bands. However, cascading thresholds with fixed set of precipitation values break a multicellular MCS into many objects, which is undesirable. To overcome this problem, we normalize the smoothed IMERG precipitation by the maximum precipitation rate within each contiguous precipitation area. Smoothing and normalizing alter the precipitation field, but they are essential to tracking precipitation systems. Therefore, we track MCSs in the smoothed and normalized precipitation field and use unsmoothed and unnormalized precipitation to calculate MCS properties. We did an extensive visual analysis and sensitivity tests to determine the optimal values for two important tracking parameters (cascading threshold and separation distance). Then, these optimal values were used to track MCSs for ten years (2011-2020) over the global tropics and stored in the publicly available TIMPS dataset.

Using the ten years of tracked data, we analyzed the spatial variability of MCSs' rain contribution, frequency, area, precipitation intensity, lifetime, and propagation velocity. Though MCSs are only 7% of all tracked precipitation systems, they contribute nearly 70% of annual precipitation over the tropics. Spatially, this percentage varies between 70-90% near ITCZ and decreases away from it. Comparing the MCS occurrence and lightning flash rate reveals different convective regimes over tropical land regions. MCSs

occur more often in the Amazon basin and the Maritime Continent than in central Africa, but central Africa has higher lightning flash rates.

Investigation of MCS properties shows two contrasting groups: land vs. ocean and onshore vs. offshore. The MCSs over most land areas are smaller and short-lived than oceans except in the Amazon basin. A similar contrast is observed over onshore and offshore coastal locations such as the Maritime Continent; and the west coasts of Colombia, Cameroon, India, and Myanmar. The positive correlation between MCS size and lifetime partially explains this observation. Though land-ocean contrast has been widely studied, further investigation is needed to understand this offshore-onshore contrast. In addition to boundary layer differences between land and ocean, the mesoscale circulations such as land-sea breeze and upslope-downslope flow from coastal mountains might contribute to differences between onshore and offshore locations.

Another land-ocean dichotomy is observed in precipitation intensity with a higher frequency of maximum precipitation rate over the ocean than on land. This contrast is surprising since heavy precipitation had been reported over land. We hypothesize that this is either due to PMW retrievals differences between land and ocean or the nature of convection. We hypothesize that convection over land has narrow heavy rain areas, which are smeared over too large an area by the coarser PMW resolution. Further research is required to understand this dichotomy.

MCSs' propagation velocity also showed some intriguing global distribution but had no distinct land-ocean contrast. Fast-moving MCSs often occur over the Amazon basin, west Africa, and the western Pacific Ocean. Early studies have reported fast propagating squall line MCSs over the Amazon basin and west Africa. However, the higher frequency of

fast propagating MCSs over the western Pacific needs further investigation. The propagation direction of MCSs over the Pacific and Atlantic ITCZ is mostly westward throughout the year, whereas MCSs over the Maritime Continent region exhibit a noticeable seasonal shift in their propagation direction associated with monsoon circulation changes.

Summarizing the regional MCS properties, we find that MCSs over the Amazon basin exhibit the characteristics of both land and oceanic MCSs. Early studies referred to the Amazon basin as a green ocean due to its shallower convection and larger MCS area, the characteristic properties of oceanic MCSs. In addition, we find that some of the Amazonian MCSs are long-lived and possibly have wider heavy rain cores (detectable as maximum precipitation rates in PMW sensor) similar to oceans. Some of the interesting regional differences are that the eastern Atlantic has a higher occurrence of large and long-lived MCSs than west Africa; however, the MCSs over west Africa are fast-moving. The western Pacific Ocean has a higher occurrence of large and fast-moving MCSs than the eastern Pacific, but the MCSs over the eastern Pacific are long-lived. Regional variations observed in the percentile plots are the locations such as Central America, Peru, the Arabian Sea, and the Bay of Bengal with fewer MCSs. Most MCSs over central America and Peru are smaller and short-lived. However, MCSs over the Arabian Sea and the Bay of Bengal are larger and longer-lived.

This study demonstrates that tracking is complex and that there are no perfect choices for FiT tracking parameters; hence, we chose optimal values that performed reasonably well. The choice of tracking algorithm, tracking parameters, and MCS definition affects the quantitative statistics, but these qualitative conclusions will remain the same. In the

future, we plan to investigate some open questions from this study, such as the land-ocean differences in IMERG's maximum rain rates and propagation velocities over the western Pacific Ocean. We believe that the MCSs properties over various tropical regions are manifestations of the environment they initiate and grow, which can also change with time. Next, we also plan to compare MCSs properties over different tropical regions through diurnal and seasonal variability to provide more insights into their convective regimes.

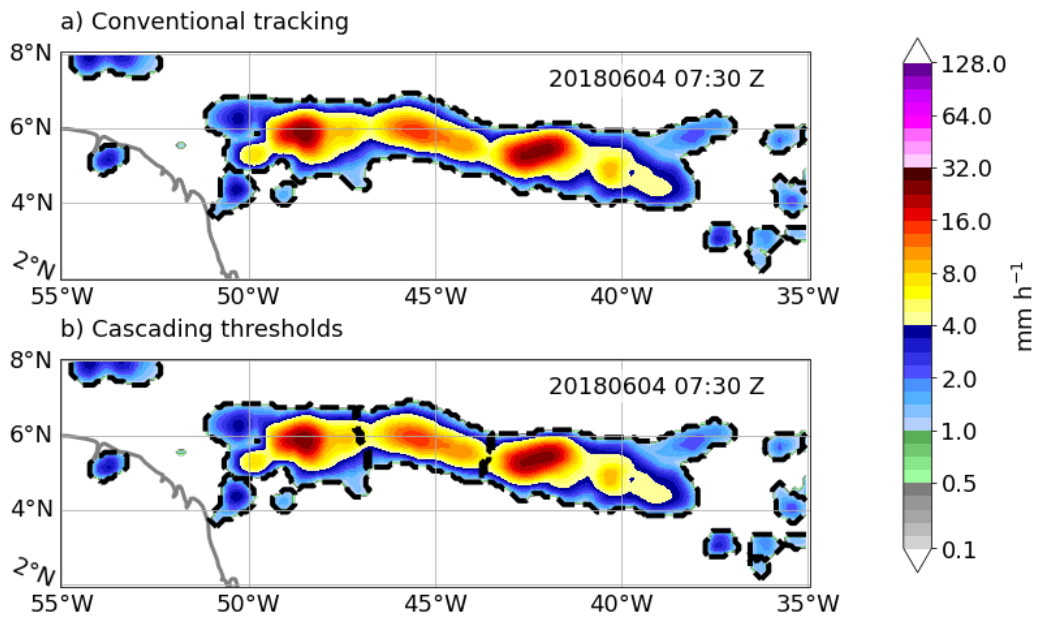


Fig. 3.1. A transient precipitation band was observed on 04 June 2018 at 07:30 UTC in IMERG. The band spans approximately 15° (~1660 km) of longitudinal width and has three or more identifiable mesoscale structures. The dashed contour represents tracked object boundary using a) single threshold, and b) cascading thresholds.

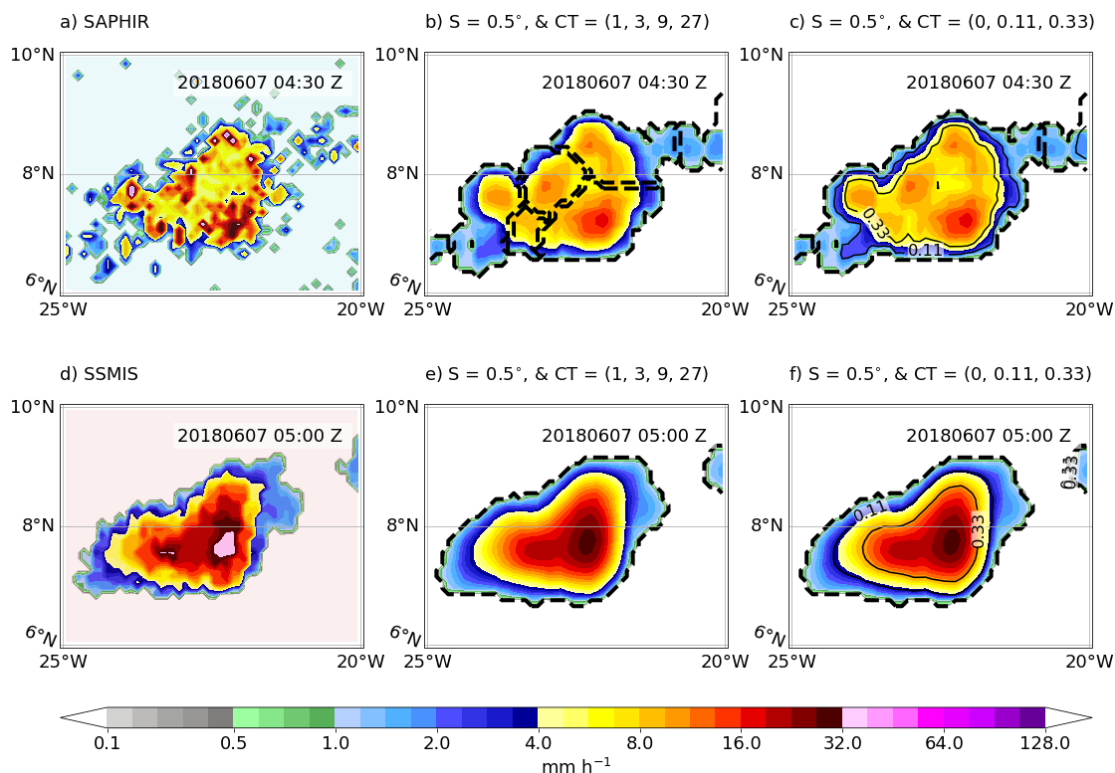


Fig. 3.2. PMW overpasses between subsequent half-hour periods on 07 June 2011, starting at 04:30 UTC and 05:00 UTC, observing an MCS in the tropical Atlantic Ocean. a) precipitation retrieval from Sounder for Probing Vertical Profiles of Humidity (SAPHIR) with a nominal resolution of ~ 10 km, b) applying a uniform smoothing filter of width $S = 0.5^\circ$, cascading thresholds, $CT = (1, 3, 9, 27)$ mm h^{-1} to SAPHIR precipitation; dashed contour represent objects identified by FiT program, c) normalized cascading threshold, $CT = (0, 0.11, 0.33)$, overlaid as solid contours; dashed contour represent objects identified by FiT program, d) precipitation retrieval from Special Sensor Microwave Imager/Sounder (SSMIS) with a nominal resolution of 55 km, e), and f) are same as b) and c) but for SSMIS overpass.

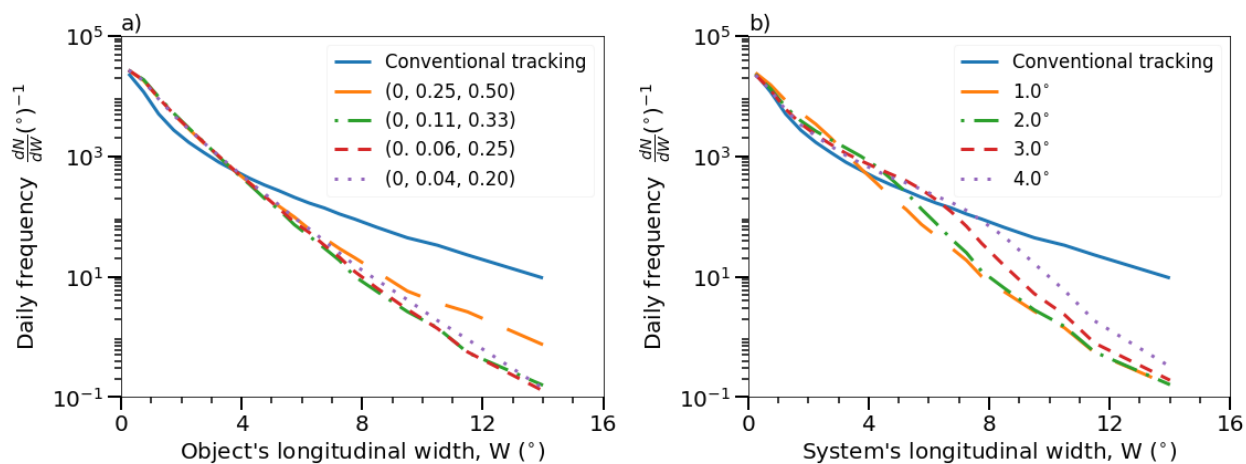


Fig. 3.3. Sensitivity tests for two major tracking parameters a) normalized cascading thresholds and b) separation distance. The identified object's size and system's size are expressed as longitudinal width, which is the difference between the easternmost and westernmost pixel longitude values.

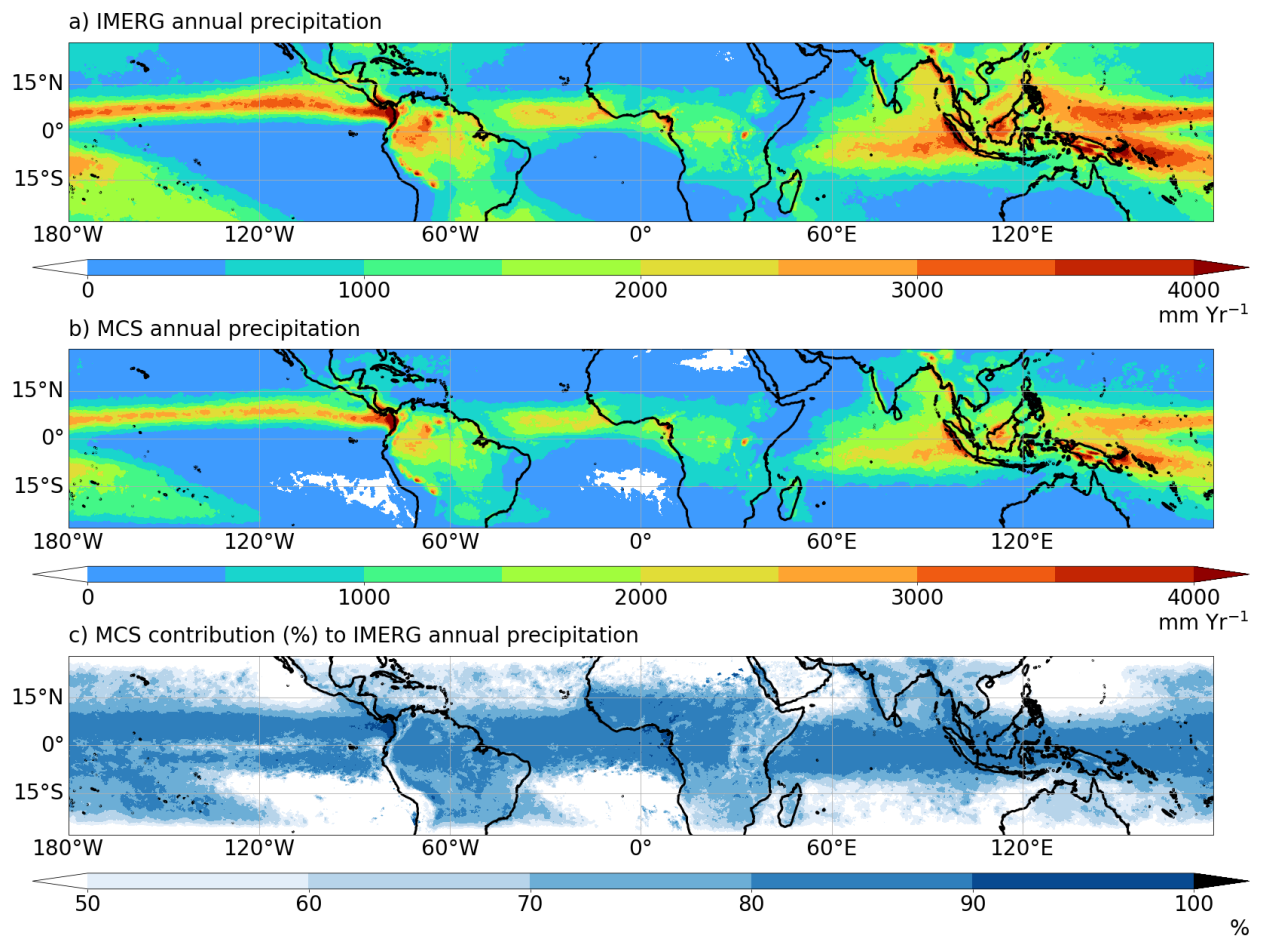


Fig. 3.4. Annual precipitation averaged over ten years (2011-2020) a) IMERG annual precipitation, b) MCS annual precipitation, and c) MCS contribution (%) as a ratio of values in panel b over panel a.

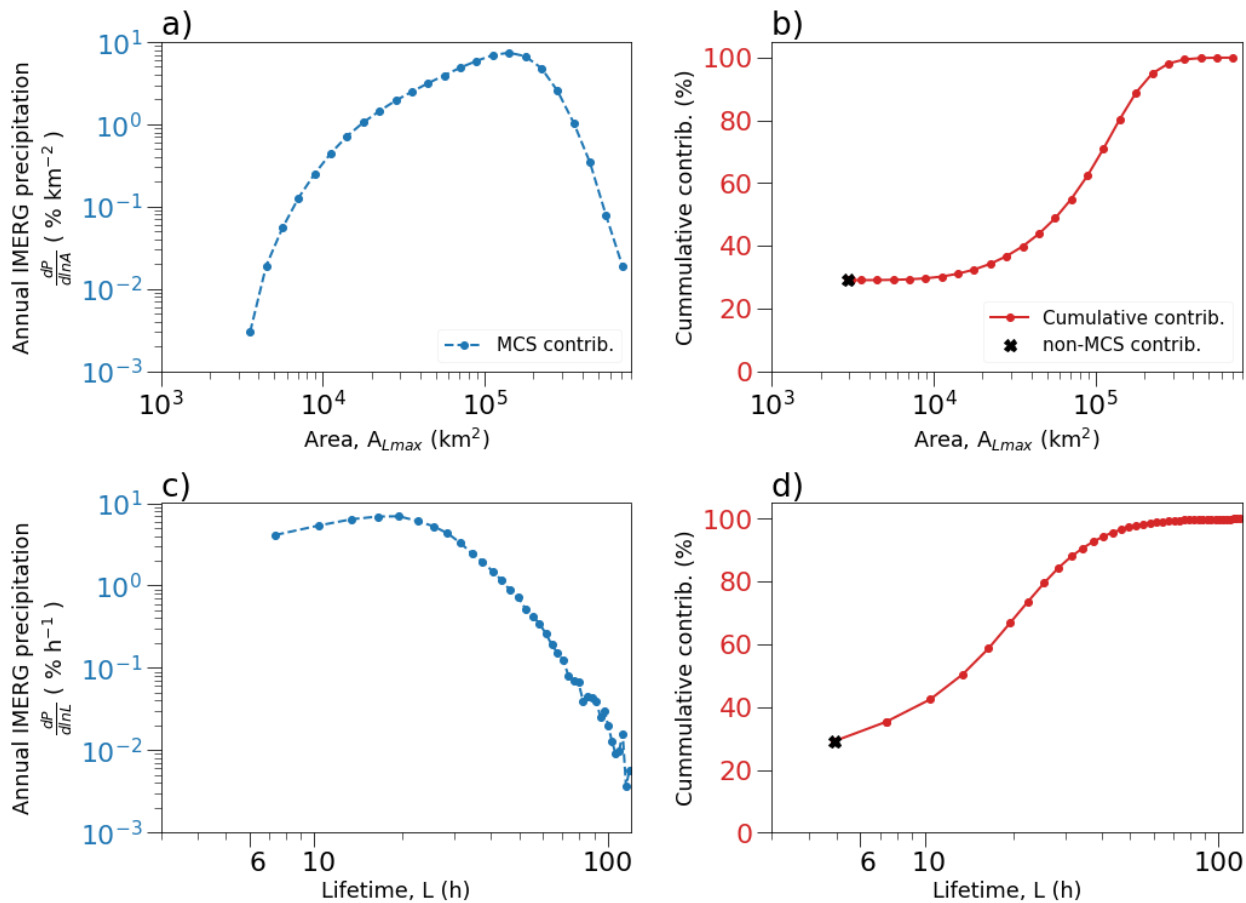


Fig. 3.5. MCSs annual rain contribution by their a) size, and b) lifetime. The non-MCS contribution is calculated as $(100 - \text{MCS contribution})$, which is approximately 30%.

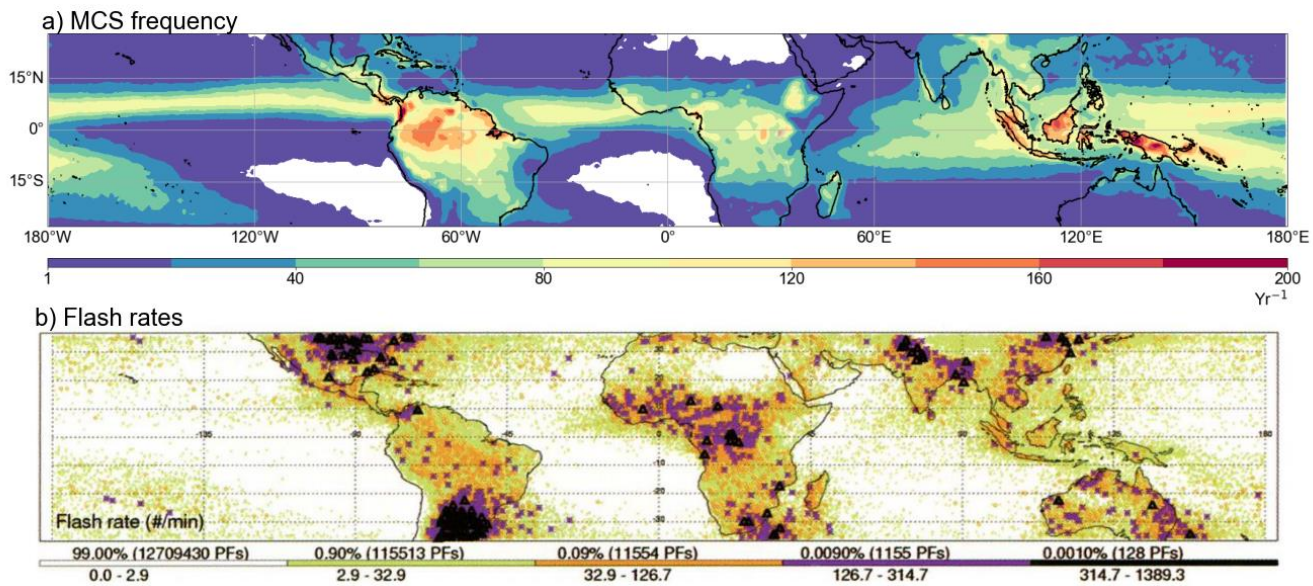


Fig. 3.6. a) Annual MCS frequency, and b) Lightning flash rates reproduced from Zipser et al., 2006.

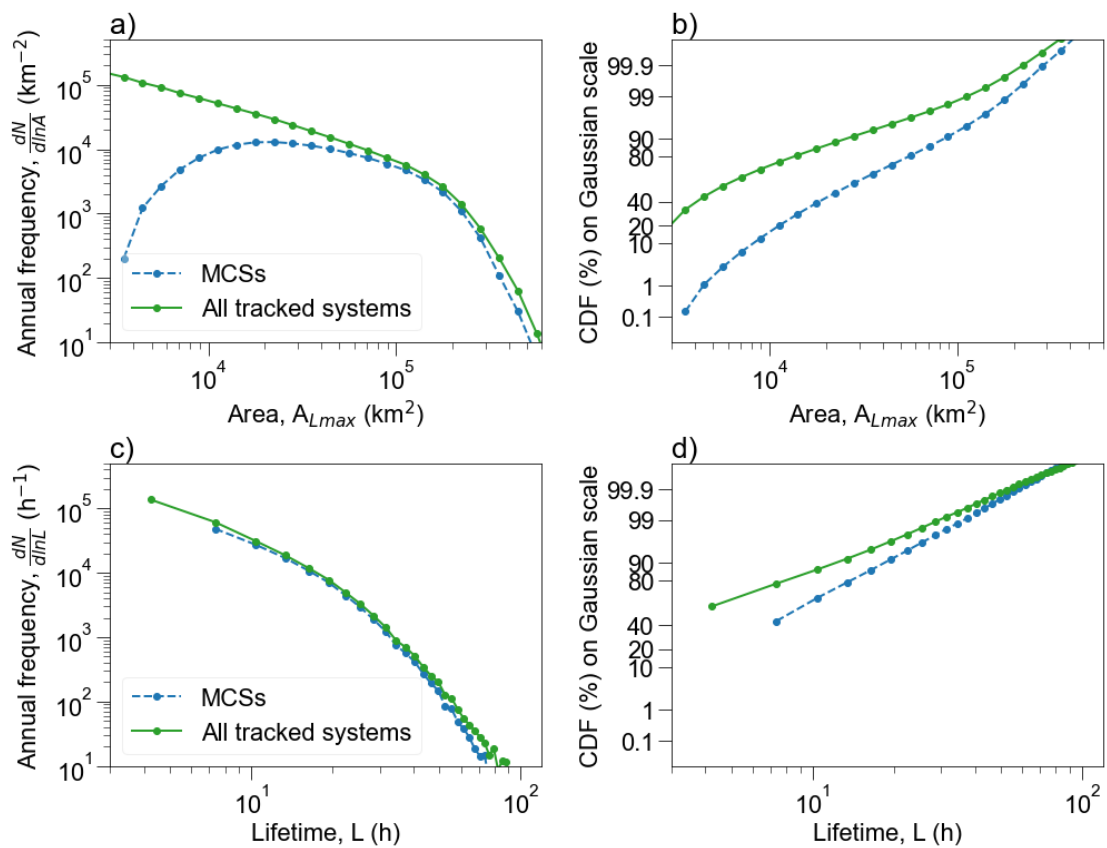


Fig 3.7. The frequency of MCSs and all tracked systems is expressed as a) probability distribution by maximum area (A_{Lmax}), b) cumulative distribution by maximum area (A_{Lmax}), and c) probability distribution by Lifetime (L), and d) Cumulative distribution of Lifetime (L).

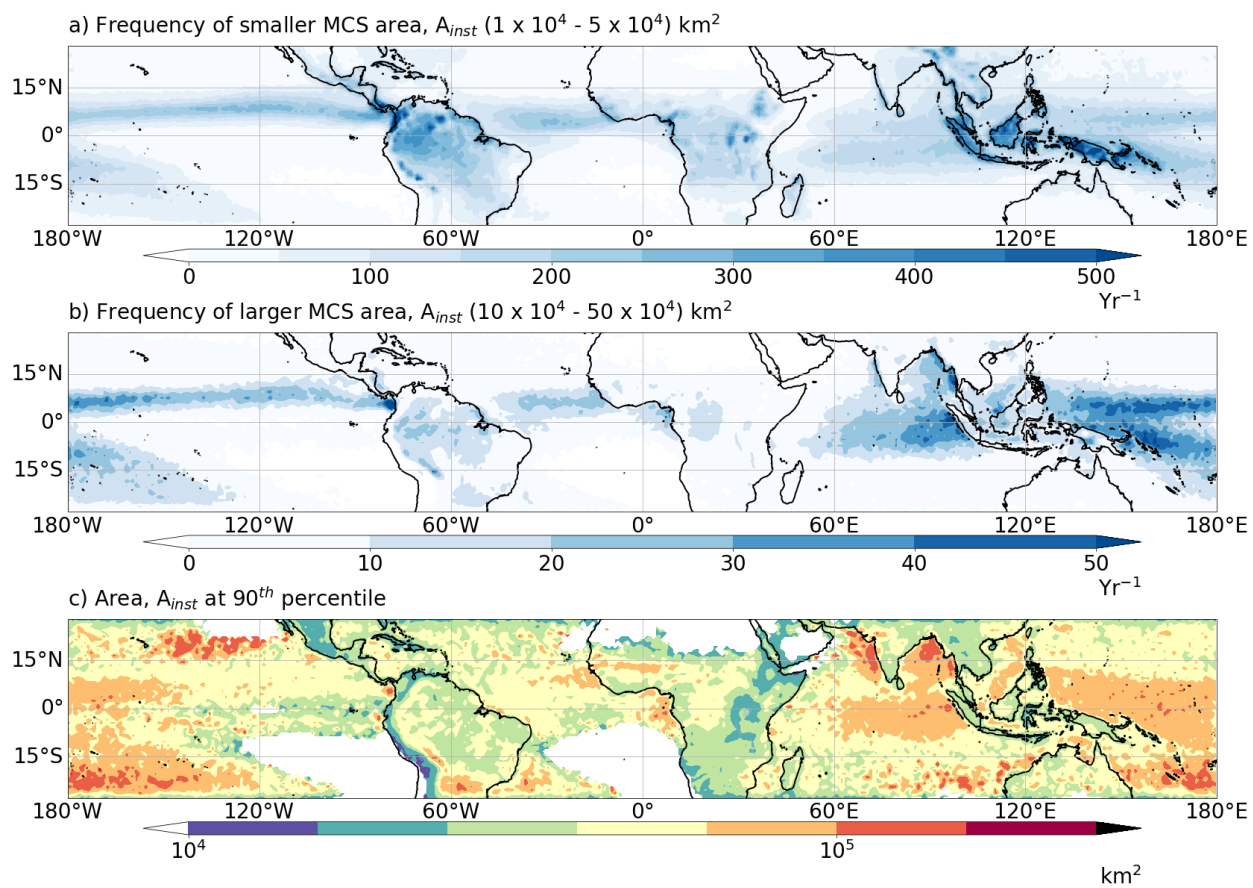


Fig 3.8. Spatial distribution of MCSs area a) annual frequency of small MCS areas, b) annual frequency of large MCS areas, c) 90th percentile of MCS areas

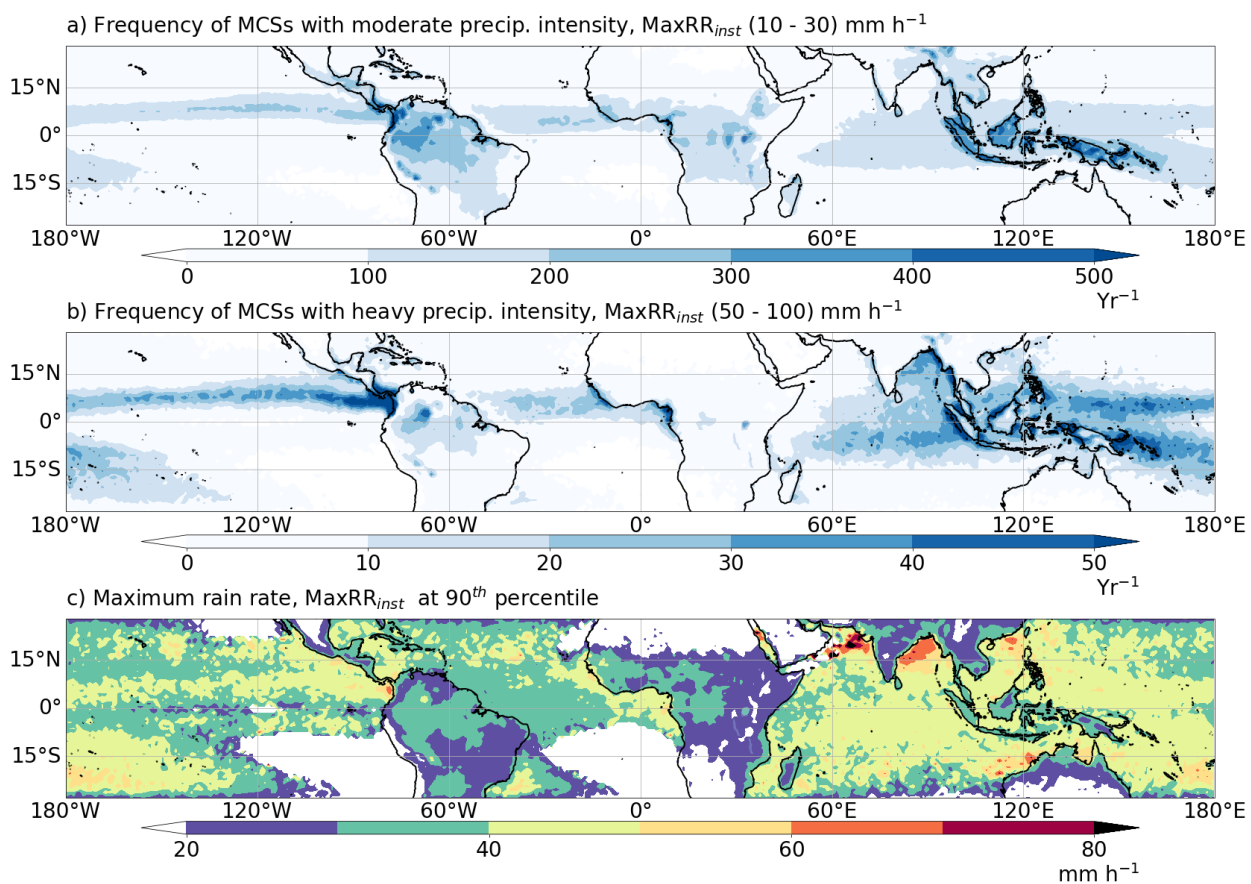


Fig 3.9. Spatial distribution of MCSs maximum rain rate a) annual frequency of MCS moderate precipitation intensities, b) annual frequency of MCS heavy precipitation intensities, c) 90th percentile of MCS maximum rain rates.

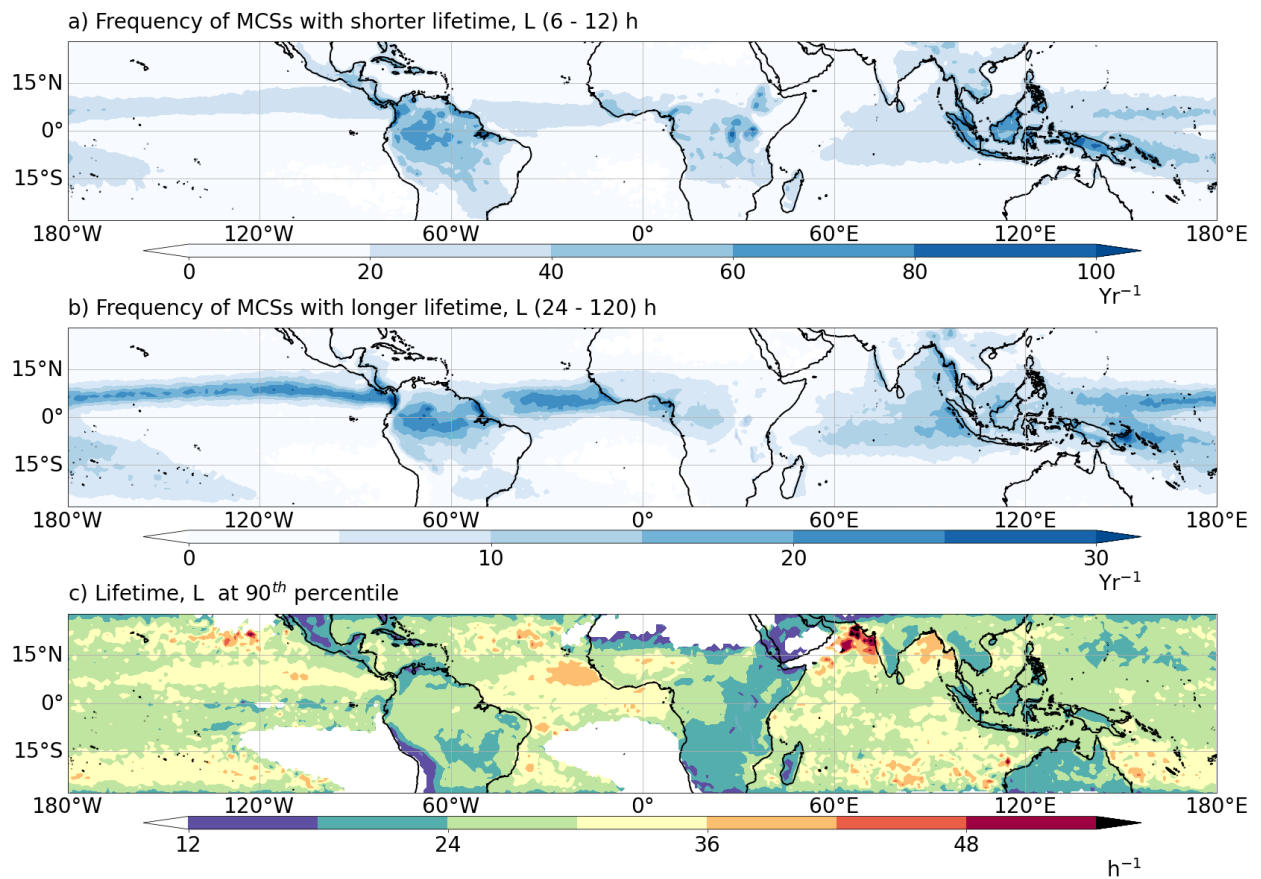


Fig 3.10. Spatial distribution of MCSs lifetime a) annual frequency of short-lived MCSs, b) annual frequency of long-lived MCSs, c) 90th percentile value of MCS lifetime.

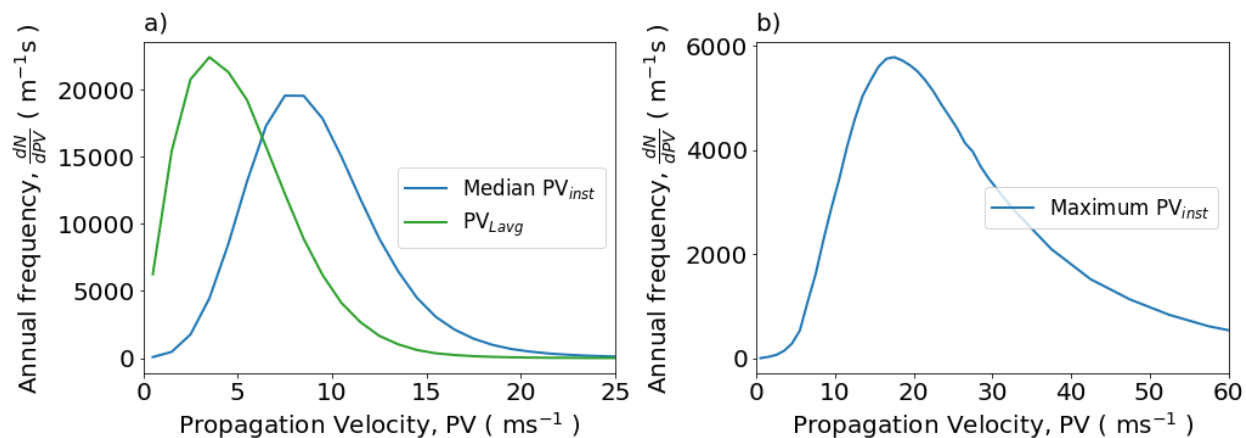


Fig. 3.11. a) Frequency distribution of median propagation velocity compared to average propagation velocity. Median propagation velocity is the median value of instantaneous velocities during an MCS lifetime. Average propagation velocity (PVL_{avg}) is computed between the start and end position of MCS's weighted centroid, b) Frequency distribution of maximum propagation velocity, which is calculated as the maximum of instantaneous velocities during an MCS lifetime.

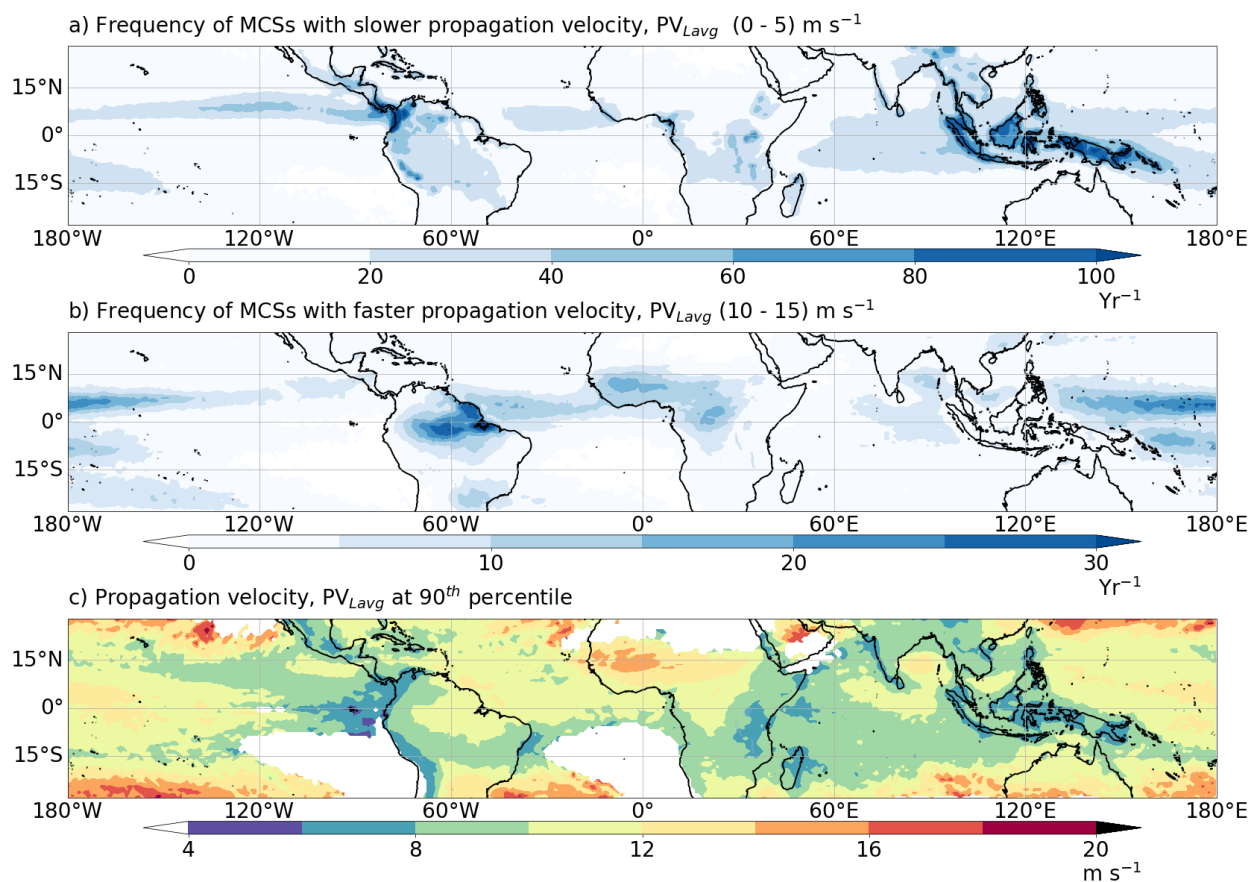


Fig 3.12. Spatial distribution of MCSs propagation velocity a) annual frequency of slow-moving MCSs, b) annual frequency of fast-moving MCSs, c) 90th percentile of MCS propagation velocity.

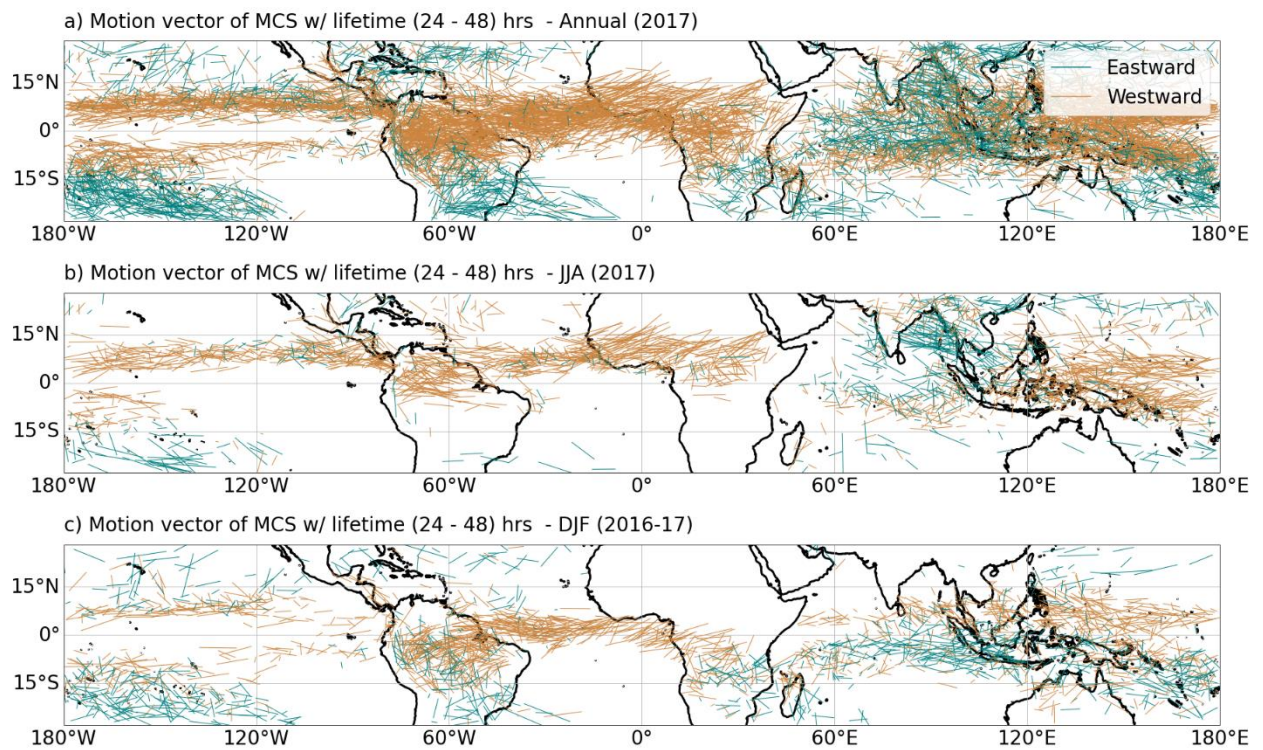


Fig 3.13. Spatial distribution of motions vector for MCSs with lifetime 24 – 48 hours a) Annual (2017), b) Boreal summer (June, July, August), 2017, c) Boreal winter (December, January, February), 2016-17.

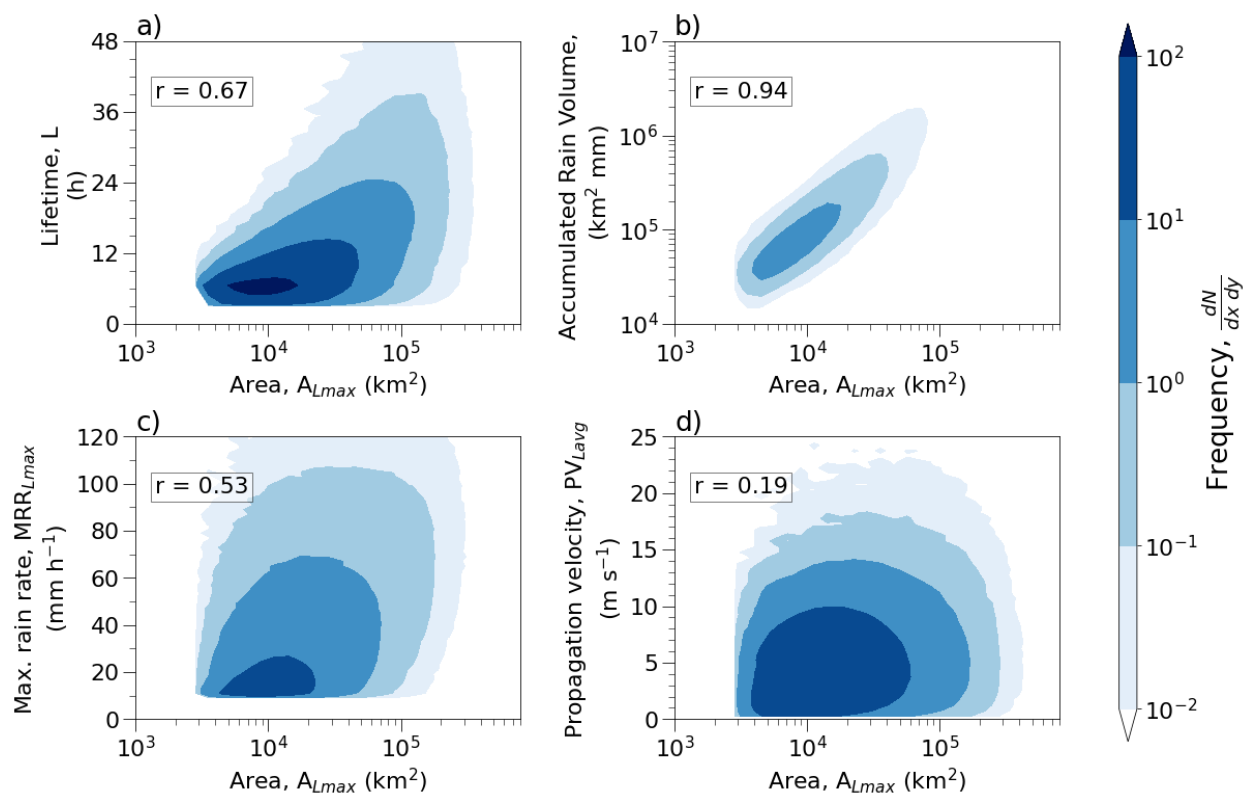


Fig. 3.14. Relationship between MCS properties: size vs. a) accumulated rain volume, b) maximum rain rate, c) lifetime and d) propagation velocity. The corresponding correlation value (r) is provided within each panel. The frequency is per unit quantity except for area and accumulated rain volume, for which the frequency is per 100 km^2 and $1000 \text{ km}^2 \text{ mm}$.

3.6 References

- Anselmo, E. M., Schumacher, C., & Machado, L. A. T. (2020). The amazonian low-level jet and its connection to convective cloud propagation and evolution. *Monthly Weather Review*, *148*(10), 4083–4099. <https://doi.org/10.1175/MWR-D-19-0414.1>
- Anselmo, E. M., Machado, L. A. T., Schumacher, C., & Kiladis, G. N. (2021). Amazonian mesoscale convective systems: Life cycle and propagation characteristics. *International Journal of Climatology*, *41*(7), 3968–3981. <https://doi.org/10.1002/joc.7053>
- Bang, S. D., & Zipser, E. J. (2016). Seeking reasons for the differences in size spectra of electrified storms over land and ocean. *Journal of Geophysical Research: Atmospheres*, *121*(15), 9048–9068. <https://doi.org/10.1002/2016JD025150>
- Benner, T. C., & Curry, J. A. (1998). Characteristics of small tropical cumulus clouds and their impact on the environment. *Journal of Geophysical Research Atmospheres*, *103*(D22), 28753–28767. <https://doi.org/10.1029/98JD02579>
- Berg, W., Kummerow, C., & Morales, C. A. (2002). Differences between East and West Pacific rainfall systems. *Journal of Climate*, *15*(24), 3659–3672. [https://doi.org/10.1175/1520-0442\(2002\)015<3659:DBEAWP>2.0.CO;2](https://doi.org/10.1175/1520-0442(2002)015<3659:DBEAWP>2.0.CO;2)
- Boer, E. R., & Ramanathan, V. (1997). Lagrangian approach for deriving cloud characteristics from satellite observations and its implications to cloud parameterization. *Journal of Geophysical Research Atmospheres*, *102*(17), 21383–21399. <https://doi.org/10.1029/97jd00930>
- Chen, S. S., & Houze, R. A. (1997). Diurnal variation and life-cycle of deep convective systems over the tropical Pacific warm pool. *Quarterly Journal of the Royal Meteorological Society*, *123*(538), 357–388. <https://doi.org/10.1256/smsqj.53805>
- Chen, S. S., Houze, R. A., & Mapes, B. E. (1996). Multiscale Variability of Deep Convection In Relation to Large-Scale Circulation in TOGA COARE. *Journal of the Atmospheric Sciences*, *53*(10), 1380–1409. [https://doi.org/10.1175/1520-0469\(1996\)053<1380:MVODCI>2.0.CO;2](https://doi.org/10.1175/1520-0469(1996)053<1380:MVODCI>2.0.CO;2)
- CHEN, S. S., & HOUZE JR, R. A. (1997). Diurnal variation and life-cycle of deep convective systems over the tropical Pacific warm pool. *Quarterly Journal of the Royal Meteorological Society*, *123*(538), 357–388. <https://doi.org/10.1256/smsqj.53805>
- Davis, C. A., Brown, B., & Bullock, R. (2006). Object-based verification of precipitation forecasts. Part I: Application to convective rain systems. *Monthly Weather Review*, *134*(7), 1785–1795. <https://doi.org/10.1175/MWR3146.1>

- Dorninger, M., Gilleland, E., Casati, B., Mittermaier, M. P., Ebert, E. E., Brown, B. G., & Wilson, L. J. (2018). The setup of the MesoVICT project. *Bulletin of the American Meteorological Society*, 99(9), 1887–1906. <https://doi.org/10.1175/BAMS-D-17-0164.1>
- Evans, J. L., & Shemo, R. E. (1996). A procedure for automated satellite-based identification and climatology development of various classes of organized convection. *Journal of Applied Meteorology*. [https://doi.org/10.1175/1520-0450\(1996\)035<0638:APFASB>2.0.CO;2](https://doi.org/10.1175/1520-0450(1996)035<0638:APFASB>2.0.CO;2)
- Feng, Z., Song, F., Sakaguchi, K., & Leung, L. R. (2020). Evaluation of Mesoscale Convective Systems in Climate Simulations: Methodological Development and Results from MPAS-CAM over the U.S. *Journal of Climate*, 1–62. <https://doi.org/10.1175/jcli-d-20-0136.1>
- Feng, Z., Leung, L. R., Liu, N., Wang, J., Houze, R. A., Li, J., et al. (2021a). A Global High-Resolution Mesoscale Convective System Database Using Satellite-Derived Cloud Tops, Surface Precipitation, and Tracking. *Journal of Geophysical Research: Atmospheres*, 126(8). <https://doi.org/10.1029/2020JD034202>
- Feng, Z., Leung, L. R., Liu, N., Wang, J., Houze, R. A., Li, J., et al. (2021b). A Global High-Resolution Mesoscale Convective System Database Using Satellite-Derived Cloud Tops, Surface Precipitation, and Tracking. *Journal of Geophysical Research: Atmospheres*, 126(8). <https://doi.org/10.1029/2020JD034202>
- Fiolleau, T., & Roca, R. (2013). An Algorithm for the Detection and Tracking of Tropical Mesoscale Convective Systems Using Infrared Images From Geostationary Satellite. *IEEE Transactions on Geoscience and Remote Sensing*, 51(7), 4302–4315. <https://doi.org/10.1109/TGRS.2012.2227762>
- Futyan, J. M., & Del Genio, A. D. (2007). Deep convective system evolution over Africa and the tropical atlantic. *Journal of Climate*, 20(20), 5041–5060. <https://doi.org/10.1175/JCLI4297.1>
- Garstang, M., Massie, H. L., Halverson, J., Greco, S., & Scala, J. (1994). Amazon Coastal Squall Lines. Part I: Structure and Kinematics. *Monthly Weather Review*, 122(4), 608–622. [https://doi.org/10.1175/1520-0493\(1994\)122<0608:ACSLPI>2.0.CO;2](https://doi.org/10.1175/1520-0493(1994)122<0608:ACSLPI>2.0.CO;2)
- Greco, S., Swap, R., Garstang, M., Ulanski, S., Shipham, M., Harriss, R. C., et al. (1990). Rainfall and surface kinematic conditions over central Amazonia during ABLE 2B. *Journal of Geophysical Research*, 95(D10), 17001. <https://doi.org/10.1029/JD095iD10p17001>
- Hamada, A., Murayama, Y., & Takayabu, Y. N. (2014). Regional characteristics of extreme rainfall extracted from TRMM PR measurements. *Journal of Climate*,

- 27(21), 8151–8169. <https://doi.org/10.1175/JCLI-D-14-00107.1>
- Hartmann, D. L., Hendon, H. H., & Houze, R. A. (1984). Some Implications of the Mesoscale Circulations in Tropical Cloud Clusters for Large-Scale Dynamics and Climate. *Journal of the Atmospheric Sciences*, *41*(1), 113–121. [https://doi.org/10.1175/1520-0469\(1984\)041<0113:SIOTMC>2.0.CO;2](https://doi.org/10.1175/1520-0469(1984)041<0113:SIOTMC>2.0.CO;2)
- Hayden, L., Liu, C., & Liu, N. (2021). Properties of Mesoscale Convective Systems Throughout Their Lifetimes Using IMERG, GPM, WLLN, and a Simplified Tracking Algorithm. *Journal of Geophysical Research: Atmospheres*, *126*(20), 1–21. <https://doi.org/10.1029/2021JD035264>
- Hodges, K. I., & Thorncroft, C. D. (1997a). Distribution and statistics of african mesoscale convective weather systems based on the ISCCP meteosat imagery. *Monthly Weather Review*, *125*(11), 2821–2837. [https://doi.org/10.1175/1520-0493\(1997\)125<2821:DASOAM>2.0.CO;2](https://doi.org/10.1175/1520-0493(1997)125<2821:DASOAM>2.0.CO;2)
- Hodges, K. I., & Thorncroft, C. D. (1997b). Distribution and Statistics of African Mesoscale Convective Weather Systems Based on the ISCCP Meteosat Imagery. *Monthly Weather Review*, *125*(11), 2821–2837. [https://doi.org/10.1175/1520-0493\(1997\)125<2821:DASOAM>2.0.CO;2](https://doi.org/10.1175/1520-0493(1997)125<2821:DASOAM>2.0.CO;2)
- Houze, Jr., R. A. (1982). Cloud Clusters and Large-Scale Vertical Motions in the Tropics. *Journal of the Meteorological Society of Japan. Ser. II*, *60*(1), 396–410. https://doi.org/10.2151/jmsj1965.60.1_396
- Houze Jr, R. a. (2004). Mesoscale Convective Systems-Review paper. *Reviews of Geophysics*, *42*, 1–43. <https://doi.org/10.1029/2004RG000150.1.INTRODUCTION>
- Houze, R. A. (1989). Observed structure of mesoscale convective systems and implications for large-scale heating. *Quarterly Journal of the Royal Meteorological Society*, *115*(487), 425–461. <https://doi.org/10.1002/qj.49711548702>
- Houze, R. A. (2004). *Mesoscale convective systems-Chapter. Rev. Geophys.* (Vol. 42). <https://doi.org/10.1029/2004RG000150>
- Houze, R. A., & Betts, A. K. (1981). Convection in GATE. *Reviews of Geophysics*, *19*(4), 541. <https://doi.org/10.1029/RG019i004p00541>
- Houze, R. A., & Cheng, C.-P. (1977). Radar Characteristics of Tropical Convection Observed During GATE: Mean Properties and Trends Over the Summer Season. *Monthly Weather Review*, *105*(8), 964–980. [https://doi.org/10.1175/1520-0493\(1977\)105<0964:RCOTCO>2.0.CO;2](https://doi.org/10.1175/1520-0493(1977)105<0964:RCOTCO>2.0.CO;2)
- Houze, R. A., Geotis, S. G., Marks, F. D., & West, A. K. (1981). Winter Monsoon

- Convection in the Vicinity of North Borneo. Part I: Structure and Time Variation of the Clouds and Precipitation. *Monthly Weather Review*, 109(8), 1595–1614. [https://doi.org/10.1175/1520-0493\(1981\)109<1595:WMCITV>2.0.CO;2](https://doi.org/10.1175/1520-0493(1981)109<1595:WMCITV>2.0.CO;2)
- Houze, R. A., Rasmussen, K. L., Zuluaga, M. D., & Brodzik, S. R. (2015a). The variable nature of convection in the tropics and subtropics: A legacy of 16 years of the Tropical Rainfall Measuring Mission satellite. *Reviews of Geophysics*, 53(3), 994–1021. <https://doi.org/10.1002/2015RG000488>
- Houze, R. A., Rasmussen, K. L., Zuluaga, M. D., & Brodzik, S. R. (2015b). The variable nature of convection in the tropics and subtropics: A legacy of 16 years of the Tropical Rainfall Measuring Mission satellite. *Reviews of Geophysics*, 53(3), 994–1021. <https://doi.org/10.1002/2015RG000488>
- Huang, X., Hu, C., Huang, X., Chu, Y., Tseng, Y. heng, Zhang, G. J., & Lin, Y. (2018). A long-term tropical mesoscale convective systems dataset based on a novel objective automatic tracking algorithm. *Climate Dynamics*, 51(7–8), 3145–3159. <https://doi.org/10.1007/s00382-018-4071-0>
- Huffman, G. J., Adler, R. F., Bolvin, D. T., Gu, G., Nelkin, E. J., Bowman, K. P., et al. (2007). The TRMM Multisatellite Precipitation Analysis (TMPA): Quasi-global, multiyear, combined-sensor precipitation estimates at fine scales. *Journal of Hydrometeorology*, 8(1), 38–55. <https://doi.org/10.1175/JHM560.1>
- Janiga, M. A., & Thorncroft, C. D. (2016). The influence of African easterly waves on convection over tropical Africa and the east Atlantic. *Monthly Weather Review*, 144(1), 171–192. <https://doi.org/10.1175/MWR-D-14-00419.1>
- Jiang, H., Feingold, G., Jonsson, H. H., Lu, M. L., Chuang, P. Y., Flagan, R. C., & Seinfeld, J. H. (2008). Statistical comparison of properties of simulated and observed cumulus clouds in the vicinity of Houston during the Gulf of Mexico Atmospheric Composition and Climate Study (GoMACCS). *Journal of Geophysical Research Atmospheres*, 113(13), 1–18. <https://doi.org/10.1029/2007JD009304>
- Kingsmill, D. E., & Houze Jr, R. a. (1999). Kinematic characteristics of air flowing into and out of precipitating convection over the west Pacific warm pool: An airborne Doppler radar survey. *Quarterly Journal of the Royal Meteorological Society*, 125(556), 1165–1207. <https://doi.org/10.1256/smsqj.55604>
- Knapp, K. R., Kruk, M. C., Levinson, D. H., Diamond, H. J., & Neumann, C. J. (2010). The international best track archive for climate stewardship (IBTrACS). *Bulletin of the American Meteorological Society*, 91(3), 363–376. <https://doi.org/10.1175/2009BAMS2755.1>
- Krishnamurti, T. N., Kanamitsu, M., Koss, W. J., & Lee, J. D. (1973). Tropical East–

- West Circulations During the Northern Winter. *Journal of the Atmospheric Sciences*, 30(5), 780–787. [https://doi.org/10.1175/1520-0469\(1973\)030<0780:TECDTN>2.0.CO;2](https://doi.org/10.1175/1520-0469(1973)030<0780:TECDTN>2.0.CO;2)
- Kummerow, C. D., Randel, D. L., Kulie, M., Wang, N. Y., Ferraro, R., Joseph Munchak, S., & Petkovic, V. (2015). The evolution of the goddard profiling algorithm to a fully parametric scheme. *Journal of Atmospheric and Oceanic Technology*, 32(12), 2265–2280. <https://doi.org/10.1175/JTECH-D-15-0039.1>
- Laurent, H., Machado, L. A. T., Morales, C. A., & Durieux, L. (2002a). Characteristics of the Amazonian mesoscale convective systems observed from satellite and radar during the WETAMC/LBA experiment. *Journal of Geophysical Research: Atmospheres*, 107(20), LBA 21-1-LBA 21-17. <https://doi.org/10.1029/2001JD000337>
- Laurent, H., Machado, L. A. T., Morales, C. A., & Durieux, L. (2002b). Characteristics of the Amazonian mesoscale convective systems observed from satellite and radar during the WETAMC/LBA experiment. *Journal of Geophysical Research: Atmospheres*, 107(20), LBA 21-1-LBA 21-17. <https://doi.org/10.1029/2001JD000337>
- LeMone, M. A., Barnes, G. M., & Zipser, E. J. (1984). Momentum Flux by Lines of Cumulonimbus over the Tropical Oceans. *Journal of the Atmospheric Sciences*, 41(12), 1914–1932. [https://doi.org/10.1175/1520-0469\(1984\)041<1914:MFBLOC>2.0.CO;2](https://doi.org/10.1175/1520-0469(1984)041<1914:MFBLOC>2.0.CO;2)
- Liebmann, B., Kiladis, G. N., Carvalho, L. M. V., Jones, C., Vera, C. S., Bladé, I., & Allured, D. (2009). Origin of convectively coupled Kelvin waves over South America. *Journal of Climate*, 22(2), 300–315. <https://doi.org/10.1175/2008JCLI2340.1>
- Liu, C. (2011a). Rainfall Contributions from Precipitation Systems with Different Sizes, Convective Intensities, and Durations over the Tropics and Subtropics. *Journal of Hydrometeorology*, 12(3), 394–412. <https://doi.org/10.1175/2010JHM1320.1>
- Liu, C. (2011b). Rainfall Contributions from Precipitation Systems with Different Sizes, Convective Intensities, and Durations over the Tropics and Subtropics. *Journal of Hydrometeorology*, 12(3), 394–412. <https://doi.org/10.1175/2010JHM1320.1>
- Liu, C., & Zipser, E. (2013). Regional variation of morphology of organized convection in the tropics and subtropics. *Journal of Geophysical Research Atmospheres*, 118(2), 453–466. <https://doi.org/10.1029/2012JD018409>
- Liu, C., Zipser, E. J., & Nesbitt, S. W. (2007). Global distribution of tropical deep convection: Different perspectives from TRMM infrared and radar data. *Journal of Climate*, 20(3), 489–503. <https://doi.org/10.1175/JCLI4023.1>

- Liu, C., Zipser, E. J., Cecil, D. J., Nesbitt, S. W., & Sherwood, S. (2008a). A cloud and precipitation feature database from nine years of TRMM observations. *Journal of Applied Meteorology and Climatology*, *47*(10), 2712–2728. <https://doi.org/10.1175/2008JAMC1890.1>
- Liu, C., Zipser, E. J., Cecil, D. J., Nesbitt, S. W., & Sherwood, S. (2008b). A cloud and precipitation feature database from nine years of TRMM observations. *Journal of Applied Meteorology and Climatology*, *47*(10), 2712–2728. <https://doi.org/10.1175/2008JAMC1890.1>
- Lopez, R. E. (1977). The Lognormal Distribution and Cumulus Cloud Populations. *Monthly Weather Review*, *105*(7), 865–872. [https://doi.org/10.1175/1520-0493\(1977\)105<0865:TLDACC>2.0.CO;2](https://doi.org/10.1175/1520-0493(1977)105<0865:TLDACC>2.0.CO;2)
- López, R. E. (1977). The Lognormal Distribution and Cumulus Cloud Populations. *Monthly Weather Review*, *105*(7), 865–872. [https://doi.org/10.1175/1520-0493\(1977\)105<0865:TLDACC>2.0.CO;2](https://doi.org/10.1175/1520-0493(1977)105<0865:TLDACC>2.0.CO;2)
- Machado, L. A. T., Rossow, W. B., Guedes, R. L., & Walker, A. W. (1998). Life cycle variations of mesoscale convective systems over the Americas. *Monthly Weather Review*, *126*(6), 1630–1654. [https://doi.org/10.1175/1520-0493\(1998\)126<1630:LCVOMC>2.0.CO;2](https://doi.org/10.1175/1520-0493(1998)126<1630:LCVOMC>2.0.CO;2)
- Mapes, B. E., & Houze, R. A. (1993). Cloud Clusters and Superclusters over the Oceanic Warm Pool. *Monthly Weather Review*, *121*(5), 1398–1416. [https://doi.org/10.1175/1520-0493\(1993\)121<1398:CCASOT>2.0.CO;2](https://doi.org/10.1175/1520-0493(1993)121<1398:CCASOT>2.0.CO;2)
- Maranan, M., Fink, A. H., Knippertz, P., Francis, S. D., Akpo, A. B., Jegede, G., & Yorke, C. (2019). Interactions between convection and a moist vortex associated with an extreme rainfall event over southern West Africa. *Monthly Weather Review*, *147*(7), 2309–2328. <https://doi.org/10.1175/MWR-D-18-0396.1>
- Martin, D. W., & Schreiner, A. J. (1981). Characteristics of West African and East Atlantic Cloud Clusters: A Survey from GATE. *Monthly Weather Review*, *109*(8), 1671–1688. [https://doi.org/10.1175/1520-0493\(1981\)109<1671:COWAAE>2.0.CO;2](https://doi.org/10.1175/1520-0493(1981)109<1671:COWAAE>2.0.CO;2)
- Mathon, V., & Laurent, H. (2001). Life cycle of Sahelian mesoscale convective cloud systems. *Quarterly Journal of the Royal Meteorological Society*, *127*(572), 377–406. <https://doi.org/10.1256/smsqj.57207>
- Matthews, A. J., & Kiladis, G. N. (2000). A Model of Rossby Waves Linked to Submonthly Convection over the Eastern Tropical Pacific. *Journal of the Atmospheric Sciences*, *57*(23), 3785–3798. [https://doi.org/10.1175/1520-0469\(2000\)057<3785:AMORWL>2.0.CO;2](https://doi.org/10.1175/1520-0469(2000)057<3785:AMORWL>2.0.CO;2)

- Mesnard, F., & Sauvageot, H. (2003). Structural characteristics of rain fields. *Journal of Geophysical Research: Atmospheres*, *108*(13).
<https://doi.org/10.1029/2002jd002808>
- Molinari, J., Vollaro, D., Skubis, S., & Dickinson, M. (2000). Origins and mechanisms of eastern Pacific tropical cyclogenesis: A case study. *Monthly Weather Review*, *128*(1), 125–139. [https://doi.org/10.1175/1520-0493\(2000\)128<0125:OAMOEP>2.0.CO;2](https://doi.org/10.1175/1520-0493(2000)128<0125:OAMOEP>2.0.CO;2)
- Moseley, C., Berg, P., & Haerter, J. O. (2013). Probing the precipitation life cycle by iterative rain cell tracking. *Journal of Geophysical Research Atmospheres*, *118*(24), 13361–13370. <https://doi.org/10.1002/2013JD020868>
- Murakami, T. (1972). Equatorial Tropospheric Waves Induced by Diabatic Heat Sources. *Journal of the Atmospheric Sciences*, *29*(5), 827–836.
[https://doi.org/10.1175/1520-0469\(1972\)029<0827:ETWIBD>2.0.CO;2](https://doi.org/10.1175/1520-0469(1972)029<0827:ETWIBD>2.0.CO;2)
- Neggers, R. A. J., Jonker, H. J. J., & Siebesma, A. P. (2003). Size statistics of cumulus cloud populations in large-eddy simulations. *Journal of the Atmospheric Sciences*, *60*(8), 1060–1074. [https://doi.org/10.1175/1520-0469\(2003\)60<1060:SSOCCP>2.0.CO;2](https://doi.org/10.1175/1520-0469(2003)60<1060:SSOCCP>2.0.CO;2)
- Nesbitt, S. W., & Zipser, E. J. (2000). A census of precipitation features in the tropics using TRMM: Radar, ice scattering, and lightning observations. *Journal of Climate*, *13*(23), 4087–4106. [https://doi.org/10.1175/1520-0442\(2000\)013<4087:ACOPFI>2.0.CO;2](https://doi.org/10.1175/1520-0442(2000)013<4087:ACOPFI>2.0.CO;2)
- Nesbitt, Stephen W., & Zipser, E. J. (2003). The diurnal cycle of rainfall and convective intensity according to three years of TRMM measurements. *Journal of Climate*, *16*(10), 1456–1475. <https://doi.org/10.1175/1520-0442-16.10.1456>
- Nesbitt, Stephen W., Cifelli, R., & Rutledge, S. A. (2006a). Storm morphology and rainfall characteristics of TRMM precipitation features. *Monthly Weather Review*, *134*(10), 2702–2721. <https://doi.org/10.1175/MWR3200.1>
- Nesbitt, Stephen W., Cifelli, R., & Rutledge, S. A. (2006b). Storm morphology and rainfall characteristics of TRMM precipitation features. *Monthly Weather Review*, *134*(10), 2702–2721. <https://doi.org/10.1175/MWR3200.1>
- Núñez Ocasio, K. M., Evans, J. L., & Young, G. S. (2020). Tracking Mesoscale Convective Systems that are Potential Candidates for Tropical Cyclogenesis. *Monthly Weather Review*, *148*(2), 655–669. <https://doi.org/10.1175/MWR-D-19-0070.1>
- Poveda, G., Espinoza, J. C., Zuluaga, M. D., Solman, S. A., Garreaud, R., & van Oevelen, P. J. (2020). High Impact Weather Events in the Andes. *Frontiers in*

- Earth Science*, 8(May), 1–32. <https://doi.org/10.3389/feart.2020.00162>
- Provod, M., Marsham, J. H., Parker, D. J., & Birch, C. E. (2016). A characterization of cold pools in the West African Sahel. *Monthly Weather Review*, 144(5), 1923–1934. <https://doi.org/10.1175/MWR-D-15-0023.1>
- Rajagopal, M., Zipser, E., Huffman, G., Russell, J., & Tan, J. (2021). Comparisons of IMERG Version 06 Precipitation At and Between Passive Microwave Overpasses in the Tropics. *Journal of Hydrometeorology*, 2117–2130. <https://doi.org/10.1175/jhm-d-20-0226.1>
- Ramage, C. S. (1968). ROLE OF A TROPICAL “MARITIME CONTINENT” IN THE ATMOSPHERIC CIRCULATION 1. *Monthly Weather Review*, 96(6), 365–370. [https://doi.org/10.1175/1520-0493\(1968\)096<0365:ROATMC>2.0.CO;2](https://doi.org/10.1175/1520-0493(1968)096<0365:ROATMC>2.0.CO;2)
- Rasmussen, K. L., Chaplin, M. M., Zuluaga, M. D., & Houze, R. A. (2016). Contribution of extreme convective storms to rainfall in South America. *Journal of Hydrometeorology*, 17(1), 353–367. <https://doi.org/10.1175/JHM-D-15-0067.1>
- Riehl, H., & Malkus, J. S. (1958). On the heat balance in the Equatorial trough zone. *Geophysica*, 6(3–4), 503–538. Retrieved from <http://scholar.google.com/scholar?hl=en&btnG=Search&q=intitle:On+the+heat+balance+in+the+Equatorial+trough+zone#0>
- Russell, J., Rajagopal, M., Veals, P., Skok, G., Zipser, E & Tinoco-Morales, M. (2022). A Dataset of Tracked Mesoscale Precipitation Systems in the Tropics. *Geoscience Data Journal*. in preparation
- Rydbeck, A. V., & Maloney, E. D. (2015). On the convective coupling and moisture organization of East Pacific easterly waves. *Journal of the Atmospheric Sciences*, 72(10), 3850–3870. <https://doi.org/10.1175/JAS-D-15-0056.1>
- Schumacher, C., & Houze, R. A. (2003). Stratiform rain in the tropics as seen by the TRMM precipitation radar. *Journal of Climate*, 16(11), 1739–1756. [https://doi.org/10.1175/1520-0442\(2003\)016<1739:SRITTA>2.0.CO;2](https://doi.org/10.1175/1520-0442(2003)016<1739:SRITTA>2.0.CO;2)
- Schumacher, C., Houze, R. A., & Kraucunas, I. (2004). The tropical dynamical response to latent heating estimates derived from the TRMM precipitation radar. *Journal of the Atmospheric Sciences*, 61(12), 1341–1358. [https://doi.org/10.1175/1520-0469\(2004\)061<1341:TTDRTL>2.0.CO;2](https://doi.org/10.1175/1520-0469(2004)061<1341:TTDRTL>2.0.CO;2)
- Silva Dias, M. A. F., Rutledge, S., Kabat, P., Silva Dias, P. L., Nobre, C., Fisch, G., et al. (2002). Cloud and rain processes in a biosphere-atmosphere interaction context in the Amazon Region. *Journal of Geophysical Research Atmospheres*, 107(20). <https://doi.org/10.1029/2001JD000335>
- Skok, G., Tribbia, J., Rakovec, J., & Brown, B. (2009a). Object-based analysis of

- satellite-derived precipitation systems over the low- and mid-latitude Pacific Ocean. *Monthly Weather Review*, *137*(10), 3196–3218.
<https://doi.org/10.1175/2009MWR2900.1>
- Skok, G., Tribbia, J., Rakovec, J., & Brown, B. (2009b). Object-Based Analysis of Satellite-Derived Precipitation Systems over the Low- and Midlatitude Pacific Ocean. *Monthly Weather Review*, *137*(10), 3196–3218.
<https://doi.org/10.1175/2009mwr2900.1>
- Skok, G., Tribbia, J., & Rakovec, J. (2010). Object-based analysis and verification of WRF model precipitation in the low- and midlatitude Pacific Ocean. *Monthly Weather Review*, *138*(12), 4561–4575. <https://doi.org/10.1175/2010MWR3472.1>
- Skok, G., Bacmeister, J., & Tribbia, J. (2013). Analysis of Tropical Cyclone Precipitation Using an Object-Based Algorithm. *Journal of Climate*, *26*(8), 2563–2579.
<https://doi.org/10.1175/JCLI-D-12-00135.1>
- Tan, J., Petersen, W. A., Kirstetter, P. E., & Tian, Y. (2017). Performance of IMERG as a function of spatiotemporal scale. *Journal of Hydrometeorology*, *18*(2), 307–319.
<https://doi.org/10.1175/JHM-D-16-0174.1>
- Tan, J., Huffman, G. J., Bolvin, D. T., Nelkin, E. J., & Rajagopal, M. (2020). SHARPEN: A Scheme to Restore the Distribution of Averaged Precipitation Fields. *Journal of Hydrometeorology*, 2105–2117. <https://doi.org/10.1175/jhm-d-20-0225.1>
- Tang, S., Xie, S., Zhang, Y., Zhang, M., Schumacher, C., Upton, H., et al. (2016). Large-scale vertical velocity, diabatic heating and drying profiles associated with seasonal and diurnal variations of convective systems observed in the GoAmazon2014/5 experiment. *Atmospheric Chemistry and Physics*, *16*(22), 14249–14264. <https://doi.org/10.5194/acp-16-14249-2016>
- Virts, K. S., & Houze, R. A. (2015). Variation of lightning and convective rain fraction in mesoscale convective systems of the MJO. *Journal of the Atmospheric Sciences*, *72*(5), 1932–1944.pdf. <https://doi.org/10.1175/JAS-D-14-0201.1>
- Wang, T., & Tang, G. (2020). Spatial Variability and Linkage Between Extreme Convections and Extreme Precipitation Revealed by 22-Year Space-Borne Precipitation Radar Data. *Geophysical Research Letters*, *47*(12), 1–10.
<https://doi.org/10.1029/2020GL088437>
- White, R. H., Battisti, D. S., & Skok, G. (2017a). Tracking precipitation events in time and space in gridded observational data. *Geophysical Research Letters*, *44*(16), 8637–8646. <https://doi.org/10.1002/2017GL074011>
- White, R. H., Battisti, D. S., & Skok, G. (2017b). Tracking precipitation events in time and space in gridded observational data. *Geophysical Research Letters*, *44*(16),

- 8637–8646. <https://doi.org/10.1002/2017GL074011>
- Wielicki, B. A., & Welch, R. M. (1986). Cumulus Cloud Properties Derived Using Landsat Satellite Data. *Journal of Climate and Applied Meteorology*, 25(3), 261–276. [https://doi.org/10.1175/1520-0450\(1986\)025<0261:CCPDUL>2.0.CO;2](https://doi.org/10.1175/1520-0450(1986)025<0261:CCPDUL>2.0.CO;2)
- Williams, M., Houze, R. (1987). Satellite-Observed Characteristics of Winter Monsoon Cloud Clusters. *Monthly Weather Review*, 5(1), 1–8. [https://doi.org/https://doi.org/10.1175/1520-0493\(1987\)115<0505:SOCOWM>2.0.CO;2](https://doi.org/https://doi.org/10.1175/1520-0493(1987)115<0505:SOCOWM>2.0.CO;2)
- Williams, M., & Houze, R. A. (1987). Satellite-observed characteristics of winter monsoon cloud clusters. *Monthly Weather Review*. [https://doi.org/10.1175/1520-0493\(1987\)115<0505:SOCOWM>2.0.CO;2](https://doi.org/10.1175/1520-0493(1987)115<0505:SOCOWM>2.0.CO;2)
- Woodley, W. L., Griffith, C. G., Griffin, J. S., & Stromatt, S. C. (1980). The Inference of GATE Convective Rainfall from SMS-1 Imagery. *Journal of Applied Meteorology*, 19(4), 388–408. [https://doi.org/10.1175/1520-0450\(1980\)019<0388:TIOGCR>2.0.CO;2](https://doi.org/10.1175/1520-0450(1980)019<0388:TIOGCR>2.0.CO;2)
- You, Y., Petkovic, V., Tan, J., Kroodsmas, R., Berg, W., Kidd, C., & Peters-Lidard, C. (2020). Evaluation of V05 Precipitation Estimates from GPM Constellation Radiometers Using KuPR as the Reference. *Journal of Hydrometeorology*. <https://doi.org/10.1175/JHM-D-19-0144.1>
- Zipser, E. J. (1977). Mesoscale and Convective–Scale Downdrafts as Distinct Components of Squall-Line Structure. *Monthly Weather Review*, 105(12), 1568–1589. [https://doi.org/10.1175/1520-0493\(1977\)105<1568:MACDAD>2.0.CO;2](https://doi.org/10.1175/1520-0493(1977)105<1568:MACDAD>2.0.CO;2)
- Zipser, E. J., Cecil, D. J., Liu, C., Nesbitt, S. W., & Yorty, D. P. (2006). WHERE ARE THE MOST INTENSE THUNDERSTORMS ON EARTH? *Bulletin of the American Meteorological Society*, 87(8), 1057–1072. <https://doi.org/10.1175/BAMS-87-8-1057>
- Zipser, Edward J. (2003). Some Views On “Hot Towers” after 50 Years of Tropical Field Programs and Two Years of TRMM Data. *Meteorological Monographs*, 29(51), 49–49. [https://doi.org/10.1175/0065-9401\(2003\)029<0049:CSVOHT>2.0.CO;2](https://doi.org/10.1175/0065-9401(2003)029<0049:CSVOHT>2.0.CO;2)
- Zipser, Edward J., & Liu, C. (2021). Extreme Convection vs. Extreme Rainfall: a Global View. *Current Climate Change Reports*, 7(4), 121–130. <https://doi.org/10.1007/s40641-021-00176-0>

CHAPTER 4

DIURNAL CYCLE TRANSITION FROM COAST TO OPEN OCEAN AND INLAND REGIONS.

4.1 Abstract

The global land and ocean have diurnal cycles of precipitation that are out of phase. Overland, the maximum precipitation typically occurs in the evening, whereas over the ocean, it is typically in the early morning. During the Global Atmospheric Research Program's Atlantic Tropical Experiment (GATE), the maximum precipitation occurred in the afternoon over the eastern Atlantic. We hypothesize that this afternoon maximum is likely from the influence of nearby land. Therefore, We use the Integrated Multi-satellite Retrieval for Global Precipitation Mission (IMERG) precipitation and Tracked IMERG Mesoscale Precipitation Systems (TIMPS) dataset to examine the diurnal cycle transition from coast to open ocean and inland regions. First, we analyze the diurnal cycle transition over three study regions and then over the global tropics.

We find that the early morning maximum over open oceans is from the enhancement of the existing convection since the TIMPS frequency has a local minimum in the early morning. The afternoon maximum observed over the eastern Atlantic and the eastern Pacific is due to increased MCSs frequency and enhanced precipitation, possibly from a merger of MCSs that intensifies the convection. On a spatial plot, the time of maximum precipitation gradually changes from early morning near offshore to afternoon

over the ocean areas, ~1000 from the coastline. This gradual change hints at the presence of propagating disturbance, possibly gravity waves. Over inland, sub-mesoscale, and small MCSs contribute significantly to creating an evening maximum, whereas large MCSs contribute significantly to creating an early morning maximum over the open ocean.

4.2 Introduction

Precipitation varies in space and time. The diurnal cycle of precipitation is one of the dominant modes of temporal variability influenced by the solar cycle. The land and ocean exhibit a different diurnal cycle for the same daily solar insolation. Past studies have shown that tropical land and ocean have maximum precipitation around 1600 and 0600 hours local solar time (LST), respectively (Dai, 2001; Yang & Slingo, 2001; Nesbitt & Zipser, 2003; Biasutti et al., 2012). The fidelity of numerical weather and climate models to capture the diurnal variability of precipitation is an important test. This is because precipitation results from many atmospheric processes, such as radiation, boundary layer, convection, and cloud physics (Covey et al., 2016; Aiguo Dai & Trenberth, 2004; Peatman et al., 2014). Over the land, the maximum precipitation is typically in the afternoon from the convection triggered by the diurnally forced circulations such as sea breeze, lake breeze, and upslope flows. However, in some land regions, the maximum precipitation is observed in the late evening or midnight, linked to the nocturnal Mesoscale Convective Systems (MCSs). Such nocturnal MCSs were observed over various regions: the continental USA (Wallace, 1975; Cotton et al., 1989; Tan et al., 2019), Northern Sahel (McGarry & Reed, 1978), and Amazon basin (Silva

Dias et al., 1987; Garstang et al., 1994; Anselmo et al., 2021).

Over the ocean, the maximum precipitation is typically observed in the early morning hours. This early morning peak is out-of-phase with the evening peak over land. One of the earliest proposed mechanisms to explain the early morning maximum is the Direct Radiation-Convection interaction (DRC). It suggested that the long wave (LW) radiative cooling from the cloud top and warming at the cloud base increases the convective circulation (Kraus, 1963; Houze, 1982; Dudhia, 1989; Randall et al., 1991). Kraus (1963) argued that short wave (SW) warming near the cloud top during the daytime suppresses this circulation, whereas nighttime cooling enhances the circulation leading to maximum precipitation in the early mornings. He also noted that SW warming is limited to a few hundred meters of the cloud top. Hence, its effect on weakening deep convective cell circulation during daytime is not observed (Yang and Smith 2006). However, the direct radiative processes play a crucial role within the stratiform/anvil cloud regions (Dudhia, 1989; Houze, 1982; Houze, 2004). These stratiform regions have their cloud base in the mid to upper troposphere, where LW radiative heating makes the cloud base warmer than the environment and destabilizes them. In contrast, the effect of LW radiative heating on deep convective cells with cloud base near boundary layer top is minimal (Dudhia, 1989). Though LW radiation-cloud interaction enhances the convective circulation in stratiform regions, the differences between daytime and nighttime convective circulation yet need to be quantified.

Another widely accepted mechanism is the dynamical effects of day vs. night differential tropospheric radiational cooling (DN-DTRC; Gray & Jacobson, 1977). At night, the absence of short wave absorption by atmospheric gases leads to increased

tropospheric cooling. This additional cooling increases the compensating subsidence from the existing convection into surrounding clear-air regions, thereby intensifying the surface convergence. The maximum precipitation is close to sunrise when the tropospheric temperature reaches a minimum. Other studies found that the surface convergence reached its maximum in the early mornings and its minimum in the late evenings (McBride and Gray, 1980; Sakaeda et al., 2018).

Chen and Houze (1997) commented that for DRC and DN-DTRC to work, the deep organized convection must already exist. They proposed that the early morning maximum is a consequence of the MCS lifecycle and mesoscale processes. The convection over the ocean initiates in the late afternoon, which then grows through the night producing maximum precipitation around the early morning. Later, the convection is weakened by the cold pool outflow and solar radiation blocked by the existing clouds. The new convection is triggered the following afternoon over the nearby cloud-free areas. This mechanism is similar to mesoscale processes responsible for the nighttime maximum over west Africa or the early morning maximum over the Amazon basin. The final theory proposes that the maximum precipitation in the early morning is due to the increased "available precipitable water" (APW) due to nighttime tropospheric cooling (Sui et al., 1997; Dai, 2001). The inflow and entrainment of cooler tropospheric air produce more condensation at lower cloud altitudes, increasing the precipitation efficiency and producing maximum precipitation. Although multiple mechanisms have been suggested to explain the early morning maximum, it could be a combination of these processes, as shown in a recent modeling study by Ruppert and Hohenegger (2018)

Early studies used infrared (IR) or space-borne precipitation radar (PR) satellite

data to investigate the diurnal variability of precipitation over the global tropics. Though IR satellite data is available at a high temporal resolution, the diurnal cycle is affected by choice of IR brightness temperature (T_b) thresholds. Mapes and Houze (1993) and Chen et al. (1997) noted that for cloud clusters defined as $T_b < 235$ K, the maximum cloud coverage occurred in the afternoon maximum, but for $T_b < 210$ K, the maximum occurred in the early mornings. Even for colder $T_b < 210$ K thresholds, Liu and Zipser (2008) found that over land, the IR cloud cover peaked two hours after the maximum surface precipitation was observed by the Tropical Rainfall Measuring Mission (TRMM) precipitation radar.

Though the maximum precipitation typically occurs in the early morning over oceans, an afternoon maximum was observed in the eastern Atlantic during the Global Atmospheric Research Program's Atlantic Tropical Experiment (GATE; McGarry and Reed, 1978; Houze and Betts, 1981). A similar afternoon maximum was also reported over the eastern South Pacific Convergence Zone (Albright et al., 1985). The afternoon maximum over the GATE domain was not peculiar to the program year (1974) but was also present in 1978 (Reed and Jaffe, 1981). The observations showing maximum precipitation during early morning and afternoon over different ocean regions are intriguing. The afternoon maximum observed over the GATE domain is close to land but far from being influenced by the land breeze. Rather than grouping locations as simply land and ocean, grouping them based on distances from the coastline may help understand these differences in the diurnal cycle over different oceanic regions.

Integrated Multi-satellite Retrieval for Global Precipitation Mission (IMERG) is NASA's global precipitation product available every 30 minutes. The finer temporal

resolution provides a more accurate diurnal cycle than its predecessor, TRMM Multi-satellite Precipitation Analysis (TMPA), available every three hours. The TRMM PR's surface precipitation is closer to surface observations and accurately represents the diurnal cycle. However, the IMERG precipitation and the related Tracked IMERG Mesoscale Precipitation Systems (TIMPS; Rajagopal et al., 2022; Russell et al., 2022) dataset will help understand the observed diurnal cycle in the context of convective system sizes, frequency, their initiation, and termination.

In this study, we examine the variability of the diurnal cycle from the coast to the open ocean and inland regions, including the early morning and afternoon maxima over specific ocean regions. We first analyze the regional transition of the diurnal cycle from coast to open oceans regionally; then, we examine the transition of the diurnal cycle globally, from coast to open ocean and inland regions, as a function of distance from the coastline. Finally, we discuss the possible mechanisms for the time of maximum precipitation over different land and ocean regions. The rest of the article is organized as follows: Section 2 discusses the IMERG product, TIMPS dataset, and the study regions; Section 3 describes the change in the diurnal cycle from regional onshore to open ocean, then globally from coast to open ocean and inland regions. Section 4 discusses the mechanism for the observed time of maximum precipitation, and a summary is presented in Section 5.

4.3 Data and Methods

We use the IMERG precipitation and TIMPS dataset to analyze the diurnal cycle transition from coast to open ocean and inland regions.

4.3.1 IMERG version 06B

The IMERG precipitation data is more beneficial for investigating the diurnal cycle since they are available every 30 minutes. The IMERG precipitation data is primarily based on passive microwave (PMW) observations from low earth orbit (LEO) satellites. In the absence of PMW observations over a location at the current analysis time, IMERG uses a time morphing scheme to estimate precipitation through a weighted average of advected PMW precipitation from past and future with Infrared (IR) precipitation (Huffman et al. 2020a, 2020b). IMERG uses the precipitation retrievals from the Goddard Profiling algorithm (GPROF) and Precipitation Retrieval and Profiling Scheme (PRPS) that convert the low and high-frequency PMW Tb values to precipitation estimates. The low-frequency PMW channels (also known as emission channels) detect the total column of liquid water, whereas the high-frequency channels (also known as scattering channels) detect the total column of ice water. Over the land, these algorithms use PMW Tb values from only ice-scattering channels, whereas both the emission and ice-scattering channels are used over the ocean.

This study uses the IMERG version 06B Final Run product, a research-quality dataset with more PMW observations and rain-gauge bias correction than other Runs (Early and Late Runs). The IMERG global precipitation data, available at Universal Coordinated Time (UTC), is converted to local solar time (LST) at each grid cell based on their longitude. The precipitation data are then grouped into hourly bins starting from 00 to 23 hours LST at each grid cell. We use the IMERG precipitation from 2011 to 2020 with corresponding tracked MCSs in the TIMPS dataset for our analysis.

4.3.2 *TIMPS dataset*

The IMERG's high spatial and temporal resolution makes it more suitable for tracking MCSs and studying their properties than other satellite products. The MCSs over the global tropics (30°N – 30°S) were tracked using the Forward in Time (FiT; Skok et al., 2009, 2013) algorithm in the IMERG precipitation field and stored in a publicly available database called Tracked IMERG Mesoscale Precipitation System (TIMPS; Russell et al., 2022) dataset. TIMPS is a subset of the tracked precipitation systems that satisfy our three MCS criteria: i) precipitation area $\geq 3000 \text{ km}^2$ at least once during its lifecycle, ii) lives for six hours or longer, and iii) precipitation intensity $\geq 10 \text{ mm h}^{-1}$ at least once during its lifetime somewhere within the system.

In the TIMPS dataset, MCS properties such as precipitation area, volumetric rain rate (rain volume), maximum precipitation rate, weighted centroid, and local solar time are stored for each timestep of an MCS lifecycle. The precipitation-weighted centroid, expressed in latitude and longitude, is the precipitation-weighted average of latitude and longitude of MCS pixels, respectively. We use the weighted centroid to determine if an MCS is located in our study regions. Though some of the MCS pixels might be outside the domain, statistically, they would still represent the study region. An MCS's volumetric rain rate is the sum of products of the pixel area and pixel rain rate of MCS pixels. An MCS's local solar time is computed from the weighted centroid's longitude and its UTC time.

4.3.3 *Study regions and seasons*

We select three study regions: i) Central America and Eastern Pacific, ii) West

Africa and Atlantic, and iii) Maritime Continent and eastern Indian Ocean (fig. 4.1) to examine the transition of the diurnal cycle from the coastal areas to the open oceans and possibly the presence of the afternoon maximum. We pick three boxes ($\sim 5^\circ \times 5^\circ$) in each region to represent coastal, transition, and open ocean areas (fig. 4.2). In the coastal box, land and ocean grid cells < 500 km from the coastline are classified as onshore and offshore, respectively. The GATE domain lies $\sim 700 - 1200$ km from the West African coastline. Therefore, we pick similar transition area boxes (E. Pac1, E. Atl, and E. IO1) approximately 700 to 1200 km from the coastal boxes. The open ocean boxes (E. Pac2, C. Atl, and E. IO2) are more than 1500 km from the coastal boxes.

In all three regions, the Inter-Tropical Convergence Zone (ITCZ) position shifts with the season; the shift is more significant over tropical land than the ocean. Fig. 4.1 and 4.2 show that the regional precipitation shifts between boreal summer (JJA) and winter (DJF). The seasonal precipitation is higher during boreal summer in central America, eastern Pacific, West Africa, and eastern Atlantic. However, seasonal precipitation over the Maritime continent is higher during boreal winter. Consequently, we investigate the diurnal cycle in these regions during the season with higher precipitation.

4.3.4 Diurnal cycle

Though ten years of data provide a large sample, the diurnal cycle over smaller areas ($\sim 5^\circ \times 5^\circ$) is still noisy. Therefore, we apply a three-hour running mean three times on the 24-hour diurnal cycle with data points wrapped at the ends. The diurnal cycle of different variables is presented as a percent of the daily mean value, similar to past

studies (Gray & Jacobson, 1977; Albright et al., 1985). The percentage helps compare the diurnal cycle amplitude and phase of various regions though they have different daily means.

4.4 Results

The following subsections describe the transition of the diurnal cycle from coast to open ocean and inland regions through the IMERG precipitation; TIMPS initiation, rain volume, and termination; and sub-mesoscale, small mesoscale, and large mesoscale system precipitation. First, we present the diurnal cycle of the above variables for three study regions and then for the global tropics. The IMERG precipitation includes both TIMPS and non-TIMPS precipitation. TIMPS represent the tracked precipitation systems that satisfy our MCS criteria but have sub-mesoscale size during their initial and final stages. Hence, we group the IMERG precipitation into three size categories: sub-mesoscale ($< 3000 \text{ km}^2$), small mesoscale ($3000 \text{ to } 10000 \text{ km}^2$), and large mesoscale ($50,000 - 100,000 \text{ km}^2$) sizes, to understand their relative contribution to the diurnal cycle.

4.4.1 IMERG vs. PR

The diurnal cycle of the IMERG precipitation, presented in fig. 4.3a shows that the maximum precipitation occurs around 1700 hours and 0600 hours over the land and ocean, respectively. The Islands of the Maritime continent and Central America have maximum precipitation at similar times as global land regions. This maximum precipitation occurs close to the late afternoon and must closely be tied to diurnally

forced circulation such as sea breeze and upslope flows (Yang and Smith, 2006; Biasutti et al., 2012). Over west Africa, the maximum precipitation is approximately two hours later, likely influenced by nocturnal MCSs.

Hayden and Liu (2021) reported that land and ocean areas between 20°N - 20°S had maximum precipitation at 1530 hours and 0430 hours for TRMM and GPM precipitation radar but at 1700 and 0600 hours for IMERG precipitation. One of the possible reasons for the delay is that the IMERG uses IR precipitation when PMW observations are absent. The IR cloud cover (and precipitation) has a delayed diurnal peak than PR surface precipitation (Liu and Zipser, 2008). Similarly, the thick stratiform cloud with cold PMW Tb might produce precipitation that may not reach the surface (Yuan and Houze, 2010; Tan et al., 2018). This will make spatially integrated rain amounts to be greater at a later time leading to the delayed diurnal maximum.

4.4.2 Regional: Coast to open ocean

Despite the lag in the diurnal cycle, the IMERG precipitation is useful for analyzing the transition of the diurnal cycle from coast to open ocean. We examine the regional transition of the diurnal cycle through different variables to understand the role of the MCS lifecycle and system sizes in the observed time of maximum precipitation.

4.4.2.1 Precipitation and TIMPS frequency

Fig. 4.4 shows the diurnal cycle of precipitation and TIMPS frequency for the onshore, offshore, transition, and open ocean areas in the three study regions. The diurnal cycle of the IMERG precipitation and TIMPS rain volume look similar though the

TIMPS represent MCSs. This is because the TIMPS rain volume includes sub-mesoscale precipitation when systems are in their initial and final stages.

The onshore and offshore areas of all three study regions have a strong diurnal cycle. The onshore of the Colombia coast has maximum precipitation near midnight, whereas the onshore of the West Africa coast and Sumatra coast have a maximum at 1900 hours. Though the offshore locations are part of the ocean, they have a stronger diurnal cycle than the open ocean. The transition areas (E. Pac1 and E. Atl) have a prominent peak in the early afternoon. This confirms the presence of maximum precipitation in the afternoon over the GATE domain on a much longer timescale. There is no afternoon maximum over the transition area (E. IO1) near the Sumatra coast, but a secondary mode is visible around noon. The open ocean areas in all three regions receive maximum precipitation in the early morning.

The TIMPS frequency has a strong diurnal cycle similar to the TIMPS rain volume for onshore and offshore areas. In these locations, the precipitation system frequency determines the time of maximum precipitation (fig. 4.4g, 4.4h, and 4.4i). However, the TIMPS frequency has a weaker diurnal cycle than precipitation over the open ocean areas and a lower frequency in the early morning than midnight. This indicates that other processes must enhance the existing convection to produce maximum precipitation in the early morning.

4.4.2.2 Initiation and Termination

The diurnal cycle of TIMPS initiation and termination present in fig. 4.5 will help understand the role of the MCSs lifecycle for the observed time of maximum

precipitation. The middle panels (fig. 4.5d, 4.5e, and 4.5f) show the TIMPS rain volume (same as in fig. 4.4d, 4.4e, and 4.4f) as a reference to compare the diurnal cycle of TIMPS initiation and termination.

Over onshore areas, the initiation occurs in the early afternoon (~1500 hours LST), likely from sea breeze circulation. Over the offshore areas, the initiation occurs near midnight (~ 2200 hours LST) at the same time when the onshore systems are dissipating at a higher frequency. Later, these offshore systems grow into mature MCSs and produce maximum precipitation in the early morning. The offshore systems dissipate slower than onshore systems, hence having a longer lifetime than onshore (Rajagopal et al., 2022).

In the open ocean areas (E. Pac2, C. Atl, and E. IO2), the TIMPS initiation peaks before noon and/or midnight, and the TIMPS termination peaks in the afternoon. The mechanism behind convection initiation close to noon and midnight needs further investigation. Over the transition areas (E. Pac1 and E. Atl), with the maximum precipitation in the afternoon, have TIMPS initiation peak at midnight and continues through noon with little variability. The resulting TIMPS frequency slightly increased after noon (figs. 4.5g and 4.5h). Therefore, the maximum precipitation in the afternoon must come from both the increased MCS frequency and the enhancement of existing convection.

In the open ocean and transition areas, the TIMPS termination peak from the afternoon through the early evening; during the same period, the precipitation reaches a minimum in the open ocean, but over E. Atl and E. Pac1, the precipitation reaches maximum.

4.4.2.3 Sub-mesoscale vs. mesoscale

The TIMPS initiation and termination help analyze the diurnal cycle. However, they represent only a subset of total IMERG precipitation. To better understand the IMERG precipitation diurnal cycle, we grouped the IMERG precipitation based on system sizes that include both TIMPS and non-TIMPS. The non-TIMPS are precipitation systems that did not satisfy our MCS criteria. The diurnal cycle of the IMERG precipitation by size (sub-mesoscale, small mesoscale, and large mesoscale) is presented in fig.4. 6. In general, the time of maximum precipitation occurs later with increasing system size. This is expected since the precipitation systems grow with time. The diurnal cycle of sub-mesoscale and small mesoscale precipitation has a single peak for onshore and offshore locations; however, they have a double peak near noon and midnight for transition and open ocean areas. This double peak is consistent with maximum TIMPS initiation just before noon and/or midnight for these locations.

The diurnal cycle of large mesoscale precipitation is similar to the diurnal cycle of total IMERG precipitation. Hence, they must be a significant contributor to total IMERG precipitation for these areas. The diurnal cycle of sub-mesoscale and small mesoscale precipitation has a large amplitude, although their contribution to total precipitation is small (fig. 4.6). This is because the hourly precipitation is expressed as a percentage of their daily contributions.

4.4.3 Spatial variability

The maximum precipitation in the afternoon is observed over the E. Pac1 and E. Atl but is absent over the E. IO1. This implies that the afternoon maximum is not present

in all transition areas. Hence, we examine the spatial variability of time of the maximum precipitation for four broad regions : i) Central America and Eastern Pacific, ii) West Africa and Atlantic, iii) South Asia and the Northern Indian Ocean, and iii) Maritime Continent and eastern Indian Ocean (fig. 4.7). The land typically has maximum precipitation in the late afternoon in these three regions. Some locations in West Africa and Laos have maximum precipitation occur during midnight or early morning.

While the spatial variability of the time of maximum precipitation over most open ocean locations has an early morning maximum, the E. Atl and E. Pac1 (transition areas) analyzed in previous sections have an early or late afternoon maximum. Near these places, the time of maximum precipitation progressively changes from early morning over offshore to an afternoon maximum over open ocean, ~1000 km from the coastline (fig. 4.7). Other areas with similar transition zones are southwest of the Mexican coast, central Bay of Bengal, and northeast of New Guinea. The afternoon maximum is not always present over transition areas (~1000 km from coastlines). However, the gradual change of time maximum in certain regions is intriguing.

4.4.4 Global: Coast to open ocean and inland

The maximum precipitation in the afternoon is present over many ocean areas ~1000 km from the coastlines. Here, we explore the impact of these areas on the global ocean's diurnal cycle and the variability of the diurnal cycle from coast to open ocean and inland. For this purpose, the IMERG grid cells are grouped into six areas based on their distance from the coastline. The onshore and offshore areas are land and ocean grid cells that are < 500 km from the coastline. The land and ocean transition areas are the grid

cells between 700 – 1200 km from the coastline. Finally, the inland and open ocean areas are the grid cells more than 1500 km from the coastline over land and ocean, respectively. Fig. 4.8 presents the diurnal precipitation cycle for these areas from coast to open ocean and inland.

The diurnal cycle for the global land has maximum precipitation around 1700 hours LST (fig. 4.3). The onshore and inland areas have maximum precipitation around the same time; however, the transition land areas have peak precipitation during the night and early morning (fig. 4.8), likely from the nocturnal MCSs. The inland areas have an evening maximum despite the nighttime MCSs observed over Africa and Amazon Basin (Zuluaga and Houze, 2015; Anselmo et al., 2021). When the precipitation is categorized by size, the inland areas have maximum precipitation from night to early morning (fig. 4.9) from large mesoscale precipitation. The evening maximum of total precipitation would imply that the sub-mesoscale and small mesoscale precipitation contribute significantly more than the large nocturnal systems. In contrast, over the open ocean, the diurnal cycle of the total precipitation looks similar to the diurnal cycle of large mesoscale precipitation (fig. 4.9), implying that large systems contribute significantly more than small systems.

Over the ocean, the double peak near noon and midnight for precipitation from sub-mesoscale and small mesoscale systems is interesting. The double peaks also coincide with maximum TIMPS initiation, implying that these systems grow into MCSs. Over the ocean, the double peaks (semi-diurnal cycles) in the afternoon and early morning have been reported in past studies (Chen & Houze, 1997b; Pereira & Rutledge, 2006; Watters and Battaglia, 2019). In this study, however, the peaks occur near noon

and midnight and need further research.

4.5 Discussion

Although there is a one to two hours delay in the time of maximum precipitation, IMERG is still helpful in examining the variability of precipitation diurnal cycle from coast to open ocean and inland. The convection over the land has been studied extensively and is closely tied to diurnally forced circulations with convergent boundaries such as sea breeze, lake breeze, and upslope flows. The nighttime precipitation over the land is often associated with MCSs aided by moist low-level jets (Zuluaga and Houze, 2015; Tan et al., 2019; Anselmo et al., 2021).

Over the ocean, many theories have been proposed to explain the early morning maximum. Some widely accepted theories are i) Direct Radiation-Convection interaction (DRC; Houze, 1982; Dudhia, 1989), ii) dynamical effects of the Day vs. Night Differential Tropospheric Radiational Cooling (DN-DTRC; Gray and Jacobson, 1977; McBride and Gray, 1980), iii) the MCS lifecycle and mesoscale processes (Chen and Houze, 1997), and iv) increased Available Precipitable Water from tropospheric cooling (APW; Sui et al., 1997). These mechanisms are briefly discussed in section 1. In our analysis, we find that over the ocean, the TIMPS initiation peak just before noon, midnight, or both. The resulting TIMPS frequency has a local minimum in the early morning. Therefore, the maximum precipitation in the early morning must be due to the enhancement of existing convection. The DRC, DN-DTRC, the increased APW, or a combination of these processes may be producing the observed early morning maximum (Ruppert and Hoggenegger, 2018).

The three mechanisms (DRC, DN-DTRC, and APW) explain the early morning maximum but not the afternoon maximum observed over the E. Atl and E. Pac1. For these areas, the diurnal cycle of the TIMPS frequency (fig. 4.4) shows slightly higher numbers around noon, but precipitation increased by a much larger percentage. Therefore the maximum precipitation in the afternoon must be a combined effect of increased MCSs frequency and enhanced precipitation. When we analyzed the diurnal cycle of TIMPS termination (fig. 4.5), MCSs terminate at a higher frequency in the afternoon. This could mean that some small systems merge to form a larger MCS, and the FiT tracking algorithm terminates all but one MCS. The merger of MCSs intensifies the existing convection and produces more precipitation due to reduced entrainment of dry ambient air (Feng et al., 2015; Glenn and Krueger, 2017).

The TIMPS lifecycle provided a context to understand the reasons for maximum precipitation in the early morning and afternoon over oceans. It is also fascinating that the time of maximum precipitation changes gradually from early morning over offshore Colombia to the afternoon ~1000 km from the coastline. Hence referred to as transition areas or zones. Fig 4.7. shows that similar transition areas are present southwest of Mexico, central Bay of Bengal, and northeast New Guinea. Since these transition areas are close to land, it must influence them. Land breeze circulation is weaker than sea breeze and is unlikely to travel such a long distance. The progressive change of maximum precipitation time would imply a propagating disturbance. Some possible mechanisms are gravity waves or propagating systems.

In a convection-permitting simulation over Colombia, Mapes et al. (2003) found diurnal and semi-diurnal gravity waves traveling at 15 ms^{-1} offshore and producing

convection. These gravity waves create a vertical motion above the boundary layer top, destabilizing the lower troposphere through increased lapse rate and moisture. Recent studies also found that gravity waves play a crucial role in offshore convection (Hassim et al., 2016; Coppin and Bellon, 2019b, 2019a). These theories explain the offshore convection through gravity waves, but they might also play a role in the convection observed ~1000 km from the coastline. Another possible mechanism for the progressive change of the diurnal phase is the MCSs propagating from offshore to the open ocean. However, the "time of maximum precipitation" changes more rapidly than the typical MCSs propagation speed of 5-8 ms⁻¹ in the tropics (Sakurai et al., 2009; Yanase et al., 2017; Rajagopal et al., 2022;). The gravity waves propagate at a much faster speed of 15 – 30 ms⁻¹ than the MCSs (Mapes et al., 2003b, Coppin and Bellon, 2019a,2019b). Hence, they must initiate convection far ahead of propagating MCSs and create the observed diurnal cycle.

The gravity waves might explain the gradual change in time of the maximum precipitation from offshore New Guinea to the open ocean areas to its northeast. However, similar transition areas are absent over the ocean west of the Sumatra coast. We think the ambient wind might also influence the propagation of gravity waves. During boreal winter, the winds are westerly over Maritime continent locations south of the equator. The transition areas are found downwind of New Guinea but absent on the upwind side of the Sumatra coast. The same is true over the central Bay of Bengal with westerly winds, southwest of Mexico with north easterly trades, east of Colombia with northeasterly and southwesterly wind convergence, and the eastern Atlantic with easterly winds. Therefore ambient wind and the gravity waves might play a combined role in

creating the gradually changing diurnal peak from offshore to the open ocean (Coppin and Bellon, 2019a, 2019b)

4.6 Summary

The diurnal cycle is one of the dominant modes of precipitation variability. The land and ocean have diurnal cycles that are out of phase, with maximum precipitation in the evening over land and early morning over the ocean. Though most locations over the ocean have an early morning maximum, an afternoon maximum was reported in the eastern Atlantic during the GATE field program. This afternoon maximum is likely influenced by nearby land. In this study, we analyzed the transition of the diurnal cycle from coast to open ocean and inland with intermediate locations similar to the GATE domain to understand possible reasons behind the afternoon maximum. First, we performed this analysis over three study regions (Colombia and eastern Pacific, west Africa and eastern Atlantic, and Sumatra and eastern Indian ocean) and then for the global tropics.

Our analysis shows that onshore and offshore locations have maximum precipitation in the evening, and early morning, respectively. The offshore diurnal cycle is much stronger than the typical ocean diurnal cycle. The diurnal cycle of TIMPS initiation shows that onshore convection terminates at a higher frequency when offshore convection initiates. Later, the offshore convection terminates at a slower rate while the convection shifts onshore. Over the open ocean (>1500 km from the coast), the maximum precipitation typically occurs early morning. The TIMPS frequency has small diurnal variability and a minimum in the early mornings. Therefore, maximum

precipitation must be from the enhancement of existing convection through a combination of mechanisms i) Direct Cloud-Radiation interaction, ii) dynamical effects of Day vs. Night Differential Tropospheric Radiative Cooling, and iii) increased Available Precipitable Water through radiative cooling.

Over the E. Atl and E. Pac1 (transition areas), the maximum precipitation occurs in the afternoon from both the increased MCS frequency and the precipitation enhancement. This enhancement is likely from the merger of some small systems to form a large MCS. The merging process intensifies existing convection and might create the observed afternoon maximum.

The spatial variability of diurnal maximum (fig. 4.7) shows that in the eastern pacific, the time of maximum precipitation changes gradually, with an early morning maximum over offshore to an afternoon maximum over the ocean areas ~1000 km from the coastline. Similar regions are found southwest of Mexico coast, central Bay of Bengal, eastern Atlantic, and northeast of New Guinea coast. The gradual change implies a propagating disturbance; possibly, the gravity waves propagate at a speed of 15 – 30 m s⁻¹. These gravity waves might initiate many convective systems that merge to produce maximum precipitation at the observed time.

The diurnal cycle of IMERG precipitation and the TIMPS dataset provided insights into the oceanic diurnal cycles with peaks in the early morning and afternoon. Though the diurnal cycle of the IMERG precipitation is delayed by 60-120 minutes compared to TRMM PR, it does not affect our conclusions. The MCSs lifecycle, used to interpret the results, is dependent on the tracking algorithm and subjective choices for algorithmic parameters that affect the merging and splitting of convective systems.

Hence, the results are interpreted based on the FiT algorithm used. The gravity wave has been hypothesized for this gradually changing diurnal cycle from coast to open ocean.

Further research is required to establish the proposed hypothesis.

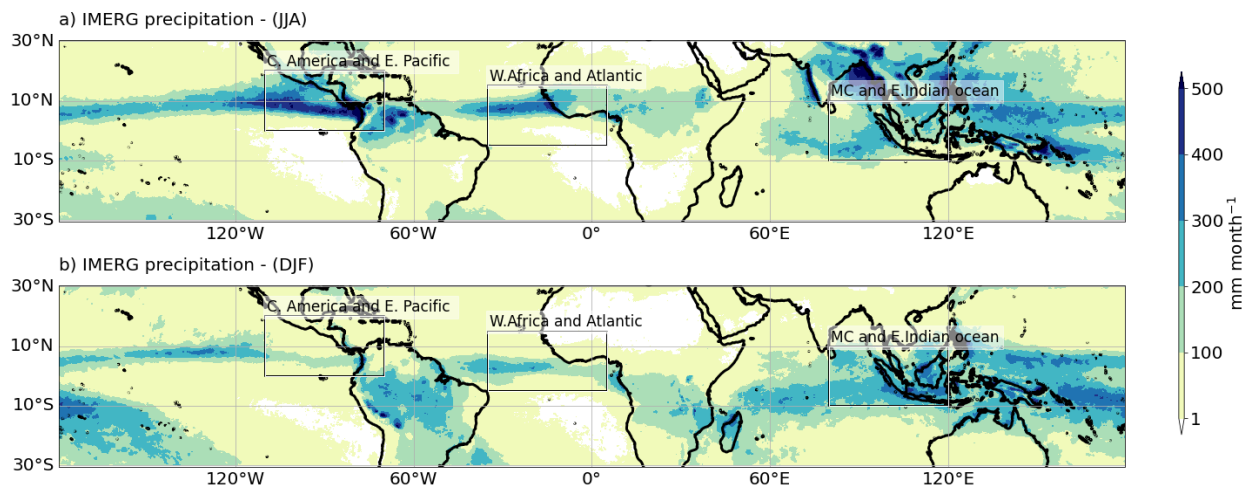


Fig. 4.1. The IMERG seasonal precipitation averaged over 2011 – 2020 for a) boreal summer and b) boreal winter. The boxes represent the three study regions (Central America and eastern Pacific, west Africa and Atlantic, and Maritime Continent and eastern Indian Ocean)

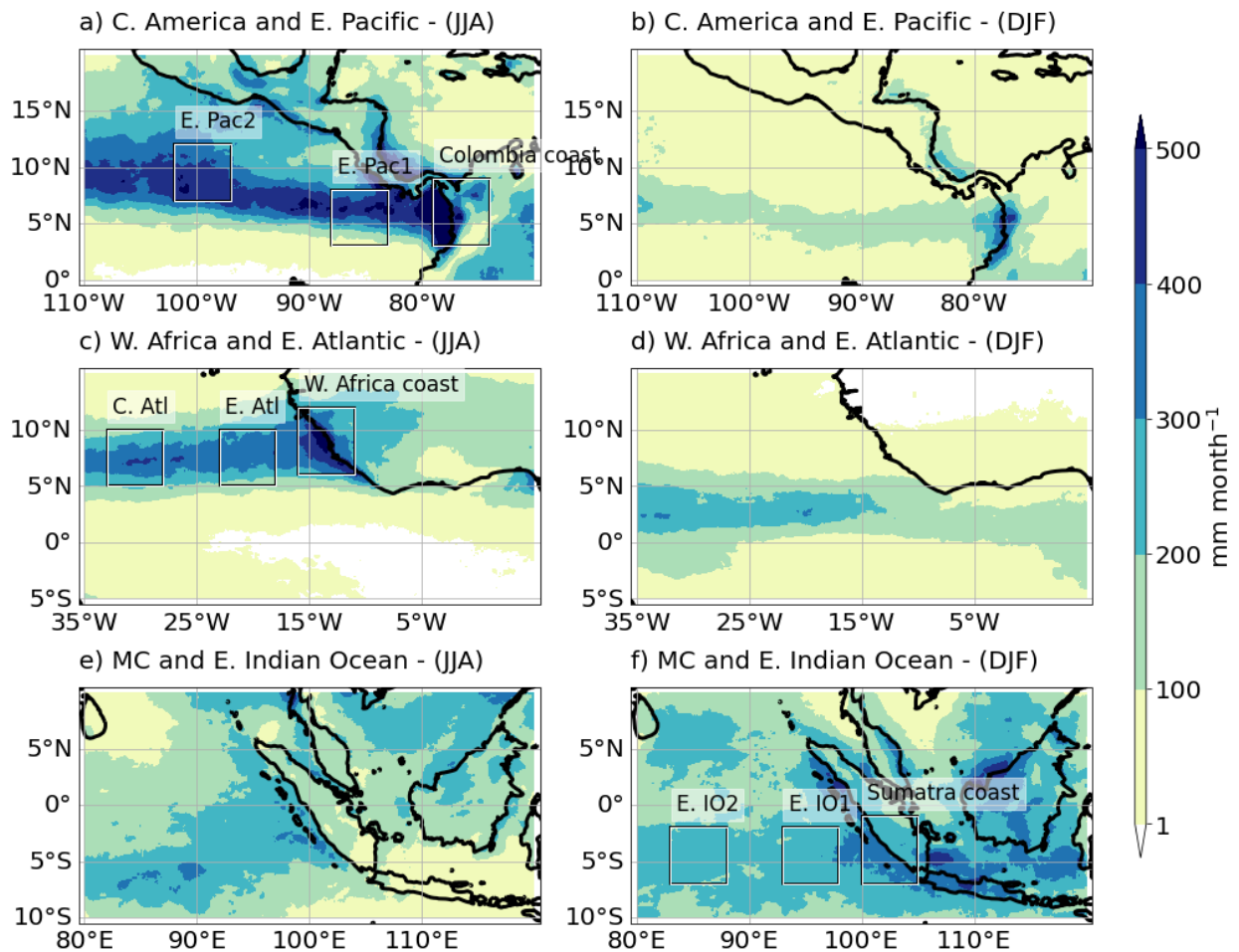


Fig. 4.2. The IMERG seasonal precipitation averaged over 2011 – 2020 for three study regions (Central America and eastern Pacific, west Africa and Atlantic, and Maritime Continent and eastern Indian Ocean) and two seasons (boreal summer and winter). The boxes represent coastal, transition, and open ocean areas from east to west.

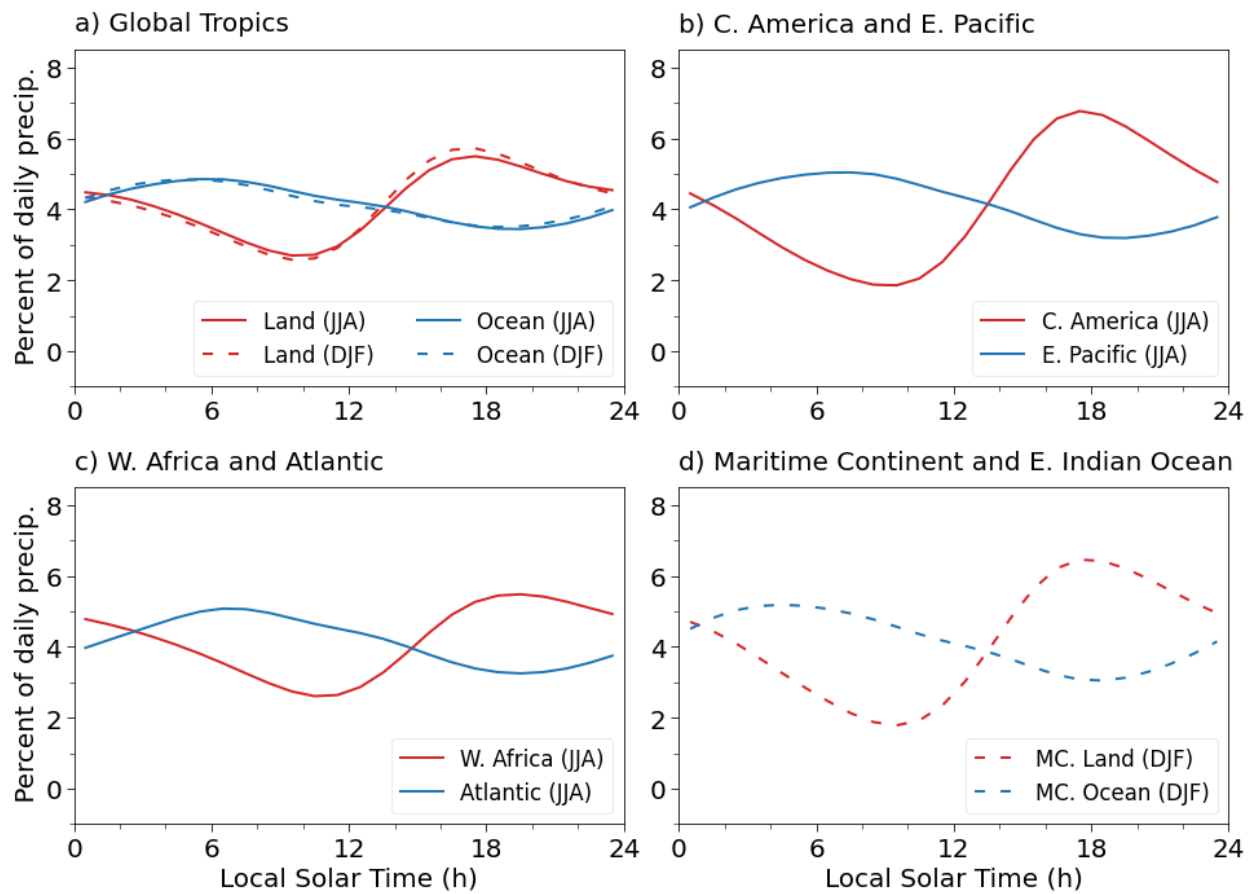


Fig. 4.3. The diurnal cycle of the IMERG precipitation averaged over 2011 - 2020 for a) global land and ocean, b) c) and d) land and ocean of three study regions.

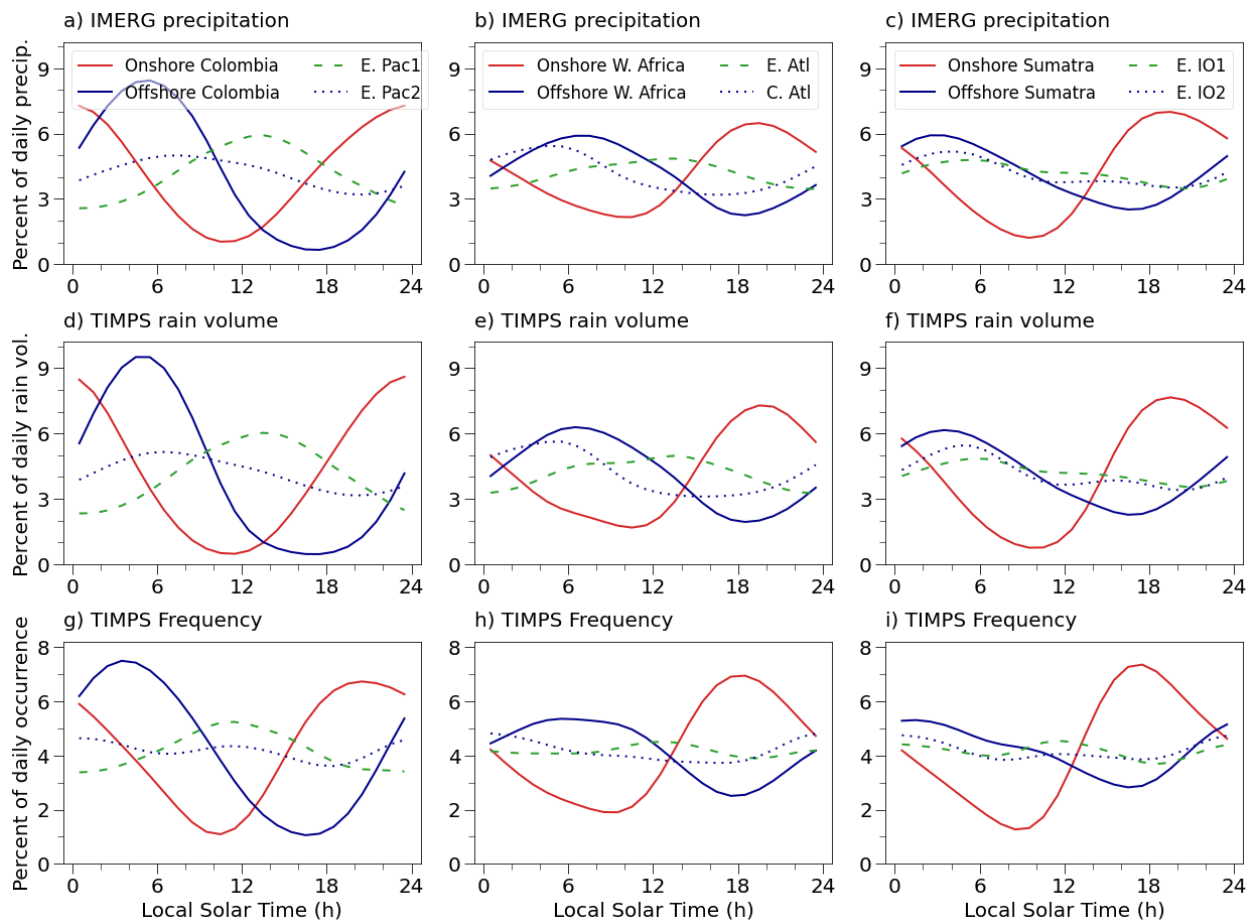


Fig. 4.4. The diurnal cycle of the IMERG precipitation, TIMPS rain volume, and TIMPS frequency for four areas (inside $5^\circ \times 5^\circ$ boxes) at various distances from the coastline in each of the three study regions.

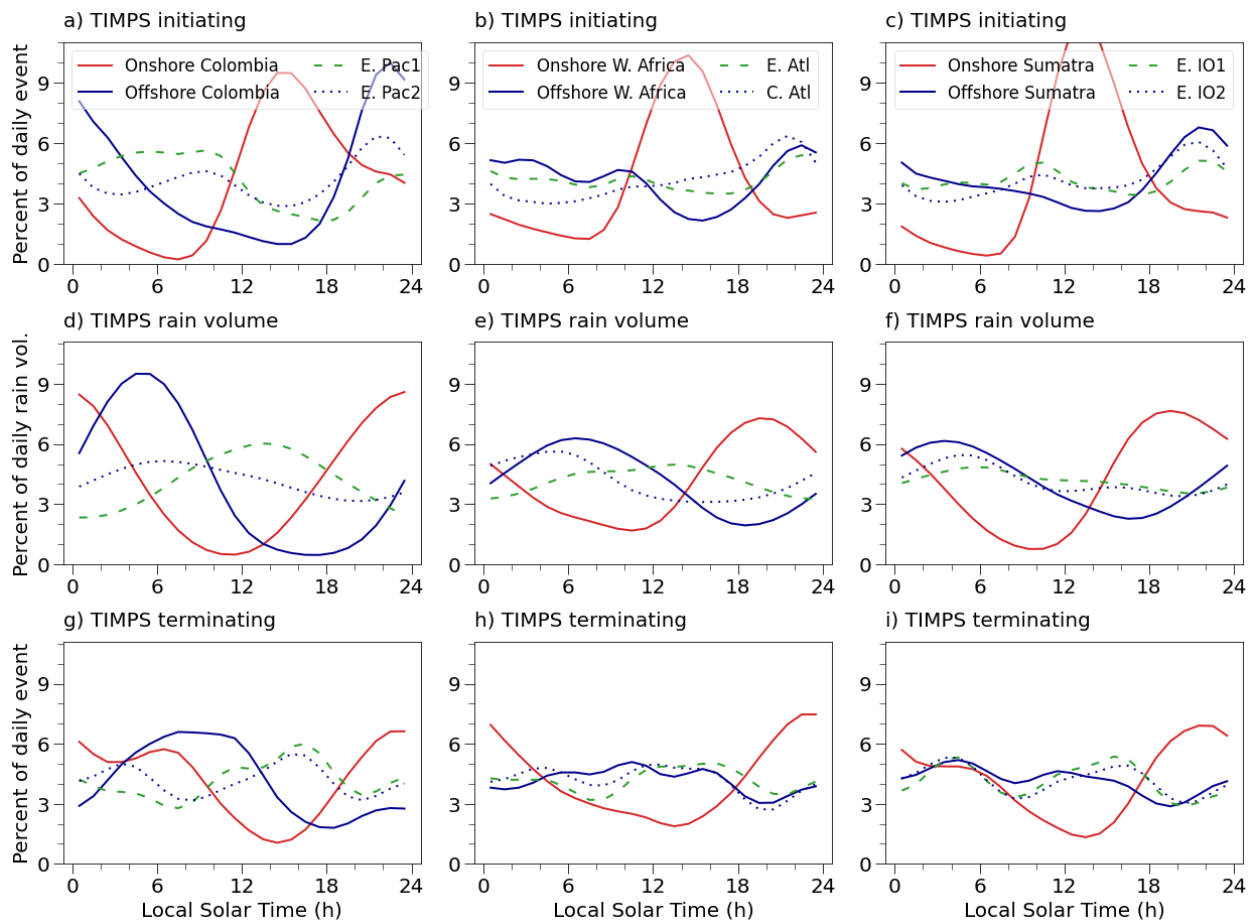


Fig. 4.5. The diurnal cycle of the TIMPS initiation, rain volume, and termination for four areas (inside $5^\circ \times 5^\circ$ boxes) at various distances from the coastline in each of the three study regions. The panels d) e) and f) are the same as fig 4d, 4e, and 4f, respectively. They are provided as a reference to compare the diurnal cycle of rain volume with initiation and termination.

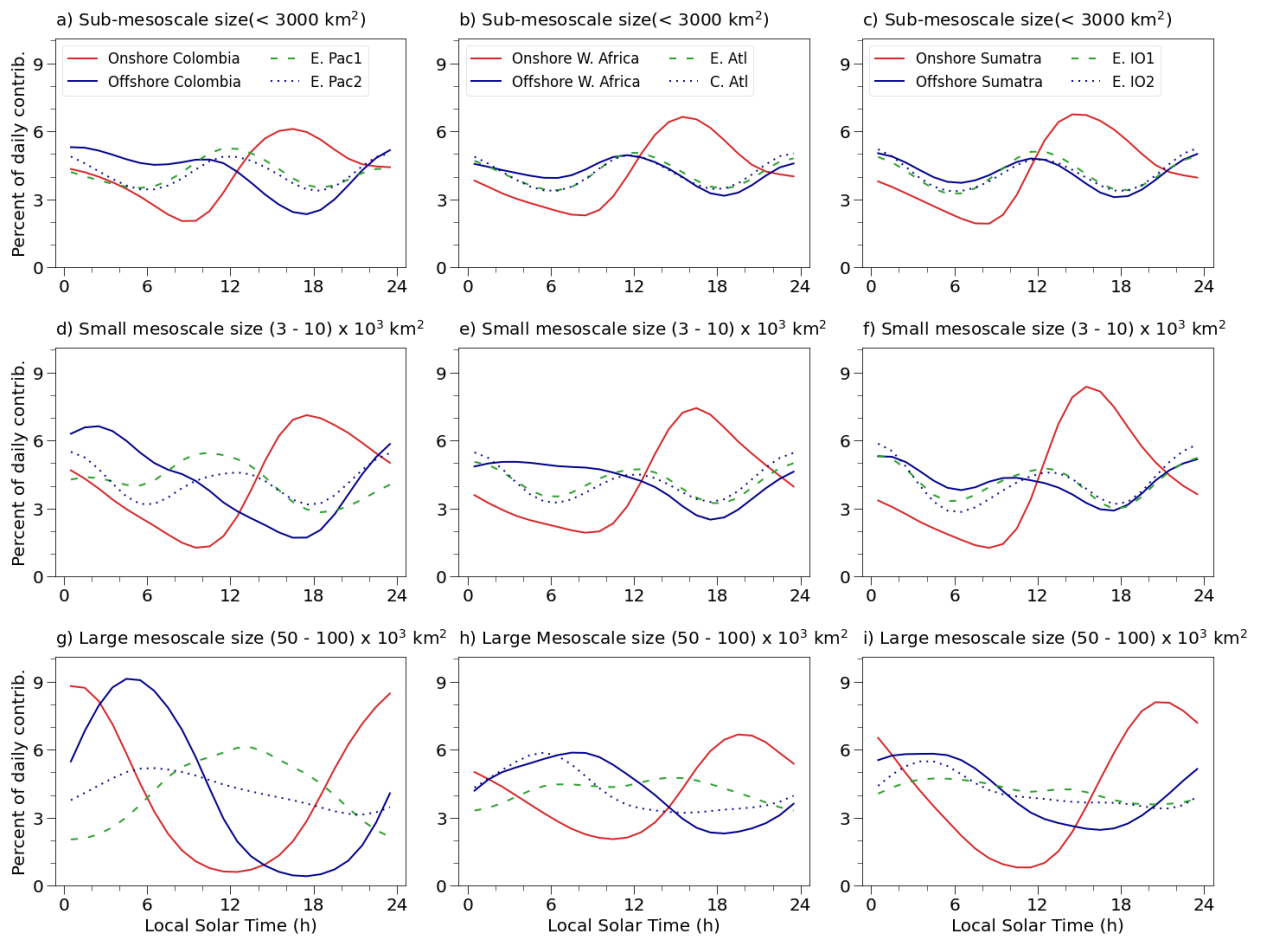


Fig. 4.6. The diurnal cycle of the precipitation contribution from different system sizes for four areas (inside $5^\circ \times 5^\circ$ boxes) at various distances from the coastline in each of the three study regions.

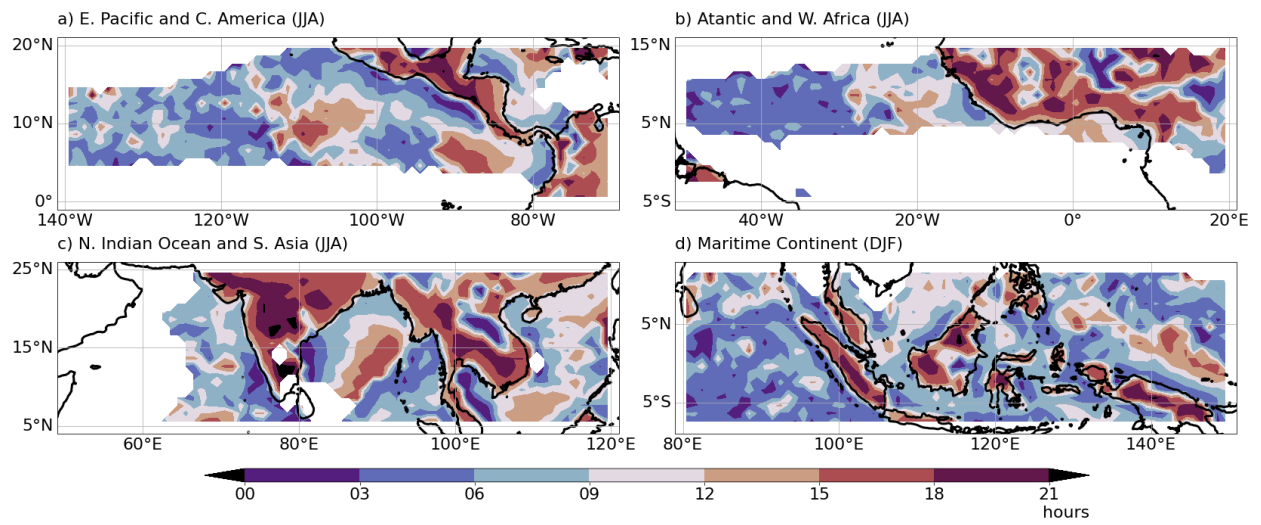


Fig. 4.7. Spatial variability of time of maximum IMERG precipitation. The data is smoothed by a running mean of 0.5° width to reduce the noise

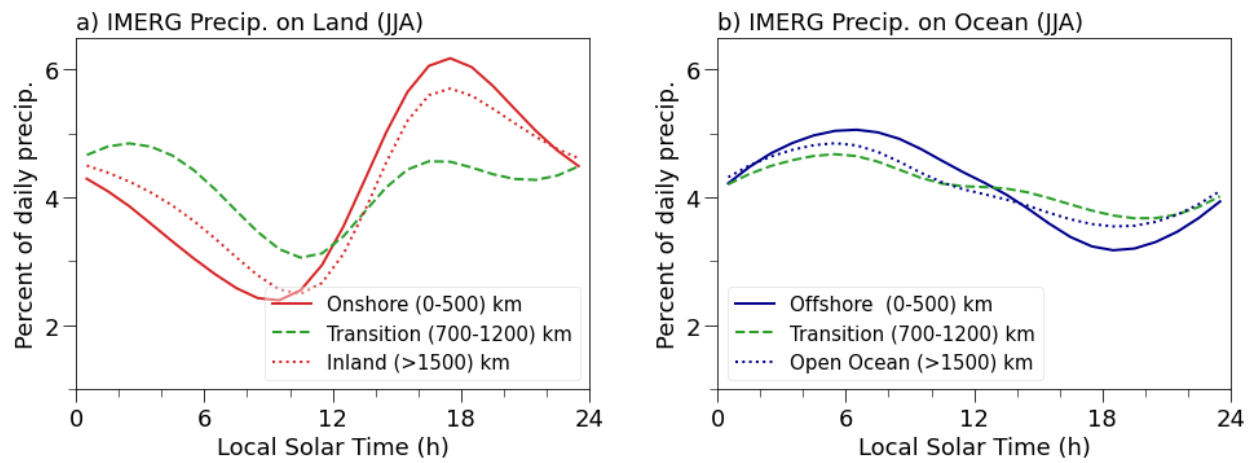


Fig. 4.8. The diurnal cycle of the IMERG precipitation for different areas at various distances from the coastline.

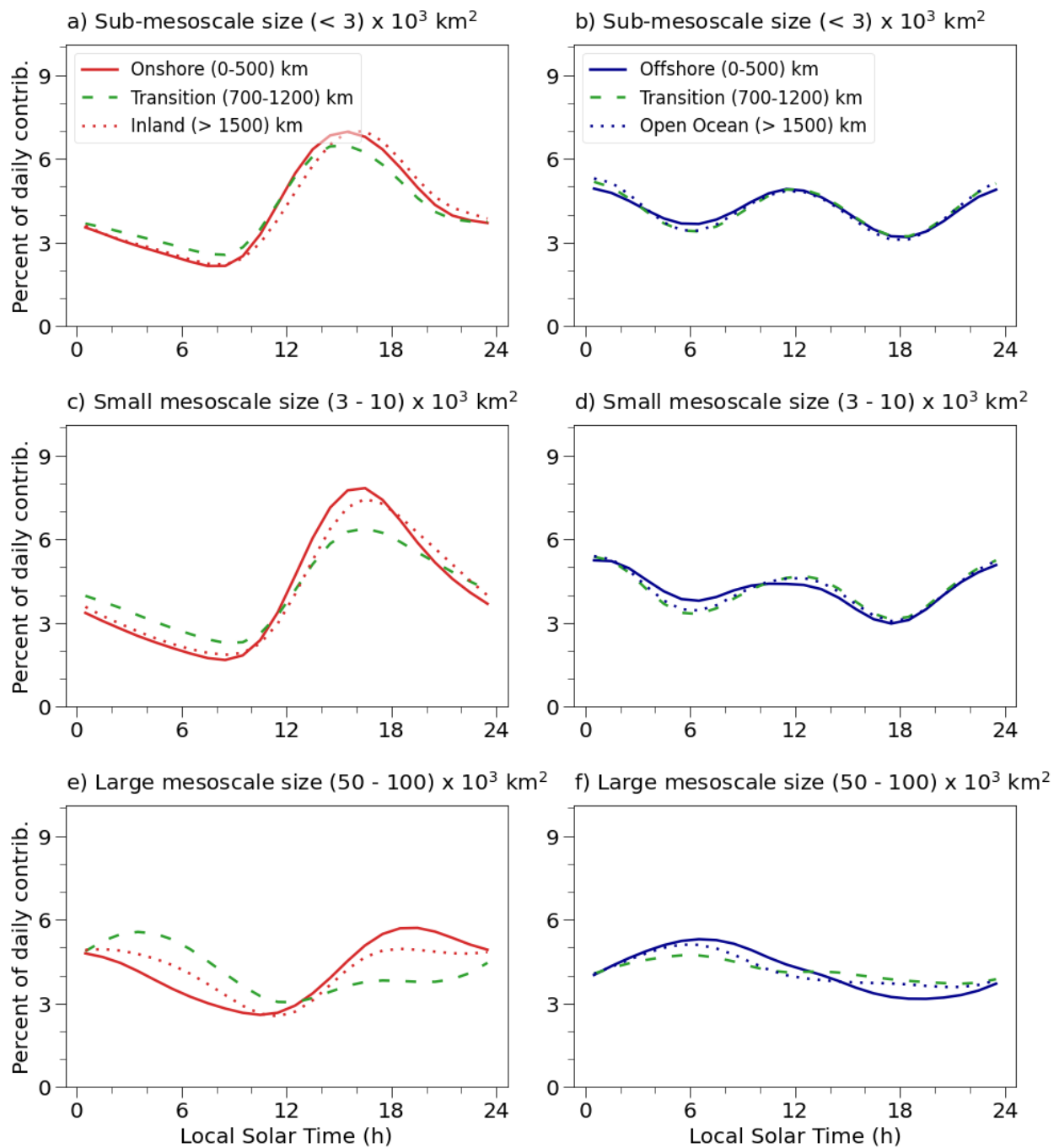


Fig. 4.9. The diurnal cycle of the IMERG precipitation by different system sizes for different global areas at various distances from the coastline.

4.7 References

- Albright, M. D., Recker, E. E., Reed, R. J., & Dang, R. (1985). The Diurnal Variation of Deep Convection and Inferred Precipitation in the Central Tropical Pacific During January–February 1979. *Monthly Weather Review*, *113*(10), 1663–1680. [https://doi.org/10.1175/1520-0493\(1985\)113<1663:TDVODC>2.0.CO;2](https://doi.org/10.1175/1520-0493(1985)113<1663:TDVODC>2.0.CO;2)
- Anselmo, E. M., Machado, L. A. T., Schumacher, C., & Kiladis, G. N. (2021). Amazonian mesoscale convective systems: Life cycle and propagation characteristics. *International Journal of Climatology*, *41*(7), 3968–3981. <https://doi.org/10.1002/joc.7053>
- Biasutti, M., Yuter, S. E., Burleyson, C. D., & Sobel, A. H. (2012). Very high resolution rainfall patterns measured by TRMM precipitation radar: Seasonal and diurnal cycles. *Climate Dynamics*, *39*(1–2), 239–258. <https://doi.org/10.1007/s00382-011-1146-6>
- Chen, S. S., & Houze, R. A. (1997). Diurnal variation and life-cycle of deep convective systems over the tropical Pacific warm pool. *Quarterly Journal of the Royal Meteorological Society*, *123*(538), 357–388. <https://doi.org/10.1256/smsqj.53805>
- CHEN, S. S., & HOUZE JR, R. A. (1997). Diurnal variation and life-cycle of deep convective systems over the tropical Pacific warm pool. *Quarterly Journal of the Royal Meteorological Society*, *123*(538), 357–388. <https://doi.org/10.1256/smsqj.53805>
- Coppin, D., & Bellon, G. (2019a). Physical Mechanisms Controlling the Offshore Propagation of Convection in the Tropics: 1. Flat Island. *Journal of Advances in Modeling Earth Systems*, *11*(9), 3042–3056. <https://doi.org/10.1029/2019MS001793>
- Coppin, D., & Bellon, G. (2019b). Physical Mechanisms Controlling the Offshore Propagation of Convection in the Tropics: 2. Influence of Topography. *Journal of Advances in Modeling Earth Systems*, *11*(10), 3251–3264. <https://doi.org/10.1029/2019MS001794>
- Cotton, W. R., Lin, M.-S., McAnelly, R. L., & Tremback, C. J. (1989). A Composite Model of Mesoscale Convective Complexes. *Monthly Weather Review*, *117*(4), 765–783. [https://doi.org/10.1175/1520-0493\(1989\)117<0765:ACMOMC>2.0.CO;2](https://doi.org/10.1175/1520-0493(1989)117<0765:ACMOMC>2.0.CO;2)
- Covey, C., Gleckler, P. J., Doutriaux, C., Williams, D. N., Dai, A., Fasullo, J., et al. (2016). Metrics for the Diurnal Cycle of Precipitation: Toward Routine Benchmarks for Climate Models. *Journal of Climate*, *29*(12), 4461–4471. <https://doi.org/10.1175/JCLI-D-15-0664.1>

- Dai, A. (2001). Global precipitation and thunderstorm frequencies. Part II: Diurnal variations. *Journal of Climate*, *14*(6), 1112–1128. [https://doi.org/10.1175/1520-0442\(2001\)014<1112:GPATFP>2.0.CO;2](https://doi.org/10.1175/1520-0442(2001)014<1112:GPATFP>2.0.CO;2)
- Dai, Aiguo, & Trenberth, K. E. (2004). The Diurnal Cycle and Its Depiction in the Community Climate System Model. *Journal of Climate*, *17*(5), 930–951. [https://doi.org/10.1175/1520-0442\(2004\)017<0930:TDCAID>2.0.CO;2](https://doi.org/10.1175/1520-0442(2004)017<0930:TDCAID>2.0.CO;2)
- Dudhia, J. (1989). Numerical Study of Convection Observed during the Winter Monsoon Experiment Using a Mesoscale Two-Dimensional Model. *Journal of the Atmospheric Sciences*, *46*(20), 3077–3107. [https://doi.org/10.1175/1520-0469\(1989\)046<3077:NSOCOD>2.0.CO;2](https://doi.org/10.1175/1520-0469(1989)046<3077:NSOCOD>2.0.CO;2)
- Feng, Z., Hagos, S., Rowe, A. K., Burleyson, C. D., Martini, M. N., & de Szoeki, S. P. (2015). Mechanisms of convective cloud organization by cold pools over tropical warm ocean during the AMIE/DYNAMO field campaign. *Journal of Advances in Modeling Earth Systems*, 357–381. <https://doi.org/10.1002/2014MS000384>
- Garstang, M., Massie, H. L., Halverson, J., Greco, S., & Scala, J. (1994). Amazon Coastal Squall Lines. Part I: Structure and Kinematics. *Monthly Weather Review*, *122*(4), 608–622. [https://doi.org/10.1175/1520-0493\(1994\)122<0608:ACSLPI>2.0.CO;2](https://doi.org/10.1175/1520-0493(1994)122<0608:ACSLPI>2.0.CO;2)
- Glenn, I. B., & Krueger, S. K. (2017). Connections matter: Updraft merging in organized tropical deep convection. *Geophysical Research Letters*, *44*(13), 7087–7094. <https://doi.org/10.1002/2017GL074162>
- Gray, W. M., & Jacobson, R. W. (1977). Diurnal Variation of Deep Cumulus Convection. *Monthly Weather Review*, *105*(9), 1171–1188. [https://doi.org/10.1175/1520-0493\(1977\)105<1171:DVODCC>2.0.CO;2](https://doi.org/10.1175/1520-0493(1977)105<1171:DVODCC>2.0.CO;2)
- Hassim, M. E. E., Lane, T. P., & Grabowski, W. W. (2016). The diurnal cycle of rainfall over New Guinea in convection-permitting WRF simulations. *Atmospheric Chemistry and Physics*, *16*(1), 161–175. <https://doi.org/10.5194/acp-16-161-2016>
- Hayden, L., & Liu, C. (2021). Differences in the Diurnal Variation of Precipitation Estimated by Spaceborne Radar, Passive Microwave Radiometer, and IMERG. *Journal of Geophysical Research: Atmospheres*, *126*(9), 1–24. <https://doi.org/10.1029/2020JD033020>
- Houze, Jr., R. A. (1982). Cloud Clusters and Large-Scale Vertical Motions in the Tropics. *Journal of the Meteorological Society of Japan. Ser. II*, *60*(1), 396–410. https://doi.org/10.2151/jmsj1965.60.1_396
- Houze Jr, R. a. (2004). Mesoscale Convective Systems-Review paper. *Reviews of Geophysics*, *42*, 1–43.

- <https://doi.org/10.1029/2004RG000150.1>.INTRODUCTION
- Houze, R. A., & Betts, A. K. (1981). Convection in GATE. *Reviews of Geophysics*, 19(4), 541. <https://doi.org/10.1029/RG019i004p00541>
- Huffman, G. J., and Coauthors, 2020a: NASA Global Precipitation Measurement (GPM) Integrated Multi-satellitE Retrievals for GPM (IMERG). Algorithm Theoretical Basis Doc., version 4.6, 28 pp., <https://gpm.nasa.gov/resources/documents/algorithm-information/IMERG-V06-ATBD>.
- Huffman, G. J., and Coauthors, 2020b: Integrated Multi-Satellite Retrievals for GPM (IMERG) technical documentation. NASA Tech. Doc., 77 pp., <https://gpm.nasa.gov/resources/documents/IMERG-V06-Technical-Documentation>
- Kraus, E. B. (1963). The Diurnal Precipitation Change over the Sea. *Journal of the Atmospheric Sciences*, 20(6), 551–556. [https://doi.org/10.1175/1520-0469\(1963\)020<0551:TDPCOT>2.0.CO;2](https://doi.org/10.1175/1520-0469(1963)020<0551:TDPCOT>2.0.CO;2)
- Liu, C., & Zipser, E. J. (2008). Diurnal cycles of precipitation, clouds, and lightning in the tropics from 9 years of TRMM observations. *Geophysical Research Letters*, 35(4), 1–6. <https://doi.org/10.1029/2007GL032437>
- Mapes, B. E., Warner, T. T., & Xu, M. (2003). Diurnal Patterns of Rainfall in Northwestern South America. Part III: Diurnal Gravity Waves and Nocturnal Convection Offshore. *Monthly Weather Review*, 131(5), 830–844. [https://doi.org/10.1175/1520-0493\(2003\)131<0830:DPORIN>2.0.CO;2](https://doi.org/10.1175/1520-0493(2003)131<0830:DPORIN>2.0.CO;2)
- McBride, J. L., & Gray, W. M. (1980). Mass divergence in tropical weather systems Paper I: Diurnal variation. *Quarterly Journal of the Royal Meteorological Society*, 106(449), 501–516. <https://doi.org/10.1002/qj.49710644908>
- McGarry, M. M., & Reed, R. J. (1978). Diurnal Variations in Convective Activity and Precipitation During Phases II and III of GATE. *Monthly Weather Review*, 106(1), 101–113. [https://doi.org/10.1175/1520-0493\(1978\)106<0101:DVICAA>2.0.CO;2](https://doi.org/10.1175/1520-0493(1978)106<0101:DVICAA>2.0.CO;2)
- Nesbitt, S. W., & Zipser, E. J. (2003). The diurnal cycle of rainfall and convective intensity according to three years of TRMM measurements. *Journal of Climate*, 16(10), 1456–1475. <https://doi.org/10.1175/1520-0442-16.10.1456>
- Peatman, S. C., Matthews, A. J., & Stevens, D. P. (2014). Propagation of the Madden-Julian Oscillation through the Maritime Continent and scale interaction with the diurnal cycle of precipitation. *Quarterly Journal of the Royal Meteorological Society*, 140(680), 814–825. <https://doi.org/10.1002/qj.2161>

- Pereira, L. G., & Rutledge, S. A. (2006). Diurnal cycle of shallow and deep convection for a tropical land and an ocean environment and its relationship to synoptic wind regimes. *Monthly Weather Review*, *134*(10), 2688–2701. <https://doi.org/10.1175/MWR3181.1>
- Rajagopal, M., Russell, J., Skok, G., & Zipser, E. (2022). Tracking Mesoscale Convective Systems and Spatial Variability of their Properties over the Global Tropics using IMERG. *Journal of Geophysical Research: Atmospheres*, 1–44 in preparation.
- Randall, D. A., Harshvardhan, & Dazlich, D. A. (1991). Diurnal Variability of the Hydrologic Cycle in a General Circulation Model. *Journal of the Atmospheric Sciences*, *48*(1), 40–62. [https://doi.org/10.1175/1520-0469\(1991\)048<0040:DVOTHC>2.0.CO;2](https://doi.org/10.1175/1520-0469(1991)048<0040:DVOTHC>2.0.CO;2)
- Reed, R. J., & Jaffe, K. D. (1981). Diurnal Variation of Summer Convection Over West Africa and the Tropical Eastern Atlantic During 1974 and 1978. *Monthly Weather Review*, *109*(12), 2527–2534. [https://doi.org/10.1175/1520-0493\(1981\)109<2527:DVOSCO>2.0.CO;2](https://doi.org/10.1175/1520-0493(1981)109<2527:DVOSCO>2.0.CO;2)
- Ruppert, J. H., & Hohenegger, C. (2018). Diurnal circulation adjustment and organized deep convection. *Journal of Climate*, *31*(12), 4899–4916. <https://doi.org/10.1175/JCLI-D-17-0693.1>
- Russell, J., Rajagopal, M., Veals, P., Skok, G., Zipser, E & Tinoco-Morales, M. (2022). A Dataset of Tracked Mesoscale Precipitation Systems in the Tropics. *Geoscience Data Journal*. in preparation
- Sakaeda, N., Powell, S. W., Dias, J., & Kiladis, G. N. (2018). The diurnal variability of precipitating cloud populations during DYNAMO. *Journal of the Atmospheric Sciences*, *75*(4), 1307–1326. <https://doi.org/10.1175/JAS-D-17-0312.1>
- Sakurai, N., Kawashima, M., Fujiyoshi, Y., Hashiguchi, H., Shimomai, T., Mori, S., et al. (2009). Internal structures of migratory cloud systems with diurnal cycle over Sumatera Island during CPEA-I campaign. *Journal of the Meteorological Society of Japan*, *87*(1), 157–170. <https://doi.org/10.2151/jmsj.87.157>
- Silva Dias, P. L., Bonatti, J. P., & Kousky, V. E. (1987). Diurnally Forced Tropical Tropospheric Circulation over South America. *Monthly Weather Review*, *115*(8), 1465–1478. [https://doi.org/10.1175/1520-0493\(1987\)115<1465:DFTTCO>2.0.CO;2](https://doi.org/10.1175/1520-0493(1987)115<1465:DFTTCO>2.0.CO;2)
- Skok, G., Tribbia, J., Rakovec, J., & Brown, B. (2009). Object-based analysis of satellite-derived precipitation systems over the low- and mid-latitude Pacific Ocean. *Monthly Weather Review*, *137*(10), 3196–3218. <https://doi.org/10.1175/2009MWR2900.1>

- Skok, G., Bacmeister, J., & Tribbia, J. (2013). Analysis of Tropical Cyclone Precipitation Using an Object-Based Algorithm. *Journal of Climate*, *26*(8), 2563–2579. <https://doi.org/10.1175/JCLI-D-12-00135.1>
- Sui, C.-H., Lau, K.-M., Takayabu, Y. N., & Short, D. A. (1997). Diurnal Variations in Tropical Oceanic Cumulus Convection during TOGA COARE. *Journal of the Atmospheric Sciences*, *54*(5), 639–655. [https://doi.org/10.1175/1520-0469\(1997\)054<0639:DVITOC>2.0.CO;2](https://doi.org/10.1175/1520-0469(1997)054<0639:DVITOC>2.0.CO;2)
- Tan, J., Petersen, W. A., Kirchengast, G., Goodrich, D. C., & Wolff, D. B. (2018). Evaluation of global precipitation measurement rainfall estimates against three dense gauge networks. *Journal of Hydrometeorology*, *19*(3), 517–532. <https://doi.org/10.1175/JHM-D-17-0174.1>
- Tan, J., Huffman, G. J., Bolvin, D. T., & Nelkin, E. J. (2019). Diurnal Cycle of IMERG V06 Precipitation. *Geophysical Research Letters*, *46*(22), 13584–13592. <https://doi.org/10.1029/2019GL085395>
- Wallace, J. M. (1975). Diurnal Variations in Precipitation and Thunderstorm Frequency over the Conterminous United States. *Monthly Weather Review*, *103*(5), 406–419. [https://doi.org/10.1175/1520-0493\(1975\)103<0406:DVIPAT>2.0.CO;2](https://doi.org/10.1175/1520-0493(1975)103<0406:DVIPAT>2.0.CO;2)
- Watters, D., & Battaglia, A. (2019). The summertime diurnal cycle of precipitation derived from IMERG. *Remote Sensing*, *11*(15), 1–17. <https://doi.org/10.3390/rs11151781>
- Yanase, A., Yasunaga, K., & Masunaga, H. (2017). Relationship between the direction of diurnal rainfall migration and the ambient wind over the Southern Sumatra Island. *Earth and Space Science*, *4*(3), 117–127. <https://doi.org/10.1002/2016EA000181>
- Yang, G. Y., & Slingo, J. (2001). The diurnal cycle in the tropics. *Monthly Weather Review*, *129*(4), 784–801. [https://doi.org/10.1175/1520-0493\(2001\)129<0784:TDCITT>2.0.CO;2](https://doi.org/10.1175/1520-0493(2001)129<0784:TDCITT>2.0.CO;2)
- Yang, S., & Smith, E. A. (2006). Mechanisms for diurnal variability of global tropical rainfall observed from TRMM. *Journal of Climate*, *19*(20), 5190–5226. <https://doi.org/10.1175/JCLI3883.1>
- Yuan, J., & Houze, R. A. (2010). Global variability of mesoscale convective system anvil structure from A-train satellite data. *Journal of Climate*, *23*(21), 5864–5888. <https://doi.org/10.1175/2010JCLI3671.1>
- Zuluaga, M. D., & Houze, R. A. (2015). Extreme Convection of the Near-Equatorial Americas, Africa, and Adjoining Oceans as seen by TRMM. *Monthly Weather Review*, *143*(1), 298–316. <https://doi.org/10.1175/MWR-D-14-00109.1>

CHAPTER 5

CONCLUSIONS.

5.1 Summary

The main objective of this work is to study the spatial and temporal variability of MCSs and their properties over the global tropics. IMERG is NASA's relatively recent precipitation product; therefore, we used the CPEX field program data to ascertain the IMERG's ability to represent MCSs and their lifecycle. Two case studies from CPEX showed that IMERG represented the observed MCSs reasonably well when there were PMW overpasses. However, in their absence, IMERG sometimes produced spurious precipitation, mostly $< 1 \text{ mm h}^{-1}$, and reduced precipitation intensities due to the time morphing algorithm (Rajagopal et al., 2021). We alleviate these issues by choosing the rain/no-rain threshold of 1 mm h^{-1} and using ten years of data to have enough PMW observations over any location. In addition, the biases are systematic and present in all regions. Therefore, any regional comparison and its qualitative conclusions are still valid and meaningful. Further, the collaboration with the IMERG team has led to the development of SHARPEN, a new algorithmic component of IMERG, that will mitigate the reported issues. This will be implemented in the upcoming IMERG Version 07 products (Tan et al., 2020).

The IMERG precipitation data, available every 30 minutes, makes tracking

precipitation systems more accurate and reliable because the precipitation systems propagate or evolve only slightly over this short time. We use the improved version of the FiT tracking algorithm to track MCSs in the IMERG precipitation. The FiT algorithm is a generic program that can track objects in any two or three-dimensional variable field. Therefore, we found the optimal value for FiT parameters that work for IMERG and tracked mesoscale precipitation systems reasonably well. Then, Dr. James Russell used these optimal parameters to track MCSs over the global tropics (30°N – 30°S) from 2011 to 2020. The MCS properties inferred from the IMERG precipitation at each time step of an MCS lifetime are stored in the TIMPS dataset (Russell et al., 2022). We use this TIMPS dataset to study the spatial and temporal variability of MCSs. TIMPS represent only a subset of tracked precipitation systems that satisfy our MCS criteria.

Our results, consistent with previous studies, show that MCSs contribute ~70% of annual precipitation over the tropics though they represent only ~7% of all tracked systems. MCSs occur more frequently over the Amazon basin and Maritime continent than in other land regions and oceans. The frequency of MCSs contrasts with a high frequency of intense convection over central Africa. This implies that the convective regime over the Amazon basin and Maritime Continent is different from central Africa.

A broader land and ocean comparison reveal that large, long-lived, and heavy rain-producing MCSs occur more often over the ocean than on land. A similar contrast exists between onshore and offshore locations along the west coasts of Colombia, Cameroon, Sumatra, and Borneo. Over these coastal locations, the offshore have a higher occurrence of MCSs with large areas and heavy rain rates than onshore. The MCSs with heavy rain rates occur more often over the offshore and open ocean than on land except

in the Amazon basin. The heavy rain rates have been observed over land from TRMM precipitation radar (Hamada et al., 2014), but IMERG has a low frequency of heavy rates on land. We hypothesize that the convection over land has heavy rain cores that are narrow, and they are spatially averaged by coarse PMW sensors, resulting in lower rain rates.

Past studies have shown that the convection over the Amazon basin has weaker updrafts and shallow cloud depths, similar to oceans; hence, called the “Green Ocean”. In addition, we find that these MCSs have a large area, longer lifetime, and heavy rain rates. The high occurrence of heavy rates similar to the ocean would imply wider heavy rain cores detectable by PMW sensors. Other regions that stand out are central America, Peru, the Arabian Sea, and the Bay of Bengal. Though they all have fewer MCSs, central America and Peru have MCSs that are mostly small, short-lived, and moderate rain producers. In contrast, the Bay of Bengal and Arabian sea have MCSs that are relatively large, long-lived, heavy rain producers.

Unlike other MCS properties, propagation velocity did not exhibit land and ocean contrast. West Africa and the Amazon basin have a high frequency of fast-moving ($10\text{-}15\text{ m s}^{-1}$) MCSs, which are likely squall lines. Though oceans typically have fewer squall lines, the western Pacific Ocean has a high frequency of fast-moving MCSs. The propagation direction of MCSs is mostly westward in the ITCZ of the Atlantic and the Pacific Ocean, but over the Indian ocean, the direction changes with monsoon circulation.

Another objective of this dissertation is to explore the temporal variability of precipitation and MCSs. The diurnal cycle of precipitation over land and ocean has been studied extensively. Though oceans typically have maximum precipitation in the early

morning, an afternoon maximum was observed over the eastern Atlantic during the GATE field program. This afternoon maximum is likely influenced by nearby land. Therefore we explored the transition of the diurnal cycle from coast to open ocean and the role of MCSs and their lifecycle in the observed diurnal cycle. We found that the afternoon peak is from both the increased MCS frequency and enhanced precipitation. The enhancement is possibly due to the merger of MCSs that intensifies the convection to produce afternoon maxima.

When the spatial variability of time of maximum precipitation is examined, we found that the time of peak precipitation changed gradually from early morning near the West African coast to the afternoon maximum over the eastern Atlantic. Other oceanic regions with similar transition zones are located southwest of Mexico, west of Colombia, central Bay of Bengal, and northeast of New Guinea. Since the time of maximum precipitation changes gradually, it must be a propagating disturbance and likely to be gravity waves. This disturbance likely initiated multiple MCSs, and some merged to produce maximum precipitation at the observed times, including the afternoon maximum.

5.2 Caveats

Though IMERG precipitation is more advantageous than IR precipitation, it has certain limitations. Our collaboration with the IMERG team and CPEX case studies helped us understand these limitations and choose the optimal parameters to track MCSs. Using different tracking algorithms or other choices for FiT tracking parameters would have produced different quantitative values. However, the qualitative conclusion presented here will remain the same.

The other issue with the IMERG precipitation is the delay in the time of maximum precipitation over land and ocean compared to the PR surface precipitation, which requires further investigation. Nevertheless, 60 – 120 minutes delay does not change our conclusions.

5.3 Future work

Our analysis produced exciting results and some open questions that will require further research. In IMERG, the heavy rain rates occur more often over the ocean than on land, despite previous studies that reported heavy rain rates over land. We hypothesized that the width of heavy rain cores is narrower over land than the ocean; hence the heavy rain rates are spatially averaged by the coarse PMW sensor resulting in lower rain estimates. Another potential research area is that the MCSs move faster (10 – 15 m s⁻¹) over the western Pacific ocean than in other ocean basins. Though fewer squall lines are observed over the ocean, the fast propagation speed is likely from the ambient winds. This question can be explored using the reanalysis data or sounding observations from nearby islands.

The TIMPS dataset combined with coincident GPM precipitation radar data provides a detailed MCS structure. The MCS structure at different lifecycle stages over different tropical regions is already being explored. Similarly, the TIMPS dataset combined with reanalysis data can be used to study the environmental factors that lead to upscale growth or dissipation.

5.4 References

- Hamada, A., Murayama, Y., & Takayabu, Y. N. (2014). Regional characteristics of extreme rainfall extracted from TRMM PR measurements. *Journal of Climate*, 27(21), 8151–8169. <https://doi.org/10.1175/JCLI-D-14-00107.1>
- Rajagopal, M., Zipser, E., Huffman, G., Russell, J., & Tan, J. (2021). Comparisons of IMERG Version 06 Precipitation At and Between Passive Microwave Overpasses in the Tropics. *Journal of Hydrometeorology*, 2117–2130. <https://doi.org/10.1175/jhm-d-20-0226.1>
- Russell, J., Rajagopal, M., Veals, P., Skok, G., Zipser, E. & Tinoco-Morales, M. (2022). A Dataset of Tracked Mesoscale Precipitation Systems in the Tropics. *Geoscience Data Journal*. in preparation
- Tan, J., Huffman, G. J., Bolvin, D. T., Nelkin, E. J., & Rajagopal, M. (2020). SHARPEN: A Scheme to Restore the Distribution of Averaged Precipitation Fields. *Journal of Hydrometeorology*, 2105–2117. <https://doi.org/10.1175/jhm-d-20-0225.1>